Western Graduate&PostdoctoralStudies

Western University
Scholarship@Western

Electronic Thesis and Dissertation Repository

12-12-2022 10:00 AM

Diffusion-Dependent Electrodes for All-Solid-State Lithium-Ion Batteries

Peiman Mardani, *The University of Western Ontario*

Supervisor: Sun, Xueliang (Andy), *The University of Western Ontario*

A thesis submitted in partial fulfillment of the requirements for the Master of Engineering Science degree in Mechanical and Materials Engineering

© Peiman Mardani 2022

Follow this and additional works at: https://ir.lib.uwo.ca/etd

 Part of the Energy Systems Commons

Recommended Citation

Mardani, Peiman, "Diffusion-Dependent Electrodes for All-Solid-State Lithium-Ion Batteries" (2022). *Electronic Thesis and Dissertation Repository*. 9032.
https://ir.lib.uwo.ca/etd/9032

This Dissertation/Thesis is brought to you for free and open access by Scholarship@Western. It has been accepted for inclusion in Electronic Thesis and Dissertation Repository by an authorized administrator of Scholarship@Western. For more information, please contact wlswadmin@uwo.ca.

Abstract

Electrode design, which is closely related to electronic and ionic transport, has a significant impact on all-solid-state batteries' performance. Typically, a combination of the active material and solid electrolyte serves as the electrode for all-solid-state batteries. An effective scaling technique to spatially organize the two components is essential for high-performance all-solid-state batteries. Here, an electrode design for all-solid-state batteries is given with a higher energy density than the typical composite-type electrode. The first section of the thesis presents a simple electrode design that primarily consists of blended active materials of graphite and phosphorus to meet the demands of all-solid-state batteries for high power and high energy density. The second section uses hard carbon electrodes to discover new anode materials for the diffusion-dependent electrode structure for all-solid-state batteries. It is demonstrated that by increasing the amount of active material in the electrode, this electrode configuration significantly increases the normalized energy density.

Keywords

All-solid-state battery, Electrode design, Composite electrode, Diffusion-dependent electrode, High energy density

Summary for Lay Audience

A successful design for all-solid-state electrodes is essential to achieve high-performance all-solid-state batteries. A typical structure to create well-percolated ionic channels within the electrode is a composite electrode, which is made up of well-mixed active material and solid electrolyte. Therefore, for high-performance all-solid-state batteries, an effective procedure to spatially organize the two components in a scalable manner is essential. In contrast, a newly developed method using interparticle diffusion between active material particles is called a diffusion-dependent electrode, primarily made of active material. Maximizing energy density and simplifying the manufacturing process are both made possible by this design. Herein, diffusion-dependent electrode design for all-solid-state batteries provides a higher energy density than the common composite-type electrode. The suggested electrode provides a seamless interface between the active materials, enabling interparticle lithium-ion diffusion. As a result, the solid electrolyte can be disregarded entirely during the electrode manufacturing process, allowing for greater procedure flexibility, and eliminating concerns regarding the incompatibility between solid electrolytes and active electrode materials. The first section of the thesis presents a straightforward electrode design that primarily consists of blended graphite and phosphorus active materials to satisfy the high power and high energy density requirements of all-solid-state batteries. The second section employs hard carbon electrode to show the capabilities of the diffusion-dependent electrode structure for all-solid-state batteries. It is demonstrated that increasing the amount of active material in the electrode can increase the normalized energy density. Thus, this electrode idea is a significant step forward for high-performance all-solid-state batteries.

Acknowledgments

This research was conducted in the Advanced Materials for Clean Energy Group under the supervision of Dr. Xueliang (Andy) Sun at the University of Western Ontario (UWO). It is my pleasure to acknowledge Dr. Sun and all those who contributed to my work over the past two years in this document.

First and foremost, I would like to express my sincere gratitude to my supervisor, Dr. Xueliang (Andy) Sun, a professor in the Department of Mechanical and Materials Engineering at UWO, a Canada Research Chair, a Fellow of the Canadian Academy of Engineering, and a Fellow of the Royal Society of Canada. Dr. Sun gave me this study opportunity and tremendous support over the course of the last two years as I completed my master's degree, and I really appreciate it. I am particularly grateful to Dr. Yang Zhao, an assistant professor in the Department of Mechanical and Materials Engineering at UWO, for his constructive feedback and suggestions regarding my study.

I would like to thank the lab manager, Ruying (Kathy) Li, and all the other researchers in our group for keeping a welcome and encouraging environment and for supporting me whenever I needed assistance with my laboratory work. Also, I want to express my gratitude to my sub-group colleagues for their support and direction during our meetings and discussions: Dr. Changhong Wang, Matthew Zheng, Kieran Doyle Davis, Justin J.T. Kim, and Dr. Adam Fraser. Particularly, I want to express my gratitude to Dr. Changhong Wang for his mentorship, extensive knowledge, assistance with the planning of my research project, and valuable advice and direction throughout the study process.

I also want to thank Dr. Hui Duan for her assistance with the X-ray diffraction (XRD) procedure and Dr. Weihan Li for his helpful assistance in the laboratories. I would like to express my gratitude to the personnel and postdoctoral fellows at the NanoSi Energy Company and GLABAT Solid-State Battery Inc., notably Dr. Huang, Dr. Qingwen Lu, and Dr. Shiting (Erica) Huang for their assistance with my research and the use of their facilities. I want to express my gratitude to the staff in the Mechanical and Materials Engineering

Department at UWO for making my journey as smooth as they possibly could, especially during a pandemic.

Finally, I would like to thank my family from the bottom of my heart. Without their support, financially and emotionally, I could not complete my master's thesis. Over the past two years, they have given me tremendous levels of unwavering love, inspiration, motivation, and support.

Table of Contents

List of Tables

List of Figures

Glossary

ASSB – all-solid-state battery

ASSLIB – all-solid-state lithium-ion battery

CC – constant current

CE – coulombic efficiency

DMC – dimethyl carbonate

EC – ethylene carbonate

EDX – energy dispersive X-ray spectroscopy

EIS - electrochemical impedance spectroscopy

EMC – ethyl methyl carbonate

ESS – energy storage system

EV – electric vehicle

GCD – galvanostatic charge-discharge

GITT – galvanostatic intermittent titration technique

Gr/P – graphite-phosphorus

HC – hard carbon

HEV – hybrid electric vehicle

HP – high pressure

HT - high temperature

ICE – internal combustion engine

LATP - $Li_{1+x}Al_xTi_{2-x}(PO_4)_3$

LGPS - $Li_{10}GeP_2S_{12}$

LIB – lithium-ion battery

LLZO - $Li_7La_3Zr_2O_{12}$

LPSCl - Li_6PS_5Cl

NMP – N-methyl-2-pyrrolidone

PVDF - polyvinylidene fluoride

RT – room temperature

SEI – solid-electrolyte interphase

SEM – scanning electron microscopy

SSE – solid-state electrolyte

XRD – X-ray diffraction

1 Chapter 1: Introduction to the Thesis

1.1 Background and Objectives

Lithium-ion batteries (LIBs) have been successfully used in consumer electronics and electric vehicles (EVs) since their commercialization in 1991 due to their high volumetric and gravimetric energy density, high power density, long lifespan, and lack of memory effect [1]. Because of the widespread use of LIBs, the Nobel Prize in chemistry for 2019 was given to Stanley Whittingham, John Goodenough, and Akira Yoshino for their significant contributions to the invention of LIBs. The world has become concerned about the safety of LIBs in recent years owing to several fire/explosion accidents involving EVs and mobile phones. In addition, high-energy-density LIBs are in high demand due to the expensive cost and limited driving range of EVs [2], [3]. As a result, individuals are motivated to design LIBs with high energy density and high safety.

All-solid-state lithium-ion batteries (ASSLIBs) have been attracting interest from all around the world because of their excellent energy density and increased safety [4]–[8]. An essential element for achieving ASSLIBs is a solid-state electrolyte (SSE). The development of highly Li^+-conductive SSEs has received much attention over the past few decades, with oxide electrolytes, sulfide electrolytes, and polymer electrolytes among the examples [8], [9]. Sulfide electrolytes typically have the best mechanical properties and the highest ionic conductivity (10^{-3} ~ 10^{-2} $S.cm^{-1}$) among these SSEs. However, developing ASSLIBs based on sulfide electrolytes is seriously hindered by high interfacial resistance, poor air stability, and a narrow electrochemical stability window. Sulfide electrolytes and sulfide-based ASSLIBs have been the subject of many notable results and benchmark performances in recent years.

The electrochemical properties of the all-solid-state batteries (ASSBs) can be significantly influenced by the electrode design and the development of new solid electrolyte materials. As a result, the fabrication of ASSBs with high energy densities depends on developing innovative and efficient electrode materials. Therefore, the main objectives of this thesis are to develop effective fabrication techniques and suitable anode

materials to produce high-performance ASSBs. These objectives are as follows in further detail:

The first objective is investigating the impact of the diffusion-dependent electrode structure on the performance of ASSBs as well as achieving high and stable performance of diffusion-dependent electrode at room or low temperatures. The electrode for ASSBs is typically made from a composite of active material and solid electrolytes to mimic the electrode of LIBs using liquid electrolytes. However, a design for an all-solid-state electrode is described here for ASSBs to attain a higher energy density than the common composite-type electrode. The proposed electrode is mainly made of active materials and provides a seamless interface between the active materials, which enables interparticle lithium-ion diffusion. As a result, the solid electrolyte can be entirely omitted during the electrode manufacturing process, resulting in greater fabrication procedure flexibility by allaying issues about the (electro)chemistry of solid electrolytes. Currently, many studies report the electrochemical performance of diffusion-dependent electrodes at elevated temperatures (60 °C~100 °C) due to the limited ion transport kinetics.

The second objective of this research is to develop high-performance anode materials for ASSLIBs that are consistent with the diffusion-dependent structure. A composite of graphite-phosphorus (Gr/P) and hard carbon (HC) are the two anode materials used in this work. The selected materials should be able to deform mechanically in response to an applied force. As a result, when the active material particles are compressed, they can come into close contact with one another, which makes it easier for lithium ions to diffuse. This study aims to reveal the electrochemical mechanisms for lithium storage based on these materials and electrode structure, as well as the relationship between these materials and the associated electrochemical performance.

1.2 Thesis Outline

This thesis contains six chapters organized in an integrated article format: an introduction, a literature review, a summary of the experimental procedures, two articles, and a conclusion. It is structured in compliance with the Thesis Regulation Guide from

the School of Graduate and Postdoctoral Studies at the University of Western Ontario. Each chapter is separated into the following outline.

Chapter 1 covers the background, objectives, and structure of the thesis.

Chapter 2 introduces the fundamentals and challenges of traditional LIBs. The ASSLIBs and their operating principles are also briefly discussed. State-of-the-art SSEs and electrodes are addressed in detail.

Chapter 3 describes detailed descriptions of the experimental procedures employed in the thesis, such as cell assembly, electrode preparation, and all the characterization techniques used.

Chapter 4 presents the performance of the Gr/P diffusion-dependent electrode in ASSLIBs. First, different active materials ratios (graphite: phosphorus) are investigated to find the optimal ratio that performs the best in capacity and stability. Although increasing the phosphorus content of a Gr/P composite electrode typically results in greater capacity values, there is a trade-off between stability and capacity. The performance of the selected electrode is then compared with that of the graphite diffusion-dependent electrode to demonstrate the superiority of the proposed electrode.

Chapter 5 examines the performance of the HC diffusion-dependent electrode in ASSLIBs based on sulfide electrolyte. The electrochemical performance of the diffusion-dependent electrode in ASSB is supplied and compared at various testing parameters. Since, HC has never been investigated in the diffusion-dependent electrode for ASSBs, the presented results are compared with the information on liquid LIBs to determine the validity of the technique and material.

Chapter 6 examines the thesis' goals and summarize the results from chapters 4 and 5. Future research based on this thesis is suggested after discussing the possibilities of diffusion-dependent electrodes and associated anode materials.

1.3 References

[1] M. Armand and J. M. Tarascon, “Issues and challenges facing rechargeable lithium batteries,” *Nature*, vol. 414, no. 6861, pp. 359–367, 2001.

[2] T. Yim, C. Y. Choi, J. Mun, S. M. Oh, and Y. G. Kim, “Synthesis and properties of acyclic ammonium-based ionic liquids with allyl substituents as electrolytes,” *Molecules*, vol. 14, no. 5, pp. 1840–1851, 2009.

[3] K. Xu, “Nonaqueous liquid electrolytes for lithium-based rechargeable batteries,” *Chem. Rev.*, vol. 104, no. 10, pp. 4303–4418, 2004.

[4] J. W. Choi and D. Aurbach, “Promise and reality of post-lithium-ion batteries with high energy densities,” *Nat. Rev. Mater.*, vol. 1, no. 4, p. 16013, 2016, doi: 10.1038/natrevmats.2016.13.

[5] Y. Zhao, K. Zheng, and X. Sun, “Addressing interfacial issues in liquid-based and solid-state batteries by atomic and molecular layer deposition,” *Joule*, vol. 2, no. 12, pp. 2583–2604, 2018.

[6] A. Manthiram, X. Yu, and S. Wang, “Lithium battery chemistries enabled by solid-state electrolytes,” *Nat. Rev. Mater.*, vol. 2, no. 4, p. 16103, 2017, doi: 10.1038/natrevmats.2016.103.

[7] K. H. Park *et al.*, “Design Strategies, Practical Considerations, and New Solution Processes of Sulfide Solid Electrolytes for All-Solid-State Batteries,” *Adv. Energy Mater.*, vol. 8, no. 18, 2018, doi: 10.1002/aenm.201800035.

[8] Y. Kato *et al.*, “High-power all-solid-state batteries using sulfide superionic conductors,” *Nat. Energy*, vol. 1, no. 4, p. 16030, 2016, doi: 10.1038/nenergy.2016.30.

[9] N. Kamaya *et al.*, “A lithium superionic conductor,” *Nat. Mater.*, vol. 10, no. 9, pp. 682–686, 2011, doi: 10.1038/nmat3066.

2 Chapter 2: Literature Review

2.1 Introduction to Lithium-ion Batteries

Lithium-ion batteries (LIBs) have been on the market for almost three decades. They have quickly evolved from being the power source of choice for small-scale applications like portable electronics to large-scale applications like (hybrid) electric vehicles ((H)EVs) and even stationary energy storage systems (ESSs) since they present an unrivaled combination of high energy and power densities, long cycle life, and low prices. Compared to primary lithium batteries of the first generation, which use lithium metal as an anode material and are non-rechargeable, lithium-ion batteries are classified as secondary rechargeable batteries [1]–[3]. Due to their high gravimetric and volumetric energy densities and flexible design, Li-based batteries now perform better than other kinds of secondary batteries among the existing technologies (**Figure 2.1**) [4]. They can be lighter and take up less space because of this. Additionally, they can recharge faster than other types of batteries due to their better power densities. These benefits come from lightweight lithium-containing compounds and a non-aqueous electrolyte, enabling a broader voltage range between the two electrodes. Due to the relationship between the energy density and this voltage range, a greater voltage will result in a higher energy density. They represent 63% of the global sales values for portable batteries [5]. This explains why they are given the greatest amount of attention at both the basic and applied levels.

The technology upgrading of LIBs is in high demand due to the rapid development of EVs and ESSs. As projected, it necessitates LIBs with higher power and energy densities [1]. Due to increased demand for more environmentally friendly transportation options as well as increased support from the public and private sectors, the number of existing EVs has grown exponentially over the last few years, from fewer than 1 million EVs in 2014 to over 10 million EVs globally in 2020 [6]. However, several issues still need to be resolved for LIBs used in EVs to match or outperform the performance of the internal combustion engine (ICE) used in conventional vehicles. These issues include higher

energy and power densities, faster-charging speeds, longer lifetimes, better safety, and lower costs [7], [8].

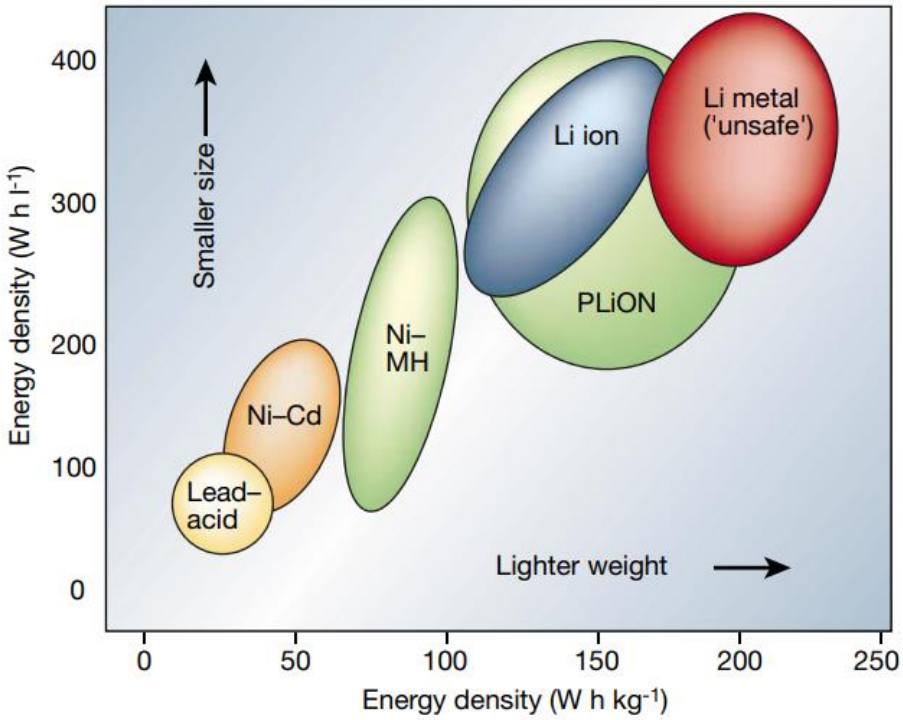

Figure 2.1: Comparison of the volumetric and gravimetric energy densities of the various battery technologies. Reproduced with permission from Springer Nature [4].

2.1.1 Fundamentals of Lithium-ion Batteries

A carbonate-based organic electrolyte with a dissolved lithium salt, a separator, a lithium metal oxide cathode (positive electrode), a carbonaceous anode (negative electrode), and current collectors comprise the electrochemical cells that make up LIBs. The great cyclability of intercalation materials makes them a common choice for both electrodes. Without causing a significant structural change, lithium ions (guests) are reversibly inserted or ejected into the host material during the intercalation process [9]. In LIBs, as the electrodes are charged or discharged, the electrolyte serves as an ion conductor. Also, separators prevent physical contact between the cathode and anode from short circuits while allowing lithium ions to flow freely through their design. Electrons are gathered

from the electrodes by current collectors and then sent through the external circuit. As shown in **Figure 2.2**, these elements can be coupled to create various LIB configurations.

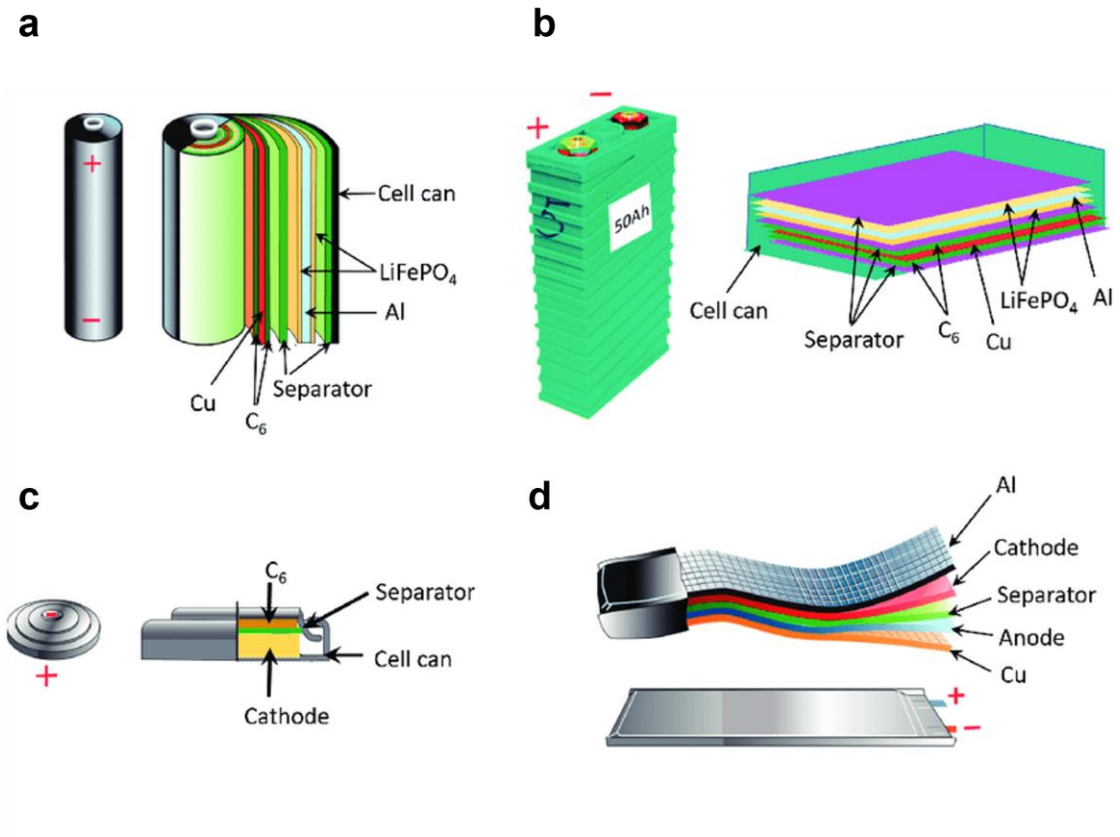

Figure 2.2: Representation of the shape and components of various LIB configurations: cylindrical (a), prismatic (b), coin (c), and pouch cell (d). Reproduced with permission from Springer Nature [10].

A lithium cobalt oxide ($LiCoO_2$) cathode and a graphite (C) anode are the traditional components of a high-capacity LIB [11]. Both electrodes are made from active (Li-ion storing) powders mixed with a small amount (1–5 wt%) of conductive carbon additives (mostly carbon black) and a small amount (3-5 wt%) of a polymer binder (mostly polyvinylidene fluoride, PVDF). They are then cast on both sides of metal current collector foils (Al foil for the cathode and Cu foil for the anode). The completed electrode layer typically has a thickness of between 60 and 100 micrometers on each side of the foil. A porous electrically insulated membrane separates the electrodes of a battery with a

typical thickness of 15 to 25 micrometers. Lithium ions are transported between electrodes using organic carbonate liquids as a polar aprotic conductive route. Because it provides the optimal blend of high ionic conductivity and low viscosity for the transport of lithium salt ions ($LiPF_6$ or $LiClO_4$), a combination of linear and cyclic carbonates in the form of 1:1 ethylene carbonate (EC) to dimethyl carbonate (DMC) is generally utilized. The processes of deintercalation at the anode and intercalation at the cathode are represented in **Figure 2.3**, a schematic representation of a commercial LIB with a carbon anode and a transition metal oxide cathode [12].

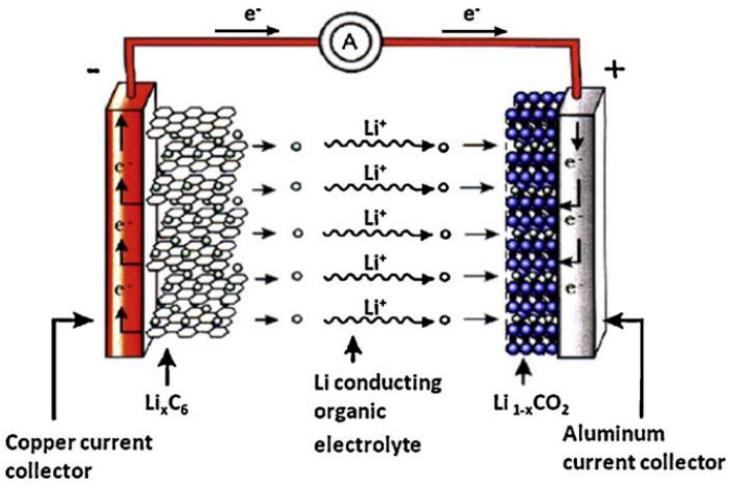

Figure 2.3: An illustration of a typical LIB. Reproduced with permission from Elsevier [12].

Lithium ions are extracted from the cathode during charging (delithiation), and they then diffuse through the electrolyte and separator before being reintroduced into the anode (lithiation). Additionally, the oxidized cathode generates electrons, which move through a circuit outside the cathode to the anode for the reduction reaction. The battery is fully charged when either the anode or cathode has undergone complete reduction or oxidation, respectively. The LIB is connected to an external load during the discharge process. After the anode has been oxidized, the migration of lithium ions to the cathode completes the reaction by creating electrons that flow to the external circuit (**Figure 2.4**). The electrochemical reactions can be expressed as follows when using graphite as the anode and lithium transition metal oxide as the cathode:

Cathode half-reaction: $Li_{1-x}MO_2 + xLi^+ + xe^- \leftrightarrow LiMO_2$ (2.1)

Anode half-reaction: $xLiC_6 \leftrightarrow xLi^+ + xe^- + xC_6$ (2.2)

Full cell reaction: $LiMO_2 + C_6 \leftrightarrow Li_{1-x}MO_2 + xLiC_6$ (2.3)

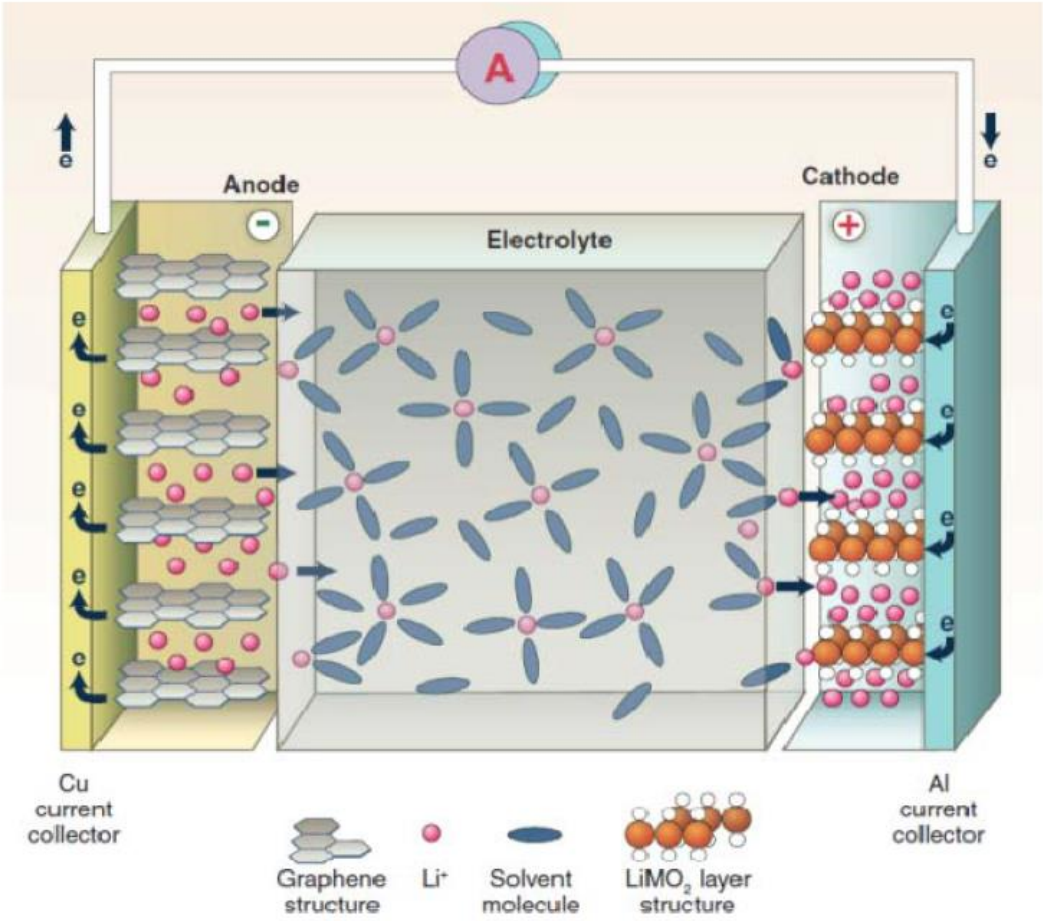

Figure 2.4: Diagram of a LIB, which has a positive electrode (Li-intercalation compound) and a negative electrode made of graphitic carbon. Reproduced with permission from MDPI [13].

Before moving on, it is crucial to define a few terms and express several fundamental equations used in the literature. The rate of flow of charge carriers through a surface or volume in a battery is represented by current (i) which is measured in amperes (A). **Equation 2.4** can be used to compute the current, where (i) is current, dQ is the change in

capacity, and dt is the change in time. **Equation 2.5**, where Q is the capacity, can be applied if the current is in a steady state. The amount of electricity produced, expressed in units of ampere-hours (Ah), is the capacity of a battery (Q). With values of $mAh.g^{-1}$, it is possible to compare the capabilities of various battery materials per unit mass. A battery's voltage (V), which is measured in volts, is the difference in electric potential between its two ends. Power (P) is the pace at which energy is delivered, whereas energy (E) is the capacity of a battery to carry out productive work. **Equation 2.6**, which assumes that the system is in a steady state, can be used to determine power, which is defined as the integral of the product of voltage and current in units of watts (W). **Equation 2.7** can be used to compute energy under the assumption that the system is in a steady state. Energy is defined as the integral of the product of voltage and capacity, or the product of power and time, with units of watt-hours (Wh). The gravimetric energy density (energy per mass with units of $Wh.kg^{-1}$) or volumetric energy density (energy per volume with units of $Wh.l^{-1}$) can be used to compare the energy storage capacity of batteries.

$$i = \frac{dQ}{dt} \qquad (2.4)$$

$$i = \frac{Q}{t} \qquad (2.5)$$

$$P = V \times i \qquad (2.6)$$

$$E = V \times Q = P \times t \qquad (2.7)$$

The cathode half-reaction and anode half-reaction potential differences, which in turn define the theoretical (maximum) voltage, depending on the cathode and anode active materials utilized. The amount of active material available, which determines the theoretical capacity, dictates the amount of electricity that is produced in a cell. The primary parameter of importance for the performance of electrode materials in LIBs is often "capacity" [11]. The charge per unit mass ($mAh.g^{-1}$) is denoted by this word, which also refers to capacity, gravimetric capacity, or mass capacity. This value is frequently used since it is simple to calculate with moderate precision and is crucial for applications that require weight. The term "mass" here refers simply to the mass of the active material

of the specific electrode, not to additional mass such as that from binders or collector foils. It's crucial for an electrode material to operate well in a variety of applications at a high enough mass loading. The "volumetric capacity" or charge per unit volume ($mAh.cm^{-3}$), which may be computed from the specific capacity, mass loading, and thickness of the active electrode material, is another term that is commonly used. As a result of each electrode being subjected to both charge and discharge, there are capabilities associated with each process, and they may vary greatly. The phrase "coulombic efficiency" (CE), which is represented in percent, refers to the ratio of the two processes' respective capacities in each cycle. In other words, the CE of a battery measure how much energy is withdrawn during discharge relative to how much is used during charging to replenish the battery's original capacity, which can be calculated by **Equation 2.8**.

$$CE(\%) = \frac{q_D}{q_C} \times 100 \qquad (2.8)$$

Where q is the specific capacity. The CE demonstrates the reversibility of the lithiation process. If the CE is less than 100%, some charge has been lost and used for processes other than the reversible lithiation/delithiation reactions. Examples include the irreversible trapping of Li in the host material and the development of solid electrolyte interphase (SEI) because of the electrolyte decomposing at low potentials. This irreversible capacity loss is only noticeable during the first few cycles, after which the lithiation process becomes more reversible, and the SEI layer has passivated the material's surface, resulting in very little irreversible capacity loss and high CE in the following cycles. It is important to remember that the electrolyte is reduced before lithiation in order to create the passivating SEI layer on the surfaces of the negative electrodes, which prevents electron transmission between the electrolyte and electrode [14]. **Equation 2.9**, which is presented below, can be used to calculate the theoretical specific capacity:

$$q = \frac{xF}{MW} \qquad (2.9)$$

Where x is the number of electrons involved in the electrochemical reaction, F is Faraday's constant, and MW is the molecular weight of the active material. For instance, **Equation 2.11** can be used to determine the theoretical specific capacity of graphite anode material, presuming that all the lithium can be extracted from the graphite as in **Equation 2.10**.

$$LiC_6 \leftrightarrow Li^+ + e^- + C_6 \qquad (2.10)$$

$$q = \frac{1\times 26801 \frac{mAh}{mol}}{6\times 12 \frac{g}{mol}} = 372 \ \frac{mAh}{g} \quad (2.11)$$

Thus, the specific capacity of the graphite is considered 372 mAh.g^{-1} at 1 C-rate. The rate at which a battery is charged or discharged is measured by the C-rate. The battery's 1 C-rate is the rate at which it is fully charged or discharged in an hour. The C-rate is expressed as follows:

$$C\ rate = \frac{1}{t} = \frac{i}{Q} \qquad (2.12)$$

Where i represents the charge/discharge current, Q represents the capacity, and t is the time in hours. For instance, a battery with a 1 C-rating and a 10 Ah capacity can be discharged at 10 A for an hour before it is completely discharged. The same battery can potentially be discharged at 0.5 C-rate for 2 hours with a current of 5 A or at 2 C-rate for 30 minutes with a current of 20 A before being completely discharged.

Only a small portion of a battery's theoretical energy is delivered practically. Concentration polarization (concentration gradient of reactants and products at electrode surfaces and bulk because of mass transfer), activation/charge-transfer polarization (activation energy for electrochemical reactions to occur at electrode surfaces), and internal impedance (which include electrolyte ionic resistance, electronic resistances of active materials, contact resistances between active materials and current collectors) in the cell can all result in the loss of energy. Ohm's rule is followed by these resistances, which causes a larger voltage drops at higher current densities [9]. The voltage V that results from connecting a cell to an external load R can be stated as follows:

$$V = V_0 - [(\eta_{ct})_a + (\eta_c)_a] - [(\eta_{ct})_c + (\eta_c)_c] - iR_i \quad (2.13)$$

Where V_0 is the cell's open circuit voltage, $(\eta_{ct})_a$ and $(\eta_{ct})_c$ are the anode and cathode activation polarizations, respectively, $(\eta_c)_a$ and $(\eta_c)_c$ are the anode and cathode concentration polarizations, respectively, i is the cell's operating current, and R_i is the cell's internal impedance.

2.1.2 Summary of Lithium-ion Battery Challenges

Despite the growth of the LIB industry, the specific energy of LIB is limited by the relatively low specific capacities of the current commercial cathode (lithium cobalt oxide, 140-170 mAh.g^{-1}) and anode (graphite, 372 mAh.g^{-1}) materials. Typically, from the perspective of the LIB market, both LIB makers and customer applications see an annual capacity increase of 5 to 8%. However, due to the limited availability of electrode materials in recent years, it is challenging to reach the necessary capacity. A higher cut-off voltage and a longer cycle life are two strategies several businesses are looking into to lower the cost of LIBs. However, increasing energy density for the next generation of LIBs remains challenging for scientists and researchers. The key to enhancing battery performance is to switch the active materials for the cathode and anode electrodes [9], [15], [16]. It took much work to create new materials with better specific capacities, like silicon for the anode and lithium nickel cobalt oxide ($Li_xNi_yCo_{1-y}O_2$) for the cathode.

Additionally, the safety of LIB is a crucial concern for large-scale applications, particularly in EVs and grid energy systems that require battery packs to operate at a larger capacity. To lessen the likelihood of any accident and limit damage before it occurs, the Battery Management System (BMS) was created. Numerous incidents involving LIBs have been documented elsewhere. The Boeing 787 Dreamliner experienced five accidents in seven days in January 2013, the majority of which concerned their backup batteries for the electrical system. Federal Aviation Administration (FAA) of the United States requested a review of the Boeing 787's development and production to address safety concerns. The end of 2014 has seen airlines placing new limits on the shipment of LIBs due to potential safety concerns. In

2013, there were 4 significant fire accidents involving Tesla EVs (Model S). Damage to the battery packs was responsible for this. It is therefore more crucial for LIBs to be made safer for their application to continue.

Due to its sophisticated production procedures, the LIBs market also faces difficulties with manufacturing costs. Basically, there are three formats available for modern LIBs: cylindrical cell, prismatic cell, and pouch cell. All of them have established manufacturing techniques, and since there is a fully automated production line, cylindrical cells (18650 format) have the highest production efficiency and the lowest cost. Additionally, cylindrical cells have continuous performance and do not swell, making them more dependable for battery packs. These advantages led Tesla to select cylindrical battery types for its EV application. Prismatic cells were the primary energy source for cell phones, but in recent years, pouch cells have quickly taken over the market, especially for smart phones, tablets, and other small portable devices. One of the key benefits is the variety of cell shapes, which can provide designers of new gadgets more creative freedom. Additionally, pouch cells are safe because they will not blast even under the most adverse conditions. In contrast to cylindrical and prismatic cells, however, the price is significantly higher due to more procedures and increased production efficiency. Due to the frequent changes in cell shapes, creating a fully automated production line is particularly challenging.

Also, each battery component, including the separator, current collectors, anode, electrolyte, and cathode, still has several problems that need to be fixed in addition to the aging problem. High electronic resistance, good ionic conductivity, resistance to electrode puncture, non-yielding and non-shrinkage of the material, an adequate pore size of less than one-micron, high electrolyte wettability, compatibility, and stability when in contact with electrodes and electrolyte are requirements for separators. Due to their excellent mechanical characteristics, chemical stability, and affordable price, microporous polyolefin materials like polyethylene or polypropylene are frequently employed [9]. Commercial polymer separators can thermally shut down at various temperatures by fusing into a film at high temperatures to prevent overheating or short circuits. However, they are useless at stopping challenging internal short circuits because

of manufacturing flaws. In general, polymer separators also experience significant shrinkage at high temperatures, but this shrinkage needs to be kept to a minimum to prevent electrode contact. Although composite/ceramic-enhanced separators have good electrolyte wettability and are more stable at higher temperatures, these benefits come at the expense of decreased tensile strength, increased separator weight, questionable electrochemical stability of the ceramic and its binder, and particle shedding because of insufficient binding to the polymer. Nonwoven mats have a low cost of production and strong stability, but their thickness lowers energy density, and their large pore diameters increase the possibility of shorting by lithium dendrites. Modifying polyolefin separators, creating alternative polymer membranes, and creating nonwoven mats employing nanoscale fibers are potential enhancement options [17].

High electrical conductivity, good mechanical strength, low weight/low density, cheap cost, and reasonable material sustainability are required for current collectors in addition to electrochemical stability against the redox conditions during battery cycling. Typically, copper and aluminum foils are employed as the current collectors for the cathode and anode, respectively. Aluminum (Al) is a good material for the cathode current collector because of its wide electrochemical stability window of 0.5–5 V versus Li^+/Li, high electrical conductivity, low density, and solid mechanical qualities. Although copper (Cu) is a desirable candidate for the anode current collector because of its strong electrical conductivity and stability up to 3.5 V vs. Li^+/Li, it is thick and may experience structural degradation after repeated cycling under bending stress. While lighter weight and higher energy densities will result from using thinner current collectors, a trade-off results in decreased electrical conductivity, less efficient heat transfer, and ultimately lower power densities. So, the design must strike a balance between energy and power density. Current collectors must stick to electrodes to collect electrons and give mechanical support, but the adhesive's tenacity also increases the battery's internal contact resistance. Thus, it should be kept to a minimum. In addition, the internal resistance of the current collector is substantially lower than the contact resistance between the electrode and the current collector. Therefore, great effort has gone into changing the surface to reduce contact resistance. Numerous enhancement methods have been investigated, including using

mesh and foam current collectors, chemical etching and coating to change the surface, and employing additional materials, including carbonaceous materials and stainless steel [18].

Anodes must have a low potential roughly equivalent to lithium metal, little structural change during cycling, reactions with lithium ions that can be reversed, a high diffusivity of lithium ions, high density, and the ability to store a lot of charge per mass [19]. Graphite is frequently utilized because of its excellent conductivity, low cost, limited dendrite growth, and good reversibility. However, graphite has limited energy density due to the need for six carbon atoms to hold one lithium atom and is chemically sensitive to electrolytes. Additionally, the surface structure is frequently damaged during cycling, which results in low first CE and poor rate capability. There are issues with other carbon-based compounds as well. Additionally, the theoretical capacity of materials based on carbon has almost been attained. Carbon composites and other materials have been developed to get around the energy density limitation. Theoretically, silicon and tin-based materials offer large capacities, but suffer from significant volume expansion during cycling, which causes electrode pulverization and poor cyclability. Although lithium metal has a significant theoretical capacity and the lowest electrochemical potential, it has a low CE after repeated cycling and lithium dendrite formation, which raises safety hazards. Doping, coating, interface design, microstructure/nanostructure design, and synthesis methods are just a few improvement tactics for anodes that are being researched [20], [21].

High chemical and electrochemical stability toward electrodes, high ionic conductivity, a wide temperature operating range, a high level of safety, and low cost are among the electrolyte requirements [19]. It is ideal for electrolyte salts to completely dissolve in the solvent, be preferentially water-stable, encourage the creation of stable and ionically conducting interfacial layers at electrodes, and have an inert and stable anion against decomposition at electrodes. Lithium salts should be sufficiently dissolved by ideal electrolyte solvents, which should also have low viscosity to guarantee quick Li-ion diffusion, good wettability on electrodes and separators, stability against cell components, and the ability to remain liquid across a wide temperature range [22]. The

typical electrolyte used in LIBs is a liquid mixture of lithium salts (such as $LiPF_6$) and organic solvents (such as carbonates, esters, and ethers) [9]. However, due to their volatility, flammability, and narrow temperature operating range (between 0 and 60 degrees Celsius), these liquid mixtures can negatively affect safety and performance [23]. Numerous studies have been conducted to enhance electrolytes' functionality and address existing problems. A tiny amount of electrolyte additions (about 5% by weight/volume) is required to significantly increase LIB performance, making them an easy and affordable option [24]. Additionally, research is being done on new and alternative electrolytes. Ionic liquid electrolytes offer a high degree of thermal stability and are composed of liquid salts at room temperature, but they are also quite viscous, operate poorly at low temperatures, and can be expensive. Gel polymer electrolytes are made of a liquid electrolyte embedded in a polymer matrix. They have characteristics of both liquid and polymer electrolytes, including a fair amount of ionic conductivity, low temperature performance, and thermal stability [19]. Although SSEs do exist and offer benefits like a higher level of safety, a wider temperature tolerance range (between -30 and 100 degrees Celsius), and a higher energy density, the technology is still in its early stages and at the moment has problems like lower ionic conductivity, high interfacial resistance, contact issues with electrodes, and poor cycling stability [23].

Currently, the LIBs utilized in EVs offer volumetric energy densities of 650 $Wh.L^{-1}$ and gravimetric energy densities of around 250 $Wh.kg^{-1}$ [25]. The volumetric and gravimetric energy densities of EVs need to be at least 750 $Wh.L^{-1}$ and 350 $Wh.kg^{-1}$, respectively, in order for them to operate similarly to ICEs [7]. The cathode, the most significant component by both cost and weight in modern LIBs, is one of the main obstacles to achieving the energy density target, which breaks down the cost and mass for a typical LIB. To reach the cell-specific energy level of 350 $Wh.kg^{-1}$, it is estimated that at least 800 $Wh.kg^{-1}$ is needed from the cathode active material, so higher energy density cathode materials are needed. The price of cathode materials must decrease in order for EVs to compete well with ICE vehicles (100 USD kWh^{-1}) in order to win over more customers [25]–[27].

As mentioned, conventional LIBs suffer from low energy density and safety concerns. These two factors motivate researchers to find suitable alternatives for typical LIBs. Solid-state batteries present higher energy density and safety levels, so they can be considered appropriate substitutes for next-generation ESSs.

2.2 Introduction to All-Solid-State Lithium-ion Batteries

All-solid-state lithium-ion batteries (ASSLIBs) have become one of the most promising energy storage technologies to achieve the highest safety and energy density levels. Also, by arranging many cells in a stack, a larger volumetric energy density can be attained [28]–[31]. It is predicted that the device would significantly support the reliable, long-term operation of EVs as well as the balanced exploitation of renewable energy sources without posing any fire risk owing to the use of non-flammable inorganic solid electrolytes [28], [32]–[37].

An ASSLIB is depicted schematically in **Figure 2.5** as having a cathode, electrolyte, anode, and current collectors as its constituent parts. The electrolyte is essential to ASSLIBs. It serves as an ionic conductor and separator at the same time. It is evident that the electrodes are connected to the electrolyte's two sides. Compared to typical LIBs with liquid electrolytes, this arrangement is more straightforward. There are fewer packaging requirements for ASSLIBs, which might drastically lower the cost of production [38].

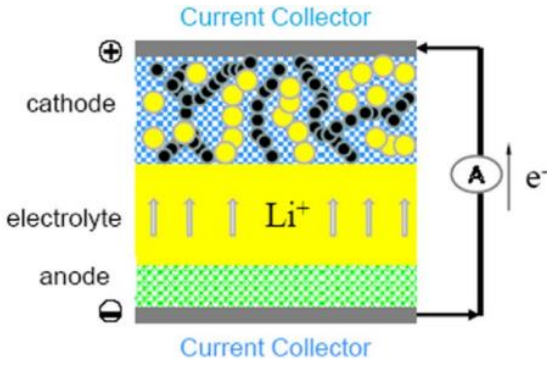

Figure 2.5: Schematic representation of an ASSLIB based on Li-ion conduction. Reproduced with permission from Elsevier [38].

2.2.1 State-of-the-Art Solid-State Electrolytes

A solid-state electrolyte (SSE) is a necessary component to achieve ASSLIBs. The ability of solid electrolytes to conduct ions is a crucial characteristic. However, other qualities are equally crucial for their practical use in electrochemical energy storage and conversion systems. SSEs must have several key characteristics in order to function correctly, including high ionic conductivity, low ionic area-specific resistance, high electronic area-specific resistance, high ionic selectivity, a wide electrochemical stability window, good chemical compatibility with other components, excellent thermal stability, excellent mechanical properties, simple fabrication processes, low cost, easy device integration, and environmental friendliness [39]–[43]. Systematic research is essential for developing solid electrolytes with these exceptional properties to realize such an ideal using high-performance ASSLIBs [44]–[46]. The development of highly Li^+-conductive SSE has received much attention over the past few decades, with oxide electrolytes, sulfide electrolytes, and polymer electrolytes among the examples [32], [47].

Thanks to their exceptional qualities, numerous solid electrolytes have demonstrated significant potential for high-performance ASSLIBs. For instance, the ionic conductivities of sulfide-based solid electrolytes like Li_6PS_5X (X: Br, Cl) and $Li_{10}GeP_2S_{12}$ reached the level of conventional liquid electrolytes, and halide-based solid electrolytes like $Li_2Sc_{2/3}Cl_4$ and Li_3MCl_6 (M = In, Y, Er) exhibited superior electrochemical stability to reversibly operate high voltage cathodes [31], [48]. In particular, sulfide and oxide-based solid electrolytes have been extensively studied and tested for high-performance ASSBs [29], [49]. The sulfide-based solid electrolytes typically have high ionic conductivity, a mechanically adaptable interface, and high deformability; however, due to their limited electrochemical stability and high chemical reactivity with polar components, these properties must be overcome with additional electrochemical treatments [31], [50], [51]. In contrast, the oxide-based solid electrolytes support greater electrochemical stability but comparatively low ionic conductivity and processability due to their mechanically rigid and brittle characteristics, which must be considered to produce high-performance ASSBs [52]–[54].

2.2.1.1 Sulfide Solid Electrolytes

One of the requirements for developing high-performance ASSLIBs is the sulfide electrolytes' strong ionic conductivity. It should be noted that some representative sulfide electrolytes already have higher ionic conductivities than those of traditional liquid organic electrolytes (10.2 $mS.cm^{-1}$ for 1 M $LiPF_6$, EC/DMC) [55], such as $Li_{9.54}Si_{1.74}P_{1.44}S_{11.7}Cl_{0.3}$ (25 $mS.cm^{-1}$) [31], $Li_{10}GeP_2S_{12}$ (12 $mS.cm^{-1}$) [47], and $Li_{3.45}[Sn_{0.09}Si_{0.36}]P_{0.55}S_4$ (11 $ms.cm^{-1}$) [56]. Prior to the successful commercialization of sulfide electrolytes in ASSLIBs, additional requirements for sulfide electrolytes must be met, including: (1) low electrical conductivity to prevent self-discharge behavior on shelves; (2) low cost; (3) a wide electrochemical window to allow the adoption of high-voltage cathodes and high capacity anodes (such as Li metal); and (4) excellent air stability, which enables the process of sulfide electrolytes in dry rooms with a dewpoint (-50 °C ~ -70 °C) [57], [58].

With a chemical formula of $Li_{10\pm1}MP_2X_{12}$, (M = Ge, Si, Sn, Al or P, and X = O, S or Se) and a strong ionic conductivity, the thio-LISICON family has attracted the attention of material scientists [55]. Ryoji Kanno's 2001 study on the thio-LISICON system is the first of its kind in history. By merely sintering the initial materials (Li_2S, GeS_2, and P_2S_5) at 700 °C for 8 hours, they achieved an ionic conductivity of 2.2×10^{-3} $S.cm^{-1}$ at 25 °C [59]. $Li_{10}GeP_2S_{12}$ (LGPS), which demonstrated an exceptional conductivity of 1.2×10^{-2} $S.cm^{-1}$ at ambient temperature, was the superionic lithium conductor Kamaya et al. disclosed in 2011 with the ongoing efforts. The crystal structure of LGPS was precisely studied using synchrotron X-ray diffraction (XRD) and neutron diffraction measurements. **Figure 2.6a** depicts the three-dimensional (3D) framework structure and one-dimensional (1D) lithium conduction path of this superionic conductor shown in **Figure 2.6b**. The LiS_4 tetrahedra in the 16h and 8f sites, which have a shared edge and form a 1D tetrahedron chain, make up the 1D conduction channel. The LiS_4 tetrahedron's common corners serve as these chains' connecting links, as shown in **Figure 2.6c** [47].

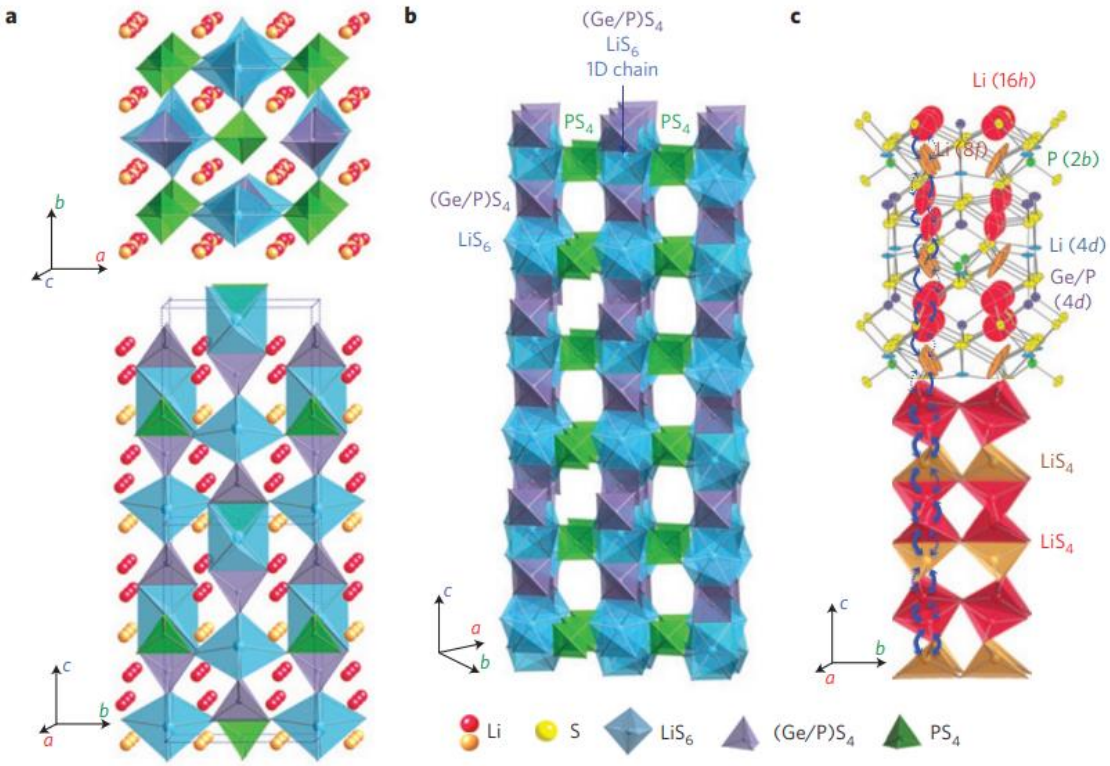

Figure 2.6: Crystal structure of LGPS. (a) The framework structure and lithium ions that participate in ionic conduction. (b) Framework structure. (c) Conduction pathways of lithium ions. Reproduced with permission from Nature Materials [47].

Deiseroth et al. were the first to synthesis the argyrodite-type Li-ion solid electrolytes Li_6PS_5X (X = Cl, Br, I) with a Li^+ mobility that is exceptionally high. [60]. Following that, they carried out a series of studies using solid-state NMR, impedance spectroscopy, and molecular dynamics simulation [61]–[63] to examine the structure, phase transition, and lithium-ion conduction of lithium argyrodites. They discovered that these materials have three-dimensional lithium-ion conduction pathways [64], [65]. According to Virginie Viallet et al., the ionic conductivities of Li_6PS_5Cl, Li_6PS_5Br, and Li_6PS_5I at room temperature are 6.2×10^{-4} S.cm^{-1}, 4.6×10^{-4} S.cm^{-1}, and 1.9×10^{-4} S.cm^{-1}, respectively [66]. The halogen argyrodites also exhibit remarkable electrochemical stability from 0 to 7 V vs. Li^+/Li and a low electronic conductivity on the order of 10^{-10} S.cm^{-1}, in addition to their excellent ionic conductivity [66], [67]. To investigate the cause of the lithium-ion conductivity in argyrodite solid electrolytes, Marnix Wagemaker et al. used density functional theory

molecular dynamics simulations. They discovered that the Li-ion diffusion of Li_6PS_5Cl and Li_6PS_5Br is significantly influenced by halogen atoms and lithium-ion vacancies, among other factors [68].

Glass and glass-ceramic Li_2S-P_2S_5 solid electrolytes were the focus of research for sulfide-type solid electrolytes prior to the invention of ceramic thio-LISICON solid electrolytes [69], [70]. Mizuno et al. advanced ceramic, glass, and glass-ceramic $70Li_2S$-$30P_2S_5$ solid electrolytes. High ionic conductivities of 5.4×10^{-5} $S.cm^{-1}$ and 3.2×10^{-3} $S.cm^{-1}$ were observed for the glass and glass ceramic samples, respectively, at room temperature. However, the ionic conductivity of the ceramic sample made via solid-state reaction was only 2.6×10^{-8} $S.cm^{-1}$ at ambient temperature, and low conductive Li_3PS_4 and $Li_4P_2S_6$ phases were found [71]. Glassy superionic conductors have several benefits over crystalline solid-state sulfide electrolytes, including isotropic ion migration properties, a wide range of chemical composition options, and ease of controlling properties while altering chemical composition [72]–[74]. In general, glass has a higher ionic conductivity than comparable crystal because glass typically has a large free volume [72]. Additionally, heating a glass above the glass transition (T_g) point makes it simple to generate a metastable phase, which is thermodynamically unstable at a specific temperature [75]. In the case of crystallization from AgI-Ag_2O-M_xO_y (M = B, Ge, P, Mo) glasses with incredibly high AgI concentrations, the high-temperature superionic phase of α-AgI was successfully precipitated and stabilized in a glass matrix to obtain an incredibly high ion conductivity of 10^{-1} $S.cm^{-1}$ at room temperature [76], [77].

2.2.1.2 Oxide Solid Electrolytes

$A_3B_2(XO_4)_3$ is the general formula for garnet-type compounds (A = Ca, Mg, Y, La, or rare earth; B = Al, Fe, Ga, Ge, Mn, Ni, V; X = Si, Ge, Al), where the A and B cations have 8-fold and 6-fold coordination, respectively. Thangadurai et al. were the first to report a new class of rapid Li-ion conducting oxides with garnet-like structures, $Li_5La_3M_2O_{12}$ (M = Nb, Ta) [78]. Chemical substitutions or structural changes were used to develop conductivity in the years after continuously. Murugan et al. produced a novel garnet-type material with a molecular composition of $Li_7La_3Zr_2O_{12}$ (LLZO) with ionic

conduction of 3×10^{-4} S.cm^{-1} at room temperature in 2007 [79]. Due to their comparatively high ionic conductivity and good chemical stability against Li-metal anode, LLZO and its derivatives have been actively explored for all-solid-state lithium-metal battery construction since then. Years later, Awaka et al. used single-crystal X-ray structural analysis to identify the detailed crystal structure of cubic LLZO (**Figures 2.7a and 2.7b**). In the garnet-type framework structure, a 3D network of the Li-ion migration channel with short Li-Li distance and occupational disordering was discovered. The Li1 and Li2 sites form a loop, the pathway's basic unit [80]. Garnet-type solid electrolytes exhibit excellent ionic conductivity and a wide electrochemical window; nevertheless, when exposed to moisture, they perform the Li^+/H^+ exchange at room temperature, resulting in an insulating Li_2CO_3 coating layer [81].

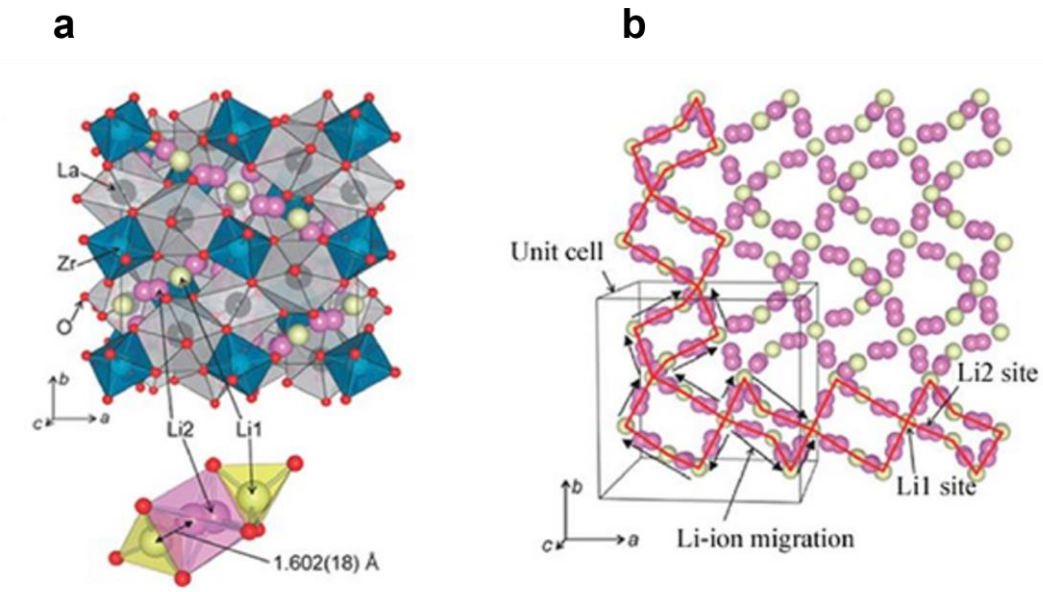

Figure 2.7: (a) $Li_7La_3Zr_2O_{12}$ Cubic crystal structure. (b) Li atomic configuration in cubic three-dimensional conducting network $Li_7La_3Zr_2O_{12}$. Reproduced with permission from Chemical Society Japan [80].

$Li_{1+x}Al_xTi_{2-x}(PO_4)_3$ (LATP) and $Li_{1+x}Al_xGe_{2-x}(PO_4)_3$ (LAGP) are crystalline phosphates with NASICON-type structures that are known to be excellent Li-ion conductors with high ionic conductivities of 7×10^{-4} S.cm^{-1} at room temperature, a wide electrochemical window of 6 V, and good stability in moist environments. Commercialized LATP might

have a conductivity of up to 1.3×10^{-3} $S.cm^{-1}$. These NASICON-type electrolytes are unstable with Li-metal anodes [82].

$Li_{3x}La_{2/3-x}TiO_3$ (LLTO) was the first perovskite-type solid electrolyte that Inaguma et al. developed, and it had bulk ionic conductivity of 1×10^{-3} $S.cm^{-1}$ and total ionic conductivity of more than 2×10^{-5} $S.cm^{-1}$ at ambient temperature for $Li_{0.34(1)}La_{0.51(1)}TiO_{2.94(2)}$ [83]. **Figure 2.8** depicts the crystal structure of LLTO, with Li and La ions occupying the center A sites and Ti ions occupying the corner B sites. Li-ions may encounter potential obstacles when moving from one A site to another due to oxygen ions' formation of bottlenecks. Many attempts were made to increase the lattice parameters of the perovskite-type solid electrolytes because modifying the lattice parameters can alter the size of bottlenecks [84].

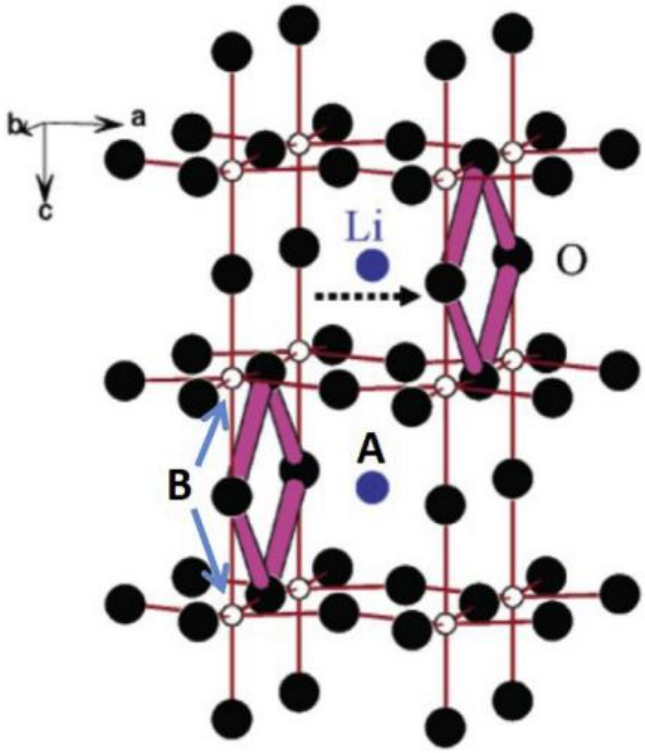

Figure 2.8: Crystal structure of perovskite-type solid electrolytes LLTO. Reproduced with permission from the American Chemical Society [84].

2.2.1.3 Halide Solid Electrolytes

Three categories can be used to group the solid halide electrolytes that have already been discovered: those with group 3 elements (Sc, Y, and La-Lu), group 13 elements (Al, Ga, and In), and divalent metals (e.g., first transition metals) are these three categories. Among these, a few substances in the first two groups displayed acceptable Li^+ conductivities greater than 10^{-4} $S.cm^{-1}$ [85]. According to Asano and coworkers, trigonal Li_3YCl_6 and monoclinic Li_3YBr_6 exhibited strong Li^+ conductivities, with values of 0.51 and 1.7 $mS.cm^{-1}$, respectively. These high Li^+ conductivities are hidden in the tenuous connection between the monovalent halide anion and Li^+ [86]. However, the benefits of both sulfide and oxide solid electrolytes are coupled in solid halide electrolytes, particularly chloride compounds, for the following reason: good (electro)chemical stability while being deformable [85]–[87].

By switching the perovskite system from $A^+B^{2+}X_3^-$ to $A^-B^{2-}X_3^+$, where the A site atom is a halogen (F, Cl, Br, I) or a combination of halogens, the B site atom is oxygen, and the X site atom is lithium, anti-perovskite-type solid electrolytes were created and constructed. Li_3OCl and Li_3OBr displayed conventional perovskite structures, and $Li_3O(Cl_{1-z}Br_z)$ may be created by solid solutions between the two end members. At room temperature, Li_3OCl and $Li_3OCl_{0.5}Br_{0.5}$ displayed ionic conductivities of 8.5×10^{-4} $S.cm^{-1}$ and 1.94×10^{-3} $S.cm^{-1}$, respectively. $Li_3OCl_{0.5}Br_{0.5}$ had a more excellent ionic conductivity because it could prevent structural distortion in Li_3OCl and the limited Li-ion hopping interstitial space in Li_3OBr [88].

The solid electrolytes that have been addressed are summarized in **Table 2.1**, and the radar plots in **Figure 2.9** show how these solid electrolyte materials' properties can be seen.

Table 2.1: Summary of lithium-ion solid electrolyte materials [29].

Type	Materials	Conductivity ($S.cm^{-1}$)	Advantages	Disadvantages
Sulfide	Li_2S-P_2S_5, Li_2S-P_2S_5-MS_x	10^{-7} – 10^{-3}	High conductivity Good mechanical strength and mechanical flexibility Low grain-boundary resistance	Low oxidation stability Sensitive to moisture Poor compatibility with cathode materials
Oxide	Perovskite, $Li_{3.3}La_{0.56}TiO_3$, NASICON $LiTi_2(PO_4)_3$, LISICON $Li_{14}Zn(GeO_4)_4$, And garnet $Li_7La_3Zr_2O_{12}$	10^{-5} – 10^{-3}	High chemical and electrochemical stability High mechanical strength High electrochemical oxidation voltage	Non-flexible Expensive large-scale production
Halide	LiI, spinel Li_2Zn_4I and anti-perovskite Li_3OCl	10^{-8} – 10^{-5}	Stable with lithium metal Good mechanical strength and mechanical flexibility	Sensitive to moisture Low oxidation voltage Low conductivity

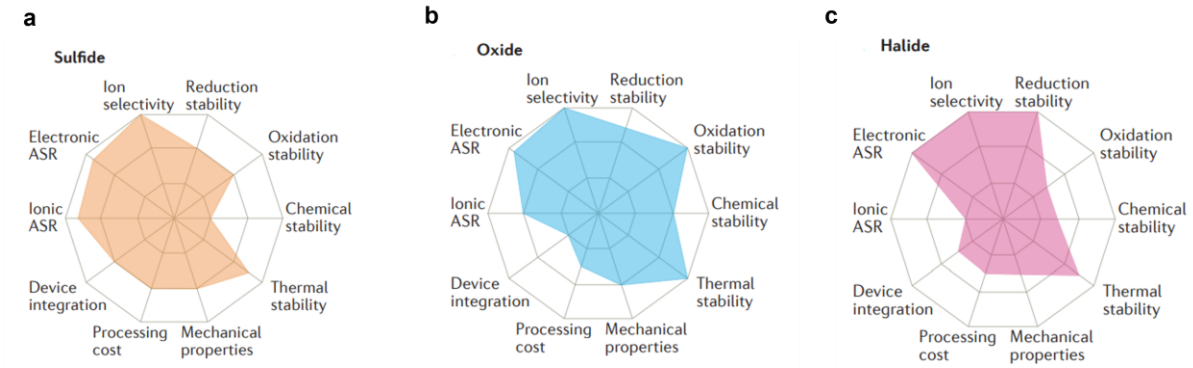

Figure 2.9: Radar plots of the performance properties of (a) sulfide solid electrolytes, (b) oxide solid electrolytes, and (c) halide solid electrolytes. ASR, area-specific resistance. Reproduced with permission from Nature Reviews Materials [29].

2.2.2 Electrode/Electrolyte Interface

It is commonly acknowledged that the characteristics of the electrode/electrolyte interface have a significant role in the performance of LIBs in addition to the electrode and electrolyte. One of the main issues with ASSLIBs is high interfacial resistance. The high interfacial resistance in ASSLIBs is because of numerous factors: the interface's active surface area is significantly less than conventional cells, where the liquid electrolyte soaks into the electrode pores and improves active material contact. However, this is not true for a solid electrolyte, as the interfacial resistance is substantially increased. Additionally, because the interface resides between two materials, damage to this region is exacerbated by electrode volumetric changes during lithiation and delithiation cycles [89]. A surface layer development was seen for ASSLIBs even though solid electrolytes have a far larger electrochemical stability window than liquid electrolytes. This surface layer can significantly increase the interfacial resistance.

2.2.2.1 Surface Layer Formation

In liquid electrolyte cells, a solid electrolyte interphase (SEI) is created on the surface of the negative electrode during the initial charge/discharge cycles. The creation of SEI results from a mismatch between the anode's electrochemical potential and the liquid

electrolyte's electrochemical stability window. As a result, when the electrolyte touches the anode's active material, it is diminished, leading to the anode's breakdown. The reduction products finally deposit on the electrode's surface, leading to the SEI's formation. An irreversible capacity loss in the battery's initial cycles can be used to track the development of this thin, solid layer. Today, it is well acknowledged that the SEI's creation is crucial to the function of the cell and must be excellent and controlled. Lithium ions can pass through the coating, but electrons cannot. As a result, the layer exhibits characteristics of a solid electrolyte [90], [91].

Compared to liquid electrolyte cells, significantly less research has been done on the interfacial chemistry of ASSLIBs. This might be caused by the solid electrolyte having stronger chemical and electrochemical stability than is often believed. Additionally, the film is securely bonded to the electrode, making it more challenging to conduct investigations at the interface between the two solid layers. However, electrochemical impedance spectroscopy (EIS) has shown interfacial resistance after cell assembly. This was explained by numerous investigations of the development of a passivation film on the electrodes' surface. The creation of an ionically conducting passivation film between a lithium electrode and a PEO/$LiCF_3SO_3$ electrolyte was first described by Fautex in 1984. He claimed this film would function as a SEI comparable to liquid electrolyte systems [92], [93].

Following that, attempts were made to describe the film creation mechanism and composition. It is crucial to remember that neither is fully understood at this time. In addition, the processing parameters and unique chemistry of the system under study significantly impact the surface layer. Most research has focused on the interface between a lithium anode and a solid electrolyte, and there is very little literature on developing a passivation layer on alternative electrode materials [94].

2.2.2.2 Reduction of the Interfacial Resistance

The interfacial resistance has been reduced using a variety of methods. The most widely used method is the addition of filler particles to the solid electrolyte. Fillers were studied to reduce interfacial resistance and improve the bulk electrolyte's electrical

characteristics. Increasing the contact between the active material particles in the electrode and the solid electrolyte would minimize the interfacial resistance and prevent the formation of a surface layer. Temperature and pressure can be regulated to accomplish this. However, this is constrained by the solid electrolyte's mechanical characteristics and the environment in which it is used. Thin films of the appropriate electrodes are utilized to improve the surface area between the electrodes and the solid electrolyte. Charge transmission to deep active material particles continues to be one of the most challenging problems in the field of ASSLIBs [95].

2.2.3 Solid-State Electrodes

The design of the electrode and the creation of new solid electrolyte materials can significantly impact the electrochemical characteristics of the ASSBs. Therefore, developing new and effective electrode materials is essential for creating ASSBs with high energy densities. A review of the electrode materials in LIBs is provided in this section. After giving an overview of the conventional anode and cathode active materials in the beginning, the structure of the composite and diffusion-dependent electrodes is given. Here, a specific focus is attributed to diffusion-dependent Gr/P and HC electrodes, representing this work's electrode structure and materials.

2.2.3.1 Anode Active Materials

Anode materials for LIBs made of pure lithium metal were first studied. Out of all the options suggested, it has the best standard potential and significant specific capacity (3861 $mAh.g^{-1}$). However, metallic lithium has proven to be risky for rechargeable batteries since it causes dendritic growth on the anode's surface while charging, raising the chance of internal short-circuiting, ensuing thermal runaway, and resulting in an explosion. Significant work has been done to make it possible to employ lithium metal in rechargeable batteries. Solid electrolytes, for instance, could potentially offer a way to reduce the hazards to safety because they have a high degree of mechanical robustness and can inhibit the growth of lithium dendrites. Despite this, primary (non-rechargeable) LIBs are the only devices utilizing lithium metal as the anode's active material [96].

Figure 2.10 provides an overview of the most investigated anode-active materials and information on their distinctive capacities and potentials.

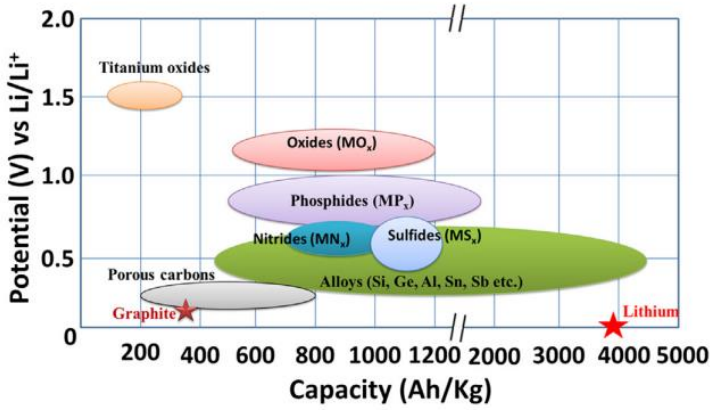

Figure 2.10: Potential as a function of gravimetric capacity for popular anode active materials. Reproduced with permission from Elsevier [97].

2.2.3.2 Cathode Active Materials

Since the cathode is the most expensive and heavy component in conventional LIBs, there have been many studies into next-generation cathode materials recently. **Figure 2.11** compares the current most widely studied cathode materials in terms of theoretical specific capacity, working voltage, compacted density, rate capability, cycle performance, and high-temperature performance. Intercalation materials are a class of materials that include the commercially available and most researched next-generation cathode materials. While layered, spinel, and olivine structures are the traditional representatives in this area, new intercalation compounds have recently been developed. Attention has recently been drawn to the conversion of cathode materials [98].

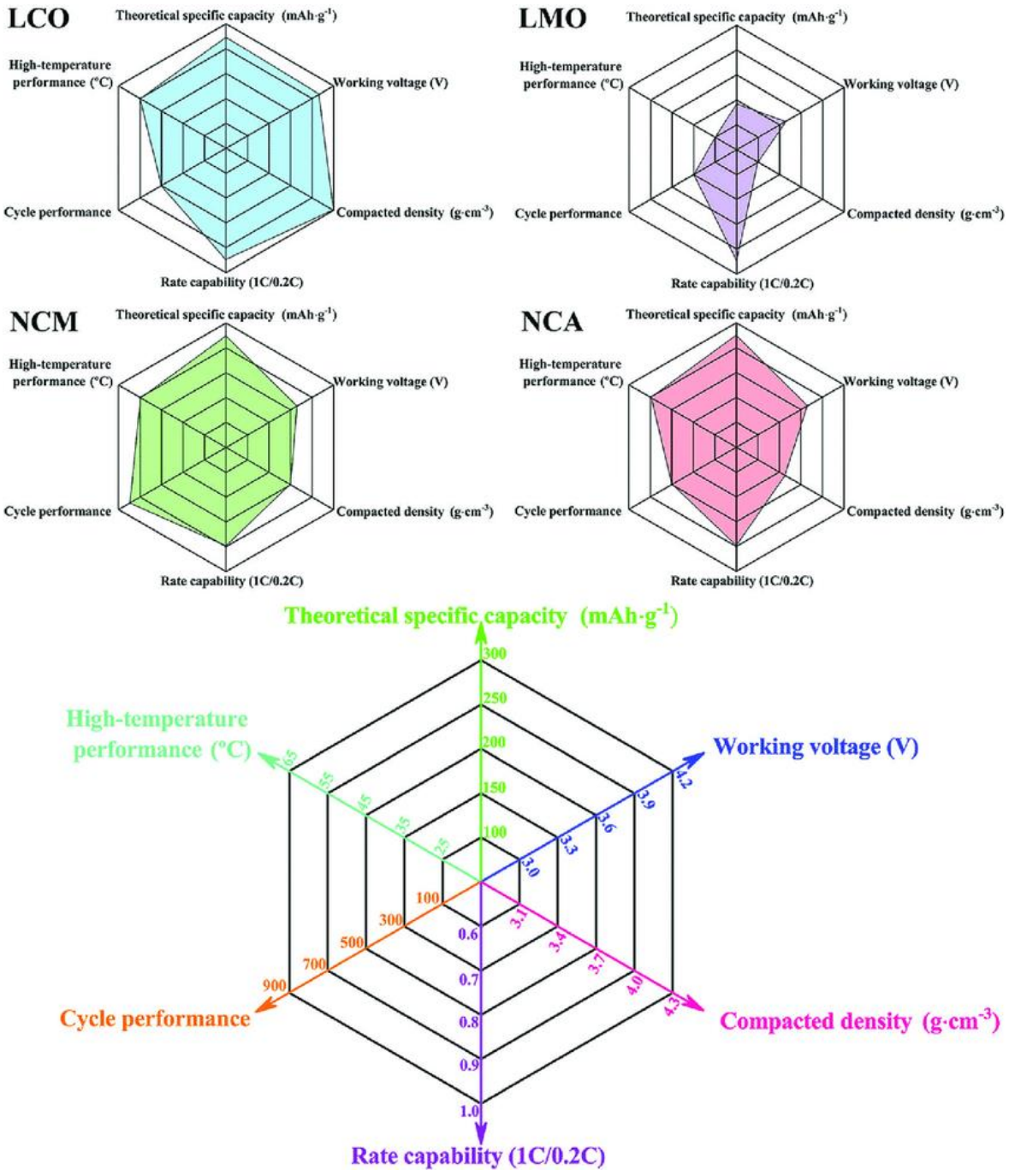

Figure 2.11: Performance comparison of active cathode materials. Reproduced with permission from Chemical Society Reviews [98].

2.2.3.3 Composite Electrode

The all-solid-state electrode design has been improved to exploit the active material's potential better while minimizing ionic resistance within the electrode. This goes hand in hand with the development of the intrinsic properties of materials [99]. Every solid-state battery uses the solid electrolyte in two parts as a standard. In order to efficiently transport lithium ions between the two electrodes while avoiding direct electrical shorting, a solid electrolyte layer between the cathode and the anode must first be constructed using solid electrolyte powders [100]–[103]. In addition, the solid electrolyte is included in the composite electrode made of active materials, providing lithium-ion transport pathways in the solid-state electrodes [99], [104]–[107].

To construct the lithium ionic and electronic conduction routes in the electrode layers of typical ASSBs, mixtures made of active material, solid electrolyte, and carbon conductive additive powders are frequently used. Additionally, most ASSBs described so far include a thick electrolyte layer acting as a separator and a thin electrode layer with a tiny amount of active materials. As a result, ASSBs now have an energy density significantly lower than normal LIBs [108]. A significant increase in energy density is greatly sought for the massive implementation of ASSBs. Two approaches might be used to achieve this goal: one is to use high-capacity electrode materials, and the other is to increase the amount of active materials in electrode layers [109]. In contrast to liquid-type LIBs, the demand for next-generation electrode materials is distinct in ASSBs. The development of the electrode-electrolyte interface and the design of advantageous lithium ionic conduction pathways in the electrode layers are the aspects of ASSBs that are crucial for their operation. It is required to use a significant amount of highly moldable solid electrolytes to produce superior electrode/electrolyte interfaces with large contact areas and good lithium ionic conduction pathways in the electrode layer. However, by raising the amount of electrolytes, the active material content should be reduced, which results in a reduction in energy density. As a result, improving energy density requires the development of active materials with favorable ductility and high ionic conductivity in addition to high capacity [109].

In typical LIBs, a permeable liquid electrolyte fills the electrode's pores, facilitating the transit of lithium ions within the electrode, but this is challenging to achieve in ASSBs. Composite electrodes with properly mixed active material and solid electrolytes solved this issue. In other words, throughout the electrode manufacturing process, the all-solid-state electrode should prepare ionic transport media for simple ion migration to the active material. The construction of well-percolated ionic routes in this context depends on the morphological alteration of solid electrolyte particles. Lithium-ion conduction in the electrode is made simple by controlling the size ratio of the solid electrolyte and active material particles, which improves the chance that they will come into close contact with one another [99], [104]. A well-designed ionic percolation is also facilitated by using solid electrolytes with more excellent aspect ratios, such as wires or plates [110]. Furthermore, the solid electrolyte in the composite electrode should be carefully coupled with a compatible binder and solvent since the commonly used sulfide solid electrolytes demonstrated considerable vulnerability to polar solvents, leading to a limited number of binder-solvent combinations [111], [112]. More interestingly, due to considerable breakdown reaction between the solid electrolyte and active materials or carbon additives, significant capacity fading was frequently seen in the composite electrodes [113]–[117].

Recently, a novel theory for diffusion-dependent solid-state electrodes has been put out in which the electrode is constructed without the addition of SSE.

2.2.3.4 Diffusion-dependent Electrode

Diffusion-dependent electrode structure increases energy density while allaying worries about chemical reactivity between inorganic SSEs and solvents/binders, which are necessary to produce sheet-type electrodes [118]. In addition, many problems brought on by composite electrodes are avoided, including side reactions at the interface between electrode materials and SSEs, SSE breakdown brought on by carbon additions, and additional surface coating on active materials. Despite the greater temperature (60~80 °C) needed to promote Li-ion diffusion in diffusion-dependent electrodes, these electrodes have shown the higher areal capacity and better cycling stability compared to the traditional composite electrodes [109], [116], [119], [120].

In the diffusion-dependent electrode, interparticle ionic diffusion via active material particles can create a practical path for lithium-ion transport within the entire electrode, provided that the active material particles form a uniform interface with one another. The active material mechanically compliant with the applied pressure is preferable in this respect. As a result, graphite and titanium disulfide are acceptable materials for diffusion-dependent electrode configuration in this regard. Furthermore, carbon additives have been eliminated for active materials like graphite with a high enough electron conductivity [118], [119]. It is preferable for the overall lithium-ion diffusion length to be as short as feasible for the diffusion-dependent electrode to operate well. Therefore, it is vital to consider the (de)lithiation direction concerning the morphologies of the active material particles to reduce the tortuosity for lithium-ion transport in the electrode [119], [121]. Furthermore, a thin electrode may be preferable to an overly thick electrode for quick charge/discharge. Although the physical dimensions and diffusivity of the active materials should be rigorously examined, it stands to reason that using active materials with a large volumetric capacity should be highly effective and produce a high normalized capacity [122].

The development of diffusion-dependent solid-state cathodes and anodes has received much attention because of these benefits. In this case, $Li_2Ru_{0.8}S_{0.2}O_{3.2}$, developed by A. Sakuda et al., is an ion and electron mixed conductor that may serve as the cathode material for ASSBs without the need for additional carbon additions or SSEs as shown in **Figure 2.12a**. The diffusion-dependent and conventional composite electrodes are compared schematically in **Figure 2.12a** and **Figure 2.12b**. Under a current density of 0.64 $mA.cm^{-2}$, the diffusion-dependent electrode performs satisfactorily in terms of rate and has a significant reversible capacity of around 200 $mAh.g^{-1}$, as shown in the **Figure 2.12c**. This capacity is more than the theoretical capacity of $Li_2Ru_{0.8}S_{0.2}O_{3.2}$ (141 $mAh.g^{-1}$), which is attributed to the anionic oxygen redox reaction and the Ru^{5+}/Ru^{4+} redox reaction. An anionic oxygen redox reaction is reversible, as evidenced by the CE, which can reach 99.8%. The strong reversibility of the $Li_2Ru_{0.8}S_{0.2}O_{3.2}$ diffusion-dependent electrode in ASSBs is further revealed by the overlap and negligible voltage decline of charge/discharge curves at various cycles shown in **Figure 2.12d** [109].

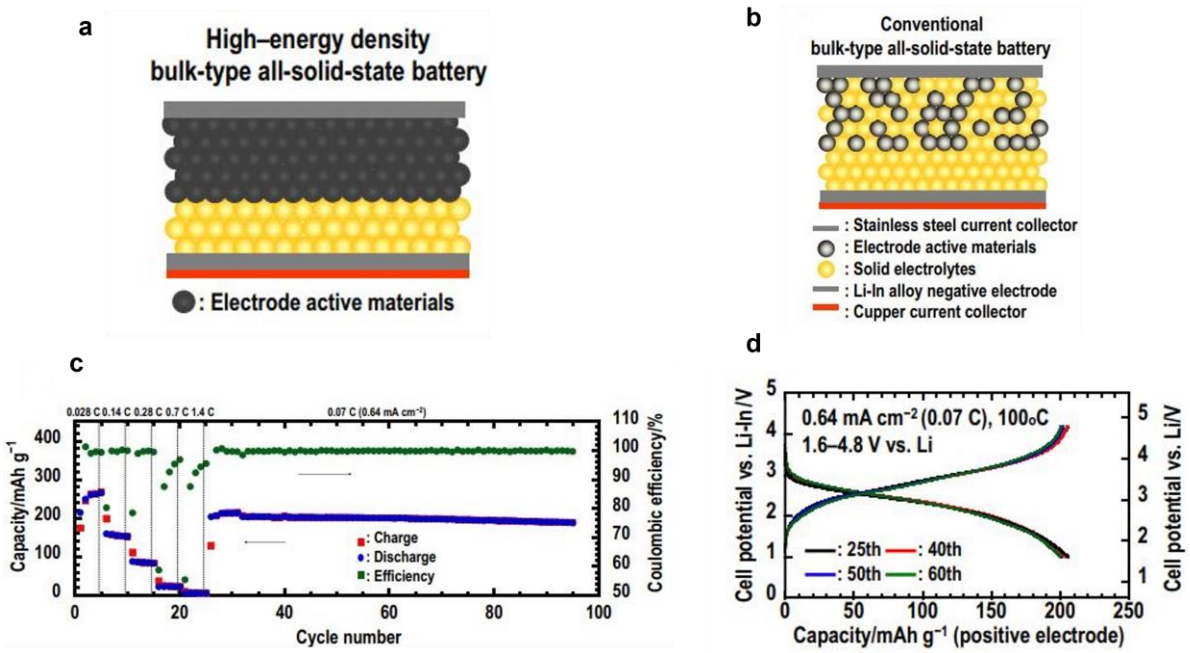

Figure 2.12: $Li_2Ru_{0.8}S_{0.2}O_{3.2}$ positive electrode. (a) Schematic for a diffusion-dependent electrode. (b) Schematic for a composite electrode. (c) Cycle performance of the diffusion-dependent electrode cell. (d) Charge/discharge curves of the diffusion-dependent electrode. Reproduced with permission from Science Advances [109].

In a different investigation, a diffusion-dependent solid-state TiS_2 electrode was developed by Y. Lee et al. and is seen schematically in **Figure 2.13a**. At a loading level of 45.6 mg.cm^{-2}, this electrode produces high areal and volumetric capacities of 9.43 mAh.cm^{-2} and 578 mAh.cm^{-3}, respectively (**Figures 2.13b and 2.13c**). This outstanding performance resulted from the TiS_2 morphological transformation from two-dimensional flakes to zero-dimensional nanograins, which led to superior mechanical ductility, high electronic conductivity, and stable Li-ion storage capabilities [119].

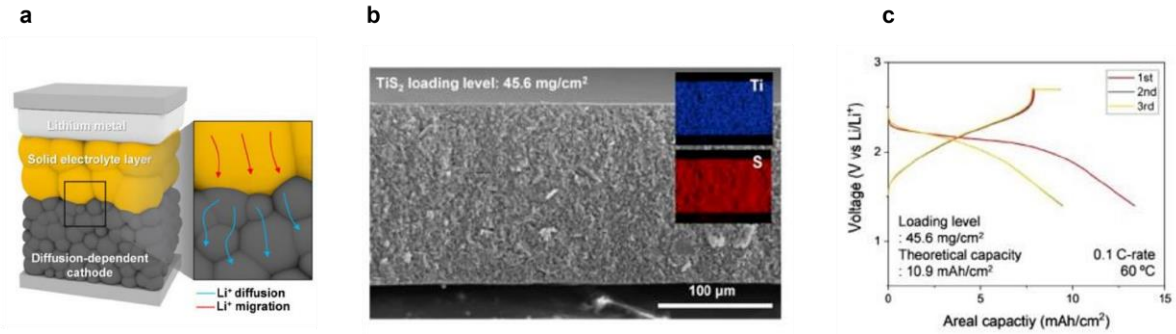

Figure 2.13: (a) Schematic representation of a lithium battery that uses a TiS_2 diffusion-dependent cathode. (b) A cross-sectional scanning electron microscopy (SEM) image of the ball-milled TiS_2 diffusion-dependent electrode with a loading level of 45.6 mg.cm^{-2}. (c) Charge-discharge voltage profile of the ball-milled TiS_2 diffusion-dependent electrode with loading levels of 45.6 mg.cm^{-2}. Reproduced with permission from Elsevier [119].

Diffusion-dependent solid-state anodes have also been created in addition to the cathode. For instance, S. Meng's team published a micro silicon diffusion-dependent electrode for ASSBs due to the material's high electronic conductivity (~ 3×10^{-5} S.cm^{-1}) and strong Li-ion diffusivity, which is schematically seen in **Figure 2.14**. A passivating SEI between the micro silicon and the SSE is created during lithiation, and then micro silicon particles are lithiated close to the interface. The nearby Si particles subsequently undergo a reaction with the highly reactive Li-Si. The reaction creates a densified Li-Si layer as it spreads throughout the electrode. This micro silicon solid-state electrode displayed a 2 mAh.cm^{-2} high reversible capacity with a high capacity retention of 80% after 500 cycles [116].

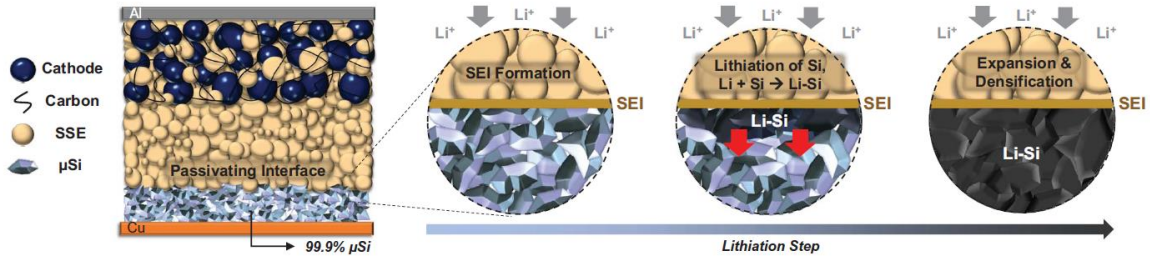

Figure 2.14: Schematic of 99.9 wt% micro silicon electrode in an ASSB full cell. Reproduced with permission from Science [116].

The diffusion-dependent solid-state anode material received tremendous attention from Y. Lee's team. His group's initial proposal for a diffusion-dependent graphite electrode employing a traditional slurry casting technique was made in 2020. According to their work, an areal capacity of 2 ~ 6 mAh.cm^{-2} can be achieved at a high temperature in a high-loading graphite electrode by using Li-ion self-diffusion inside graphite electrodes [118]. Following this study, they presented an electrode for ASSBs that was graphite-silicon diffusion-dependent and had a short effective diffusion length, schematically shown in **Figure 2.15a** [120]. Recent results using a hybrid solid-state electrode (**Figure 2.15b**) technique (composite electrode and diffusion electrode) showed high normalized capacities of 5.83 mAh.cm^{-2} and 1300 mAh.cm^{-3}, which are among the highest values reported so far for ASSBs [123].

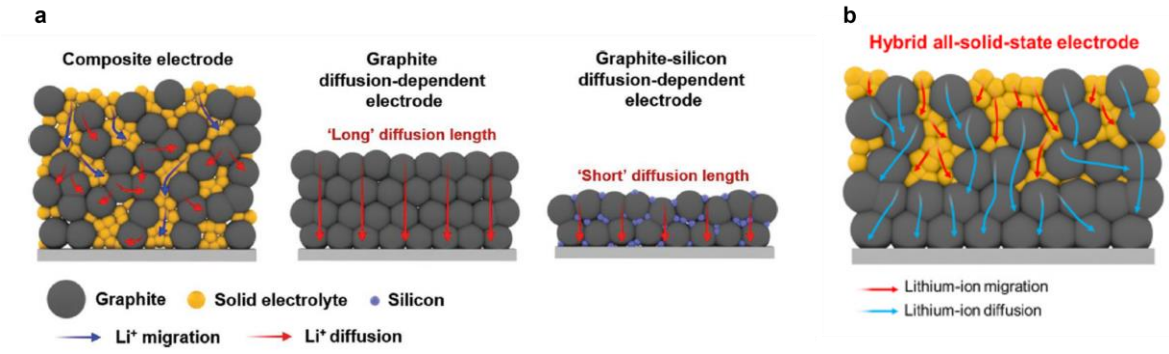

Figure 2.15: (a) Diagram illustrating the structure and lithium-ion transport of the composite electrode, the graphite diffusion-dependent electrode, and the graphite-silicon diffusion-dependent electrode. Reproduced with permission from Wiley [120].

(b) Schematic illustration of Li-ion transport mechanism in a composite-diffusion hybrid electrode. Reproduced with permission from Elsevier [123].

In summary, various SSEs, including sulfide, oxide, and halide electrolytes, have been developed to fabricate ASSBs. Due to the inferior solid-solid contact and significant interface reactions, SSEs face several interfacial challenges at the cathode and anode interfaces, hindering Li^+ transport at the electrode/electrolyte contact. At the cathode interface, space charge layer formation, interfacial reactions, and interfacial ionic contact are three main challenges. At the anode interface, the high interfacial resistance and lithium dendrite formation are two major challenges facing the lithium anode and SSE contact. The reason for the high interfacial resistance is that when SSEs encountered a lithium metal anode, they experienced thermodynamic reduction to produce new phases. Also, as mentioned, there are two types of solid-state electrode designs used in ASSBs: a) composite electrode with a well-mixed active material and solid electrolyte, b) diffusion-dependent electrode, which is mainly made of active material and utilizes interparticle lithium-ion diffusion between active material particles. As already stated, diffusion-dependent electrode design has gained much attention recently due to its ease of fabrication and ability to avoid the severe problems caused by solid electrolytes with high chemical reactivity with polar solvents and high interface resistance with neighboring particles. Additionally, the compact electrode design of the diffusion-dependent electrode, which does not use a solid electrolyte, allows it to provide a greater energy density than the composite electrode. The research in the thesis focuses on the Gr/P and HC diffusion-dependent electrodes for sulfide-Based ASSLIBs.

2.3 References

[1] A. Manthiram, “A reflection on lithium-ion battery cathode chemistry,” *Nat. Commun.*, vol. 11, no. 1, pp. 1–9, 2020.

[2] M. Li, J. Lu, Z. Chen, and K. Amine, “30 Years of Lithium-Ion Batteries,” *Adv. Mater.*, vol. 30, no. 33, 2018, doi: 10.1002/adma.201800561.

[3] M. Winter, B. Barnett, and K. Xu, “Before Li Ion Batteries,” *Chem. Rev.*, vol. 118, no. 23, pp. 11433–11456, Dec. 2018, doi: 10.1021/acs.chemrev.8b00422.

[4] M. Armand and J. M. Tarascon, “Issues and challenges facing rechargeable lithium batteries,” *Nature*, vol. 414, no. 6861, pp. 359–367, 2001.

[5] H. Takeshita, “Portable Li-ion, worldwide,” 2000.

[6] “IEA (2021), Global EV Outlook 2021, IEA, Paris,” 2021.

[7] J. Francfort and K. Walkowicz, “Electrochemical Energy Storage Technical Team Roadmap,” *U.S. Drive*, no. June, pp. 1–17, 2017.

[8] Y. Ding, Z. P. Cano, A. Yu, J. Lu, and Z. Chen, “Automotive Li-ion batteries: current status and future perspectives,” *Electrochem. Energy Rev.*, vol. 2, no. 1, pp. 1–28, 2019.

[9] T. B. Reddy, *Linden’s handbook of batteries*. McGraw-Hill Education, 2011.

[10] D. Li, D. Danilov, H. Bergveld, R.-A. Eichel, and P. Notten, “CHAPTER 9: Understanding battery aging mechanisms,” in *RSC Catalysis Series*, 2019, pp. 220–250.

[11] N. Nitta and G. Yushin, “High-capacity anode materials for lithium-ion batteries: choice of elements and structures for active particles,” *Part. Part. Syst. Charact.*, vol. 31, no. 3, pp. 317–336, 2014.

[12] B. Scrosati and J. Garche, “Lithium batteries: Status, prospects and future,” *J. Power Sources*, vol. 195, no. 9, pp. 2419–2430, 2010.

[13] M. Yang and J. Hou, “Membranes in lithium ion batteries,” *Membranes (Basel).*, vol. 2, no. 3, pp. 367–383, 2012.

[14] J. R. Szczech and S. Jin, “Nanostructured silicon for high capacity lithium battery anodes,” *Energy Environ. Sci.*, vol. 4, no. 1, pp. 56–72, 2011, doi: 10.1039/c0ee00281j.

[15] E. D. I. Michael and M. Thackeray, “Christopher Wolverton, Electrical energy storage for transportation-approaching the limits of, and going beyond, lithium-ion batteries,” *Energy Environ. Sci.*, vol. 5, pp. 7854–7863, 2012.

[16] H. Wu and Y. Cui, “Designing nanostructured Si anodes for high energy lithium ion batteries,” *Nano Today*, vol. 7, no. 5, pp. 414–429, 2012.

[17] X. Huang, “Separator technologies for lithium-ion batteries,” *J. Solid State Electrochem.*, vol. 15, no. 4, pp. 649–662, 2011.

[18] P. Zhu, D. Gastol, J. Marshall, R. Sommerville, V. Goodship, and E. Kendrick, “A review of current collectors for lithium-ion batteries,” *J. Power Sources*, vol. 485, p. 229321, 2021.

[19] J.-K. Park, *Principles and applications of lithium secondary batteries*. John Wiley & Sons, 2012.

[20] Z. H. Z. H. Khan, “Zou W. Xu J. Zhang L. et al,” *J. Mater. Chem. A*, vol. 6, no. 42, pp. 20564–20620, 2018.

[21] W. Chen, “A review of materials and their future development trends for lithium ion battery anodes,” in *IOP Conference Series: Earth and Environmental Science*, 2020, vol. 546, no. 2, p. 22026.

[22] M. Marcinek *et al.*, “Electrolytes for Li-ion transport–Review,” *Solid State Ionics*, vol. 276, pp. 107–126, 2015.

[23] Y.-K. Sun, “Promising all-solid-state batteries for future electric vehicles,” *ACS Energy Letters*, vol. 5, no. 10. ACS Publications, pp. 3221–3223, 2020.

[24] S. S. Zhang, “A review on electrolyte additives for lithium-ion batteries,” *J. Power Sources*, vol. 162, no. 2 SPEC. ISS., pp. 1379–1394, 2006, doi: 10.1016/j.jpowsour.2006.07.074.

[25] A. Manthiram, “An outlook on lithium ion battery technology,” *ACS Cent. Sci.*, vol. 3, no. 10, pp. 1063–1069, 2017.

[26] W. Li, E. M. Erickson, and A. Manthiram, “High-nickel layered oxide cathodes for lithium-based automotive batteries,” *Nat. Energy*, vol. 5, no. 1, pp. 26–34, 2020.

[27] A. Kwade, W. Haselrieder, R. Leithoff, A. Modlinger, F. Dietrich, and K. Droeder, “Current status and challenges for automotive battery production technologies. Nat Energy 3: 290–300.” 2018.

[28] J. W. Choi and D. Aurbach, “Promise and reality of post-lithium-ion batteries with high energy densities,” *Nat. Rev. Mater.*, vol. 1, no. 4, p. 16013, 2016, doi: 10.1038/natrevmats.2016.13.

[29] A. Manthiram, X. Yu, and S. Wang, “Lithium battery chemistries enabled by solid-state electrolytes,” *Nat. Rev. Mater.*, vol. 2, no. 4, p. 16103, 2017, doi: 10.1038/natrevmats.2016.103.

[30] X. Chen, W. He, L.-X. Ding, S. Wang, and H. Wang, “Enhancing interfacial contact in all solid state batteries with a cathode-supported solid electrolyte membrane framework,” Energy Environ. Sci., vol. 12, no. 3, pp. 938–944, 2019, doi: 10.1039/c8ee02617c.

[31] Y. Kato *et al.*, “High-power all-solid-state batteries using sulfide superionic conductors,” *Nat. Energy*, vol. 1, no. 4, p. 16030, 2016, doi: 10.1038/nenergy.2016.30.

[32] Y. Wang *et al.*, “Design principles for solid-state lithium superionic conductors,” *Nat. Mater.*, vol. 14, no. 10, pp. 1026–1031, 2015, doi: 10.1038/nmat4369.

[33] J. Wan, J. Xie, D. G. Mackanic, W. Burke, Z. Bao, and Y. Cui, “Status, promises, and challenges of nanocomposite solid-state electrolytes for safe and high performance

lithium batteries," *Mater. Today Nano*, vol. 4, pp. 1–16, 2018, doi: https://doi.org/10.1016/j.mtnano.2018.12.003.

[34] S. Xia, X. Wu, Z. Zhang, Y. Cui, and W. Liu, "Practical Challenges and Future Perspectives of All-Solid-State Lithium-Metal Batteries," *Chem*, vol. 5, no. 4, pp. 753–785, 2019, doi: 10.1016/j.chempr.2018.11.013.

[35] Y.-S. Hu and Y. Lu, "2019 Nobel Prize for the Li-Ion Batteries and New Opportunities and Challenges in Na-Ion Batteries," *ACS Energy Lett.*, vol. 4, no. 11, pp. 2689–2690, Nov. 2019, doi: 10.1021/acsenergylett.9b02190.

[36] Q. Zhao, S. Stalin, C.-Z. Zhao, and L. A. Archer, "Designing solid-state electrolytes for safe, energy-dense batteries," *Nat. Rev. Mater.*, vol. 5, no. 3, pp. 229–252, 2020, doi: 10.1038/s41578-019-0165-5.

[37] H.-D. Lim *et al.*, "A review of challenges and issues concerning interfaces for all-solid-state batteries," *Energy Storage Mater.*, vol. 25, pp. 224–250, 2020, doi: https://doi.org/10.1016/j.ensm.2019.10.011.

[38] C. Sun, J. Liu, Y. Gong, D. P. Wilkinson, and J. Zhang, "Recent advances in all-solid-state rechargeable lithium batteries," *Nano Energy*, vol. 33, pp. 363–386, 2017.

[39] E. Quartarone and P. Mustarelli, "Electrolytes for solid-state lithium rechargeable batteries: recent advances and perspectives," *Chem. Soc. Rev.*, vol. 40, no. 5, pp. 2525–2540, 2011.

[40] Y.-S. Hu, "Batteries: getting solid," *Nat. Energy*, vol. 1, no. 4, pp. 1–2, 2016.

[41] J. W. Fergus, "Ceramic and polymeric solid electrolytes for lithium-ion batteries," *J. Power Sources*, vol. 195, no. 15, pp. 4554–4569, 2010.

[42] W. Xia *et al.*, "Ionic conductivity and air stability of Al-doped $Li_7La_3Zr_2O_{12}$ sintered in alumina and Pt crucibles," *ACS Appl. Mater. Interfaces*, vol. 8, no. 8, pp. 5335–5342, 2016.

[43] T. Matsuyama, A. Sakuda, A. Hayashi, Y. Togawa, S. Mori, and M. Tatsumisago, “Electrochemical properties of all-solid-state lithium batteries with amorphous titanium sulfide electrodes prepared by mechanical milling,” *J. Solid State Electrochem.*, vol. 17, no. 10, pp. 2697–2701, 2013.

[44] T. K. Schwietert *et al.*, “Clarifying the relationship between redox activity and electrochemical stability in solid electrolytes,” *Nat. Mater.*, vol. 19, no. 4, pp. 428–435, 2020.

[45] D. Wang, C. Zhu, Y. Fu, X. Sun, and Y. Yang, “Interfaces in garnet-based all-solid-state lithium batteries,” *Adv. Energy Mater.*, vol. 10, no. 39, p. 2001318, 2020.

[46] Y. Xiao *et al.*, “Electrolyte melt infiltration for scalable manufacturing of inorganic all-solid-state lithium-ion batteries,” *Nat. Mater.*, vol. 20, no. 7, pp. 984–990, 2021.

[47] N. Kamaya *et al.*, “A lithium superionic conductor,” *Nat. Mater.*, vol. 10, no. 9, pp. 682–686, 2011, doi: 10.1038/nmat3066.

[48] L. Zhou, C. Y. Kwok, A. Shyamsunder, Q. Zhang, X. Wu, and L. F. Nazar, “A new halospinel superionic conductor for high-voltage all solid state lithium batteries,” *Energy Environ. Sci.*, vol. 13, no. 7, pp. 2056–2063, 2020.

[49] A. Miura *et al.*, “Liquid-phase syntheses of sulfide electrolytes for all-solid-state lithium battery,” *Nat. Rev. Chem.*, vol. 3, no. 3, pp. 189–198, 2019, doi: 10.1038/s41570-019-0078-2.

[50] F. Mizuno, A. Hayashi, K. Tadanaga, and M. Tatsumisago, “New, highly ion-conductive crystals precipitated from Li_2S-P_2S_5 glasses,” *Adv. Mater.*, vol. 17, no. 7, pp. 918–921, 2005, doi: 10.1002/adma.200401286.

[51] K. H. Park *et al.*, “Design Strategies, Practical Considerations, and New Solution Processes of Sulfide Solid Electrolytes for All-Solid-State Batteries,” *Adv. Energy Mater.*, vol. 8, no. 18, 2018, doi: 10.1002/aenm.201800035.

[52] S. Ohta, J. Seki, Y. Yagi, Y. Kihira, T. Tani, and T. Asaoka, “Co-sinterable lithium garnet-type oxide electrolyte with cathode for all-solid-state lithium ion battery,” *J. Power Sources*, vol. 265, pp. 40–44, 2014, doi: https://doi.org/10.1016/j.jpowsour.2014.04.065.

[53] X. Han *et al.*, “Negating interfacial impedance in garnet-based solid-state Li metal batteries,” *Nat. Mater.*, vol. 16, no. 5, pp. 572–579, 2017, doi: 10.1038/nmat4821.

[54] S. Xu *et al.*, “Three-Dimensional, Solid-State Mixed Electron–Ion Conductive Framework for Lithium Metal Anode,” *Nano Lett.*, vol. 18, no. 6, pp. 3926–3933, Jun. 2018, doi: 10.1021/acs.nanolett.8b01295.

[55] K. Xu, “Nonaqueous liquid electrolytes for lithium-based rechargeable batteries,” *Chem. Rev.*, vol. 104, no. 10, pp. 4303–4418, 2004.

[56] Y. Sun, K. Suzuki, S. Hori, M. Hirayama, and R. Kanno, “Superionic Conductors: $Li_{10+\delta}[Sn_ySi_{1-y}]_{1+\delta}P_{2-\delta}S_{12}$ with a $Li_{10}GeP_2S_{12}$-Type Structure in the Li_3PS_4-Li_4SnS_4-Li_4SiS_4 Quasi-Ternary System,” *Chem. Mater*, vol. 29, pp. 5858–5864, 2017.

[57] V. Thangadurai, S. Narayanan, and D. Pinzaru, “Garnet-type solid-state fast Li ion conductors for Li batteries: Critical review,” *Chem. Soc. Rev.*, vol. 43, no. 13, pp. 4714–4727, 2014, doi: 10.1039/c4cs00020j.

[58] R. Chen, W. Qu, X. Guo, L. Li, and F. Wu, “The pursuit of solid-state electrolytes for lithium batteries: from comprehensive insight to emerging horizons,” *Mater. Horizons*, vol. 3, no. 6, pp. 487–516, 2016.

[59] R. Kanno and M. Murayama, “Lithium ionic conductor thio-LISICON: the Li_2S-GeS_2-P_2S_5 system,” *J. Electrochem. Soc.*, vol. 148, no. 7, p. A742, 2001.

[60] H. Deiseroth *et al.*, “Li_6PS_5X: a class of crystalline Li-rich solids with an unusually high Li^+ mobility,” *Angew. Chemie Int. Ed.*, vol. 47, no. 4, pp. 755–758, 2008.

[61] S. Kong *et al.*, “Lithium argyrodites with phosphorus and arsenic: order and disorder of lithium atoms, crystal chemistry, and phase transitions,” *Chem. Eur. J.*, vol.

16, no. 7, pp. 2198–2206, 2010.

[62] S. T. Kong, Ö. Gün, B. Koch, H. J. Deiseroth, H. Eckert, and C. Reiner, "Structural Characterisation of the Li Argyrodites Li_7PS_6 and Li_7PSe_6 and their Solid Solutions: Quantification of Site Preferences by MAS-NMR Spectroscopy," *Chem. Eur. J.*, vol. 16, no. 17, pp. 5138–5147, 2010.

[63] O. Pecher *et al.*, "Atomistic Characterisation of Li^+ Mobility and Conductivity in $Li_{7-x}PS_{6-x}I_x$ Argyrodites from Molecular Dynamics Simulations, Solid-State NMR, and Impedance Spectroscopy," *Chem. Eur. J.*, vol. 16, no. 28, pp. 8347–8354, 2010.

[64] H. M. Chen, C. Maohua, and S. Adams, "Stability and ionic mobility in argyrodite-related lithium-ion solid electrolytes," *Phys. Chem. Chem. Phys.*, vol. 17, no. 25, pp. 16494–16506, 2015.

[65] H. Deiseroth, J. Maier, K. Weichert, V. Nickel, S. Kong, and C. Reiner, "Li_7PS_6 and Li_6PS_5X (X: Cl, Br, I): Possible Three-dimensional Diffusion Pathways for Lithium Ions and Temperature Dependence of the Ionic Conductivity by Impedance Measurements." Wiley Online Library, 2011.

[66] S. Boulineau, M. Courty, J.-M. Tarascon, and V. Viallet, "Mechanochemical synthesis of Li-argyrodite Li_6PS_5X (X= Cl, Br, I) as sulfur-based solid electrolytes for all solid state batteries application," *Solid State Ionics*, vol. 221, pp. 1–5, 2012.

[67] F. Stadler and C. Fietzek, "Crystalline halide substituted Li-argyrodites as solid electrolytes for lithium secondary batteries," *ECS Trans.*, vol. 25, no. 36, p. 177, 2010.

[68] N. J. J. De Klerk, I. Rosłoń, and M. Wagemaker, "Diffusion mechanism of Li argyrodite solid electrolytes for Li-ion batteries and prediction of optimized halogen doping: the effect of Li vacancies, halogens, and halogen disorder," *Chem. Mater.*, vol. 28, no. 21, pp. 7955–7963, 2016.

[69] M. Tatsumisago and A. Hayashi, "Sulfide glass-ceramic electrolytes for all-solid-state lithium and sodium batteries," *Int. J. Appl. Glas. Sci.*, vol. 5, no. 3, pp. 226–235,

2014.

[70] A. R. Kulkarni, H. S. Maiti, and A. Paul, “Fast ion conducting lithium glasses-Review,” *Bull. Mater. Sci.*, vol. 6, no. 2, pp. 201–221, 1984, doi: 10.1007/BF02743897.

[71] F. Mizuno, A. Hayashi, K. Tadanaga, and M. Tatsumisago, “New, highly ion-conductive crystals precipitated from Li_2S–P_2S_5 glasses,” *Adv. Mater.*, vol. 17, no. 7, pp. 918–921, 2005.

[72] M. Tatsumisago and A. Hayashi, “Superionic glasses and glass–ceramics in the Li_2S–P_2S_5 system for all-solid-state lithium secondary batteries,” *Solid State Ionics*, vol. 225, pp. 342–345, 2012.

[73] N. Machida, H. Maeda, H. Peng, and T. Shigematsu, “All-Solid-State Lithium Battery with $LiCo_{0.3}Ni_{0.7}O_2$ Fine Powder as Cathode Materials with an Amorphous Sulfide Electrolyte,” *J. Electrochem. Soc.*, vol. 149, no. 6, p. A688, 2002.

[74] A. Hayashi, “Preparation and characterization of glassy materials for all-solid-state lithium secondary batteries,” *J. Ceram. Soc. Japan*, vol. 115, no. 1338, pp. 110–117, 2007.

[75] K. Minami, A. Hayashi, and M. Tatsumisago, “Preparation and characterization of superionic conducting $Li_7P_3S_{11}$ crystal from glassy liquids,” *J. Ceram. Soc. Japan*, vol. 118, no. 1376, pp. 305–308, 2010.

[76] M. Tatsumisago, T. Saito, and T. Minami, “Fabrication of mesoscopic composites composed of α-AgI and AgI-based superionic glass,” *Thermochim. Acta*, vol. 280, pp. 333–341, 1996.

[77] M. Tatsumisago, T. Saito, and T. Minami, “Stabilization of Superionic α-AgI at Room Temperature by Heating of $AgI-Ag_2O-MoO_3$ Glasses,” *Chem. Lett.*, vol. 30, no. 8, pp. 790–791, 2001.

[78] V. Thangadurai, H. Kaack, and W. J. F. Weppner, “Novel fast lithium ion conduction in garnet-type $Li_5La_3M_2O_{12}$ (M = Nb, Ta),” *J. Am. Ceram. Soc.*, vol. 86, no.

3, pp. 437–440, 2003, doi: 10.1111/j.1151-2916.2003.tb03318.x.

[79] R. Murugan, V. Thangadurai, and W. Weppner, “Fast lithium ion conduction in garnet-type $Li_7La_3Zr_2O_{12}$,” *Angew. Chemie - Int. Ed.*, vol. 46, no. 41, pp. 7778–7781, 2007, doi: 10.1002/anie.200701144.

[80] J. Awaka, A. Takashima, K. Kataoka, N. Kijima, Y. Idemoto, and J. Akimoto, “Crystal structure of fast lithium-ion-conducting cubic $Li_7La_3Zr_2O_{12}$,” *Chem. Lett.*, vol. 40, no. 1, pp. 60–62, 2011, doi: 10.1246/cl.2011.60.

[81] Y. Li *et al.*, “Hybrid Polymer/Garnet Electrolyte with a Small Interfacial Resistance for Lithium-Ion Batteries,” *Angew. Chemie - Int. Ed.*, vol. 56, no. 3, pp. 753–756, 2017, doi: 10.1002/anie.201608924.

[82] I. Abrahams and E. Hadzifejzovic, “Lithium ion conductivity and thermal behaviour of glasses and crystallised glasses in the system Li_2O–Al_2O_3–TiO_2–P_2O_5,” *Solid State Ionics*, vol. 134, no. 3, pp. 249–257, 2000, doi: https://doi.org/10.1016/S0167-2738(00)00768-2.

[83] Y. Inaguma *et al.*, “High ionic conductivity in lithium lanthanum titanate,” *Solid State Commun.*, vol. 86, no. 10, pp. 689–693, 1993, doi: https://doi.org/10.1016/0038-1098(93)90841-A.

[84] S. Stramare, V. Thangadurai, and W. Weppner, “Lithium lanthanum titanates: a review,” *Chem. Mater.*, vol. 15, no. 21, pp. 3974–3990, 2003.

[85] X. Li *et al.*, “Progress and Perspectives for Halide Solid-State Electrolyte for All-Solid-State Lithium Batteries,” *Energy*, vol. 11, no. 4, pp. 719–1000, 2018.

[86] T. Asano, A. Sakai, S. Ouchi, M. Sakaida, A. Miyazaki, and S. Hasegawa, “Solid halide electrolytes with high lithium-ion conductivity for application in 4 V class bulk-type all-solid-state batteries,” *Adv. Mater.*, vol. 30, no. 44, p. 1803075, 2018.

[87] S. Wang *et al.*, “Lithium chlorides and bromides as promising solid-state chemistries for fast ion conductors with good electrochemical stability,” *Angew. Chemie*

Int. Ed., vol. 58, no. 24, pp. 8039–8043, 2019.

[88] Y. Zhao and L. L. Daemen, "Superionic Conductivity in Lithium-Rich Anti-Perovskites," *J. Am. Chem. Soc.*, vol. 134, no. 36, pp. 15042–15047, Sep. 2012, doi: 10.1021/ja305709z.

[89] K. Takada, "Progress and prospective of solid-state lithium batteries," *Acta Mater.*, vol. 61, no. 3, pp. 759–770, 2013.

[90] J. Vetter *et al.*, "Ageing mechanisms in lithium-ion batteries," *J. Power Sources*, vol. 147, no. 1–2, pp. 269–281, 2005.

[91] C. Xu, B. Sun, T. Gustafsson, K. Edström, D. Brandell, and M. Hahlin, "Interface layer formation in solid polymer electrolyte lithium batteries: an XPS study," *J. Mater. Chem. A*, vol. 2, no. 20, pp. 7256–7264, 2014.

[92] D. Fauteux, "Formation of a passivating film at the lithium-PEO-$LiCF_3SO_3$ interface," *Solid State Ionics*, vol. 17, no. 2, pp. 133–138, 1985.

[93] D. Fauteux, "Lithium Electrode/PEO-Based Polymer Electrolyte Interface Behavior Between 60° and 120° C," *J. Electrochem. Soc.*, vol. 135, no. 9, p. 2231, 1988.

[94] H. Y. Sun, Y. Takeda, N. Imanishi, O. Yamamoto, and H. Sohn, "Ferroelectric materials as a ceramic filler in solid composite polyethylene oxide-based electrolytes," *J. Electrochem. Soc.*, vol. 147, no. 7, p. 2462, 2000.

[95] K. Kerman, A. Luntz, V. Viswanathan, Y.-M. Chiang, and Z. Chen, "Review — Practical challenges hindering the development of solid state Li ion batteries," *J. Electrochem. Soc.*, vol. 164, no. 7, pp. A1731–A1744, 2017, doi: 10.1149/2.1571707jes.

[96] N. Nitta, F. Wu, J. T. Lee, and G. Yushin, "Li-ion battery materials: present and future," *Mater. today*, vol. 18, no. 5, pp. 252–264, 2015.

[97] S. Goriparti, E. Miele, F. De Angelis, E. Di Fabrizio, R. P. Zaccaria, and C. Capiglia, "Review on recent progress of nanostructured anode materials for Li-ion

batteries," *J. Power Sources*, vol. 257, pp. 421–443, 2014.

[98] L. Wang, B. Chen, J. Ma, G. Cui, and L. Chen, "Reviving lithium cobalt oxide-based lithium secondary batteries-toward a higher energy density," *Chem. Soc. Rev.*, vol. 47, no. 17, pp. 6505–6602, 2018.

[99] T. Shi *et al.*, "High Active Material Loading in All-Solid-State Battery Electrode via Particle Size Optimization," *Adv. Energy Mater.*, vol. 10, no. 1, 2020, doi: 10.1002/aenm.201902881.

[100] D. H. Kim *et al.*, "Infiltration of Solution-Processable Solid Electrolytes into Conventional Li-Ion-Battery Electrodes for All-Solid-State Li-Ion Batteries," *Nano Lett.*, vol. 17, no. 5, pp. 3013–3020, May 2017, doi: 10.1021/acs.nanolett.7b00330.

[101] L. Yang *et al.*, "Flexible Composite Solid Electrolyte Facilitating Highly Stable 'Soft Contacting' Li–Electrolyte Interface for Solid State Lithium-Ion Batteries," *Adv. Energy Mater.*, vol. 7, no. 22, 2017, doi: 10.1002/aenm.201701437.

[102] Z. Jiang *et al.*, "Tape-Casting $Li_{0.34}La_{0.56}TiO_3$ Ceramic Electrolyte Films Permit High Energy Density of Lithium-Metal Batteries," *Adv. Mater.*, vol. 32, no. 6, 2020, doi: 10.1002/adma.201906221.

[103] E. J. Cheng, T. Kimura, M. Shoji, H. Ueda, H. Munakata, and K. Kanamura, "Ceramic-Based Flexible Sheet Electrolyte for Li Batteries," *ACS Appl. Mater. Interfaces*, vol. 12, no. 9, pp. 10382–10388, Mar. 2020, doi: 10.1021/acsami.9b21251.

[104] F. Strauss *et al.*, "Impact of Cathode Material Particle Size on the Capacity of Bulk-Type All-Solid-State Batteries," *ACS Energy Lett.*, vol. 3, no. 4, pp. 992–996, Apr. 2018, doi: 10.1021/acsenergylett.8b00275.

[105] A. Bielefeld, D. A. Weber, and J. Janek, "Microstructural Modeling of Composite Cathodes for All-Solid-State Batteries," *J. Phys. Chem. C*, vol. 123, no. 3, pp. 1626–1634, Jan. 2019, doi: 10.1021/acs.jpcc.8b11043.

[106] X. Chen, W. He, L.-X. Ding, S. Wang, and H. Wang, "Enhancing interfacial

contact in all solid state batteries with a cathode-supported solid electrolyte membrane framework," *Energy Environ. Sci.*, vol. 12, no. 3, pp. 938–944, 2019, doi: 10.1039/c8ee02617c.

[107] Y. Li *et al.*, "Ultralow-Concentration Electrolyte for Na-Ion Batteries," *ACS Energy Lett.*, vol. 5, no. 4, pp. 1156–1158, Apr. 2020, doi: 10.1021/acsenergylett.0c00337.

[108] L. Zhou *et al.*, "High areal capacity, long cycle life 4 V ceramic all-solid-state Li-ion batteries enabled by chloride solid electrolytes," *Nat. Energy*, vol. 7, no. 1, pp. 83–93, 2022.

[109] K. Nagao *et al.*, "A reversible oxygen redox reaction in bulk-type all-solid-state batteries," *Sci. Adv.*, vol. 6, no. 25, p. eaax7236, 2020.

[110] J. Park *et al.*, "Dimension-controlled solid oxide electrolytes for all-solid-state electrodes: Percolation pathways, specific contact area, and effective ionic conductivity," *Chem. Eng. J.*, vol. 391, p. 123528, 2020.

[111] D. Y. Oh *et al.*, "Slurry-Fabricable Li^+-Conductive Polymeric Binders for Practical All-Solid-State Lithium-Ion Batteries Enabled by Solvate Ionic Liquids," *Adv. Energy Mater.*, vol. 9, no. 16, 2019, doi: 10.1002/aenm.201802927.

[112] K. Lee, J. Lee, S. Choi, K. Char, and J. W. Choi, "Thiol–ene click reaction for fine polarity tuning of polymeric binders in solution-processed all-solid-state batteries," *ACS Energy Lett.*, vol. 4, no. 1, pp. 94–101, 2018.

[113] G. Oh, M. Hirayama, O. Kwon, K. Suzuki, and R. Kanno, "Bulk-Type All Solid-State Batteries with 5 V Class $LiNi_{0.5}Mn_{1.5}O_4$ Cathode and $Li_{10}GeP_2S_{12}$ Solid Electrolyte," *Chem. Mater.*, vol. 28, no. 8, pp. 2634–2640, Apr. 2016, doi: 10.1021/acs.chemmater.5b04940.

[114] S. Cangaz *et al.*, "Enabling High-Energy Solid-State Batteries with Stable Anode Interphase by the Use of Columnar Silicon Anodes," *Adv. Energy Mater.*, vol. 10, no. 34,

p. 2001320, 2020.

[115] D.-M. Kim, S.-T. Yun, S. Yoon, and B. Mayer, “Signature of oxygen and sulfur isotopes of sulfate in ground and surface water reflecting enhanced sulfide oxidation in mine areas,” *Appl. Geochemistry*, vol. 100, pp. 143–151, 2019, doi: https://doi.org/10.1016/j.apgeochem.2018.11.018.

[116] D. H. S. Tan *et al.*, “Carbon-free high-loading silicon anodes enabled by sulfide solid electrolytes,” *Science (80-.).*, vol. 373, no. 6562, pp. 1494–1499, 2021.

[117] J. Y. Kim *et al.*, “Efficient cell design and fabrication of concentration-gradient composite electrodes for high-power and high-energy-density all-solid-state batteries,” *ETRI J.*, vol. 42, no. 1, pp. 129–137, 2020.

[118] J. Y. Kim *et al.*, “Diffusion-dependent graphite electrode for all-solid-state batteries with extremely high energy density,” *ACS Energy Lett.*, vol. 5, no. 9, pp. 2995–3004, 2020.

[119] J. Y. Kim *et al.*, “Revisiting TiS_2 as a diffusion-dependent cathode with promising energy density for all-solid-state lithium secondary batteries,” *Energy Storage Mater.*, vol. 41, pp. 289–296, 2021.

[120] J. Y. Kim *et al.*, “Graphite–Silicon Diffusion-Dependent Electrode with Short Effective Diffusion Length for High-Performance All-Solid-State Batteries,” *Adv. Energy Mater.*, vol. 12, no. 3, p. 2103108, 2022.

[121] J. Billaud, F. Bouville, T. Magrini, C. Villevieille, and A. R. Studart, “Magnetically aligned graphite electrodes for high-rate performance Li-ion batteries,” *Nat. Energy*, vol. 1, no. 8, pp. 1–6, 2016.

[122] U. Kasavajjula, C. Wang, and A. J. Appleby, “Nano-and bulk-silicon-based insertion anodes for lithium-ion secondary cells,” *J. Power Sources*, vol. 163, no. 2, pp. 1003–1039, 2007.

[123] J. Y. Kim *et al.*, “All-solid-state hybrid electrode configuration for high-

performance all-solid-state batteries: Comparative study with composite electrode and diffusion-dependent electrode," *J. Power Sources*, vol. 518, p. 230736, 2022.

3 Chapter 3: Experimental and Characterization Methods

This chapter discusses the experimental and characterization techniques utilized in the thesis.

3.1 Fabrication Methods

3.1.1 Fabrication of Electrodes

Each electrode slurry has three main components: anode/cathode active material, binder, and solvent. Graphite-phosphorus (Gr/P) and hard carbon (HC) were used as the active anode material and will be specified for each experimental chapter (chapters 4 and 5). Polyvinylidene fluoride (PVDF) was used as the binder. Super P C65 was utilized as the conductive additive for liquid cells. The active anode material: PVDF: Super P C65 were quickly weighed out with a VWR-225 AC scale in a ratio of 90:5:5 for liquid cells. For the all-solid-state cells, the active anode material and PVDF were quickly weighed out in a ratio of 98:2. The active material and binder were dry mixed with a mortar and pestle for 30 minutes to ensure even dispersion of the materials. The mixed materials were then dissolved into N-methyl-2-pyrrolidone (NMP) solvent (additional NMP adjusted a proper slurry viscosity). After that, materials were mixed in the mortar and pestle for 10 minutes to create uniform blending.

Once the slurry was thoroughly mixed, it was transferred onto a piece of copper (Cu) foil substrate and then casted onto the substrate at a thickness of 15 μm using an automatic coating machine. The slurry was then dried at 100°C under a vacuum overnight to eliminate solvent traces. Finally, roll-pressing was applied to the electrode to ensure structural stability and form a seamless interface between Gr/P and HC particles. After rolling, a circular punch is used to prepare 10 mm diameter (5 mm radius) disks from the finished electrode.

3.1.2 Coin Cell Assembly

In the glovebox, the CR2032 coin cells are put together in the following order: cathode shell, 10 mm diameter anode disk, 19 mm diameter Celgard 2400 separator with electrolyte, 14 mm lithium foil, spacer, spring, and anode shell. **Figure 3.1** shows the exploded view of the assembled coin cell. The electrolyte used is 1 M $LiPF_6$ dissolved in a 1:1:1 mixture of ethylene carbonate (EC), dimethyl carbonate (DMC), and ethyl methyl carbonate (EMC). Using plastic tweezers, the components of each cell are all precisely centred. After that, a hydraulic crimping machine is used to seal the constructed cell by applying pressure equals to 1000 PSI to it.

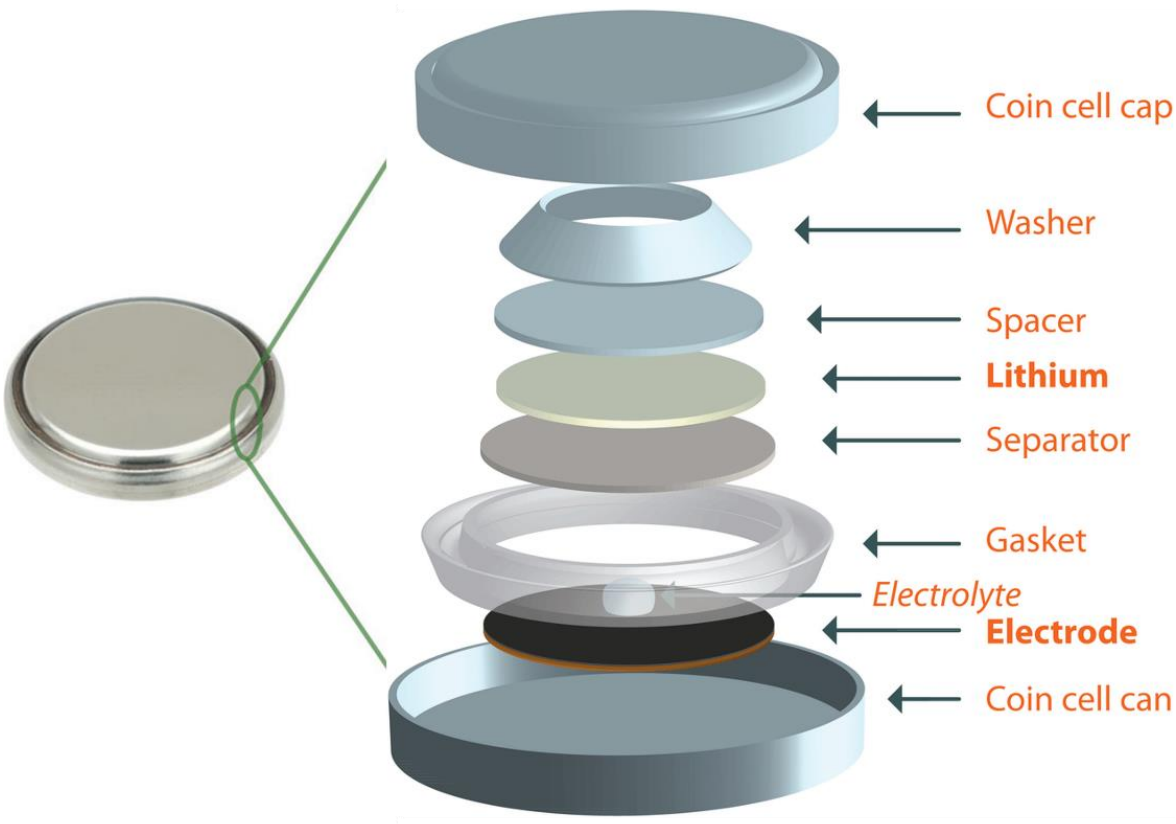

Figure 3.1: Coin cell components

3.1.3 Fabrication of All-Solid-State Batteries

The all-solid-state cells are assembled in the following order. First, 100 mg of Li_6PS_5Cl (LPSCl) powder was pelletized under 0.5 tons in a polyether ether ketone mold with a diameter of 13 mm to produce a solid electrolyte layer. The pre-pelletized solid electrolyte layer and the Gr/P and HC electrodes were combined by pressing under 4 tons once more after the Gr/P and HC electrodes had been compressed under 0.5 tons separately. The lithium metal half-cells were built in a glove box under a high-purity Ar-filled atmosphere ($H_2O \leq 0.1$ ppm, $O_2 \leq 0.1$ ppm) with Li-In alloy as the counter electrode and on the opposite side. The ASSLIB schematic with a diffusion-dependent electrode is illustrated in **Figure 3.2a**, and **Figure 3.2b** shows physical representations of the mold cells.

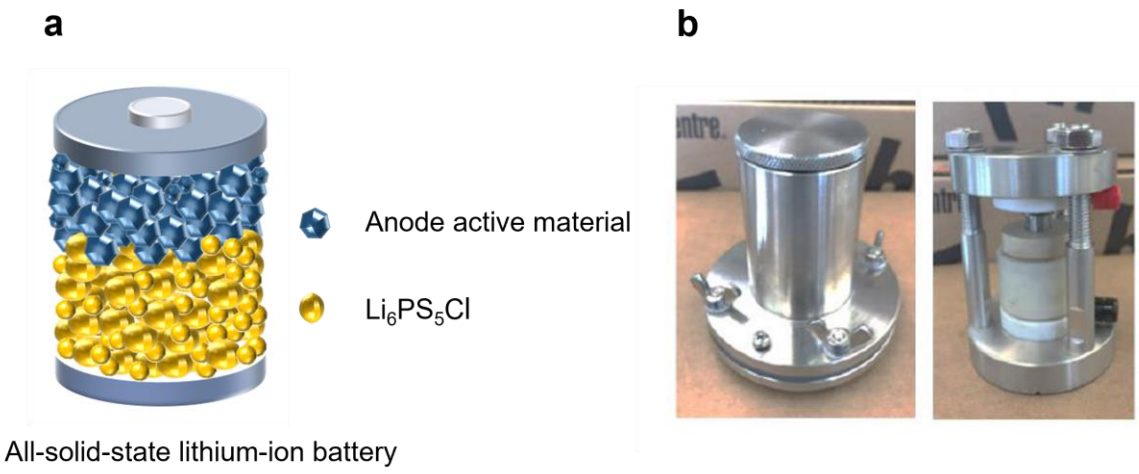

Figure 3.2: (a) Schematic of the ASSLIB with a diffusion-dependent electrode. (b) Physical pictures of the mold cells.

3.2 Characterization Methods

3.2.1 Galvanostatic Charge-Discharge

Galvanostatic charge-discharge (GCD) testing was used to examine the coin cells and all-solid-state cells' electrochemical performance. When conducting a GCD test, a continuous current is applied to the cell while measuring its capacity and voltage. The

coin cells were examined using a Neware BTS4000 battery testing machine (**Figure 3.3a**). All-solid-state cells' cycling tests were carried out using a Landt Instruments CT2001A battery testing system (**Figure 3.3b**), and high-temperature tests were carried out using a Land CT2001A battery testing system connected to a Fisher Scientific 60L Gravity Oven (151030519 model) (**Figure 3.3c**).

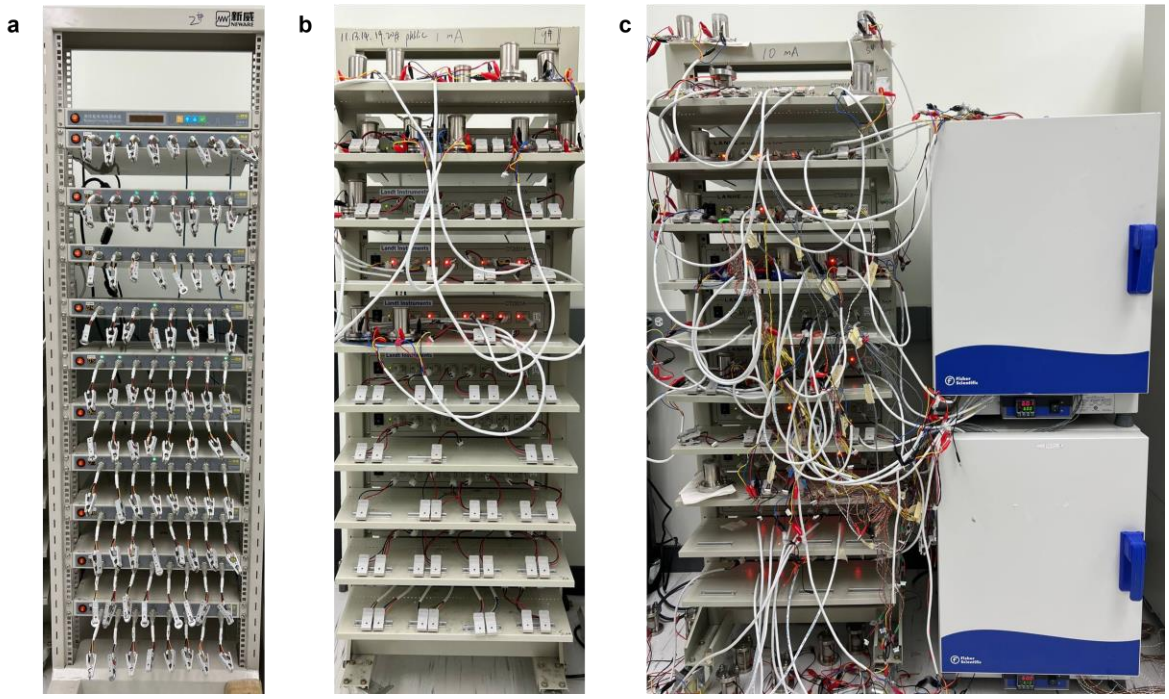

Figure 3.3: Photos of (a) Neware BTS4000 battery testing system, (b) Landt Instruments CT2001A battery testing system, (c) Land CT2001A battery testing system attached to a Fisher Scientific 60L Gravity Oven.

GCD experiments for the liquid cells were carried out at room temperature (25 °C) with constant current (CC) discharging and CC charging, between 0 and 2 V. The cells were cycled at C/10 rate for the first 5 cycles and C/3 rate for the remaining 100 cycles for the cycling performance testing. To perform the rate capability tests, the cells performed 5 cycles at the following rates: C/10, C/4, C/3, C/2, 1C, and 2C, followed by 5 cycles at the C/10 rate.

Due to the use of Li-In alloy as the anode component, GCD tests for ASSBs were carried out with CC discharging and CC charging between -0.6 and 1.4 V at both low

temperatures (25 °C) and high temperatures (60 °C). The cells were cycled 100 times at a rate of 0.1C to examine the cycling performance. For the rate ability testing, the cells went through 5 cycles the following rates: 0.1C, 0.2C, 0.3C, 0.5C, and 1C, followed by 5 cycles at 0.3C rate. Both low-pressure and high-pressure tests were performed on the cells.

To comprehend the electrochemical performance of the various samples, GCD data were used to create voltage plots against specific capacity (V vs. Q) and discharge capacity against number of cycles. These graphs contain data that can be used to determine capacity, CE, and capacity retention. To understand the potentials at which specific electrochemical reactions (such as intercalation/deintercalation) and/or phase transitions occur, differential capacity against voltage (dQ/dV versus V) curves were built. These curves illustrate the change in specific capacity concerning voltage. In the voltage-capacity curves, flat plateaus typically indicate a two-phase reaction with a constant chemical potential, whereas a sloped plateau (i.e., a changing chemical potential) denotes a change in the concentration of the solid solution [1]. A steep rise or decline in the voltage of V versus Q curves marks the kinetic limit where the current being forced into or out of the electrode can no longer be absorbed. These plateaus are simple to recognize since they appear as peaks in the dQ/dV vs V curves [1].

3.2.2 Scanning Electron Microscopy and Energy Dispersive X-ray Spectroscopy

A popular imaging technique known as scanning electron microscopy (SEM) can reveal information about the composition and morphology of surfaces. **Figure 3.4a** shows how an electron beam is condensed and focussed onto a sample in a scanning electron microscope using several electromagnetic lenses and coils. An electron gun produces the electron beam. The electrons from the incoming beam interact with the atoms in the sample to produce a region, called the interaction volume, where signals, such as electromagnetic radiation and electrons, are emitted. Secondary electrons and specific X-rays are signals frequently examined in the SEM. The creation of secondary electrons occurs when incoming electrons impart energy to electrons that were initially bonded to

sample atoms; these electrons are subsequently inelastically dispersed and detected by the secondary electron detector [2]. Additionally, incoming electrons could excite electrons in a sample atom to a higher orbital, which causes them to generate distinctive X-rays upon returning to their ground state. An X-ray semiconductor detector attached to the scanning electron microscope can be used for energy dispersive X-ray spectroscopy (EDX) analysis of these X-rays. By comparing reference characteristic peaks, the energy and intensity of the X-rays are sorted into a spectrum that can be used to understand the data [3]. Surface morphology was characterized using the secondary electron mode on a Hitachi S-4800 scanning electron microscope (**Figure 3.4b**), with an acceleration voltage of 5.0 kV and a working distance of 5 mm. The scanning electron microscope's X-ray detector attachment was used for the EDX study, with a working distance of 15 mm and an acceleration voltage of 20.0 kV [4].

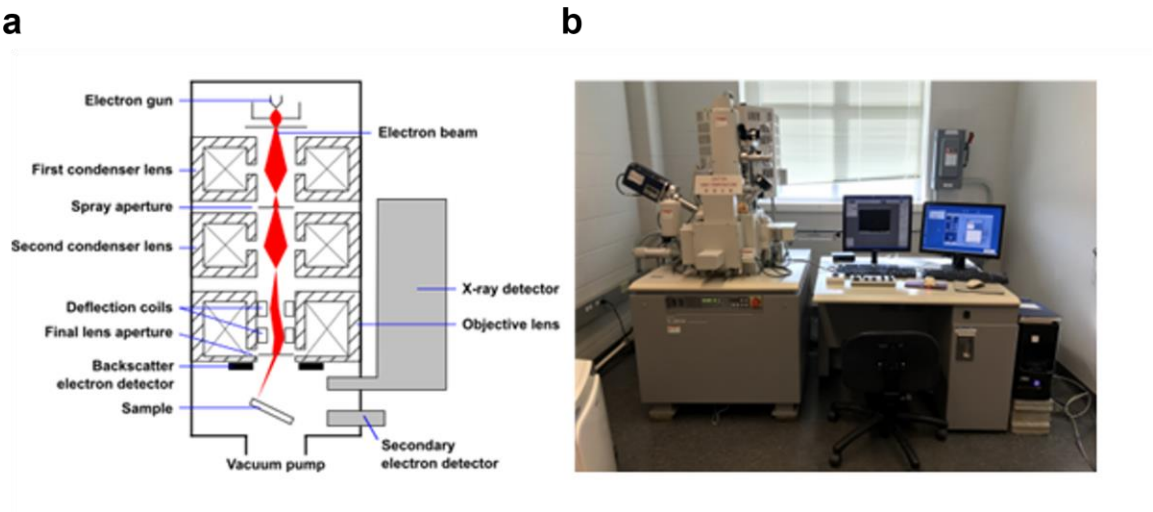

Figure 3.4: (a) Configuration of a typical SEM. Image licensed under CC BY-SA 3.0 [4]. (b) Photo of the Hitachi S-4800 scanning electron microscope.

3.2.3 X-ray Diffraction

XRD uses X-rays to identify a sample's structural information. The diffraction pattern at a certain angle, which is strongly related to the atomic arrangement of samples, can be seen if the XRD respects Bragg's law (**Figure 3.5a**). Cu Kα radiation at 40 kV and 40

mA was used to acquire the XRD pattern of the samples used in this thesis using a Bruker D8 Advance Diffractometer (**Figure 3.5b**).

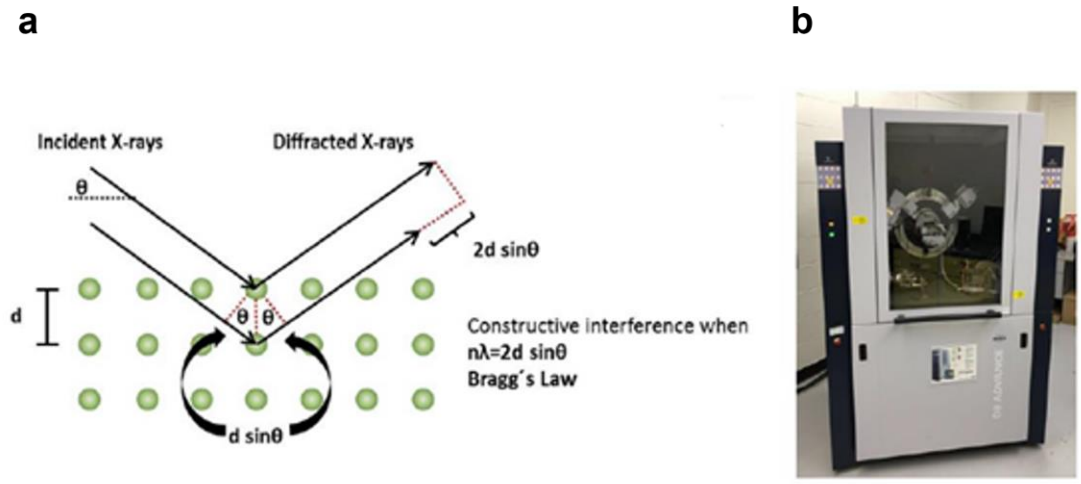

Figure 3.5: (a) The principle of XRD. (b) The Bruker D8 advance diffractometer XRD system.

3.3 References

[1] E. Talaie, P. Bonnick, X. Sun, Q. Pang, X. Liang, and L. F. Nazar, "Methods and protocols for electrochemical energy storage materials research," *Chem. Mater.*, vol. 29, no. 1, pp. 90–105, 2017.

[2] R. Mehta, "Interactions, Imaging and Spectra in SEM," 2012.

[3] D. Vaughan, *Energy Dispersive X-Ray Microanalysis An Introduction*. Kevex, 1983.

[4] Stef; ARTE, "Schema MEB," 2010. https://commons.wikimedia.org/wiki/File:Schema_MEB_(en).svg.

4 Chapter 4: Electrochemically Activated Graphite-Phosphorus Diffusion-Dependent Electrode for All-Solid-State Batteries

4.1 Introduction

All-solid-state batteries (ASSBs), which are composed entirely of solid-type components, are one of the most compelling next-generation energy storage technologies for achieving both superior safety and significant energy density [1]–[5]. The technology is expected to significantly contribute to the stable, long-term use of EVs and the balanced exploitation of renewable energy sources without any fire danger. Systematic research is essential for the development of SSEs with high (electro)chemical and favorable mechanical properties [6]–[10], profound comprehension of interface reactions between the solid compounds [11]–[20], and rational protocol of facile cell fabrication [21]–[25] in order to realize such an ideal using high-performance ASSBs. Due to ongoing research, several SSEs have demonstrated significant potential for high-performance ASSBs. For instance, the ionic conductivities of sulfide-based solid electrolytes like Li_6PS_5X (X: Br, Cl), $Li_{10}GeP_2S_{12}$, and $Li_{9.54}Si_{1.74}P_{1.44}S_{11.7}Cl_{0.3}$ reached the level of traditional liquid electrolytes [26]–[28]. The design of an all-solid-state electrode has also been enhanced, along with the inherent properties of materials, to optimize the potential of the active material while minimizing ionic resistance inside the electrode [23], [29]–[39]. Active material and solid electrolyte particles have typically been mixed uniformly to create composite electrodes, which resemble the porous electrode fully saturated with liquid electrolytes in LIBs. To create well-percolated ionic channels in this configuration, the morphological adjustment of solid electrolyte particles is vital [23], [33]. Additionally, composite electrodes exhibit many interfacial reactions due to the inherently small stability window of sulfide-based solid electrolytes. Furthermore, the energy density of ASSBs is compromised by the significant amount of inactive SSE in the composite electrodes.

In addition to the composite electrode, a new and effective electrode design that may deliver high energy density with an easy fabrication process is the diffusion-dependent electrode, which is mainly composed of active materials [30]–[32], [35], [36], [38]. The active material mechanically compliant with the applied pressure is preferable in this respect. Graphite and titanium disulfide are acceptable materials for diffusion-dependent electrode configuration [30], [36]. Additionally, Y. Lee's group proposed a graphite-silicon diffusion-dependent electrode for ASSBs. According to their research, an excellent electrode configuration for quick charge/discharge was created by using silicon between graphite particles [40]. A good anode choice for LIBs is elemental phosphorus because of its high volumetric and gravimetric energy density [41]–[45]. It is well known that phosphorus reacts electrochemically with lithium to create the Li_3P alloy. A high theoretical capacity of about 2595 $mAh.g^{-1}$ is produced by the three-electron transfer reaction between P and Li, roughly seven times that of graphite. However, phosphorus has two inherent constraints: (1) its low electrical conductivity (1×10^{-14} $S.cm^{-1}$) leads to poor reaction kinetics and complicated electrochemical redox processes, (2) upon lithiation, phosphorus experiences a volume change of more than 300 percent, which results in pulverization and an unstable SEI. As a result, anodes made of phosphorus exhibit quick capacity fading, poor CE, and electrode degradation during electrochemical cycling [46]–[48]. In order to get beyond these restrictions, various groups have created composites made of carbon and phosphorus [41], [49]–[53]. For instance, by cycling half-cells in a constrained voltage window of 0.78-2 V, Park et al. could attain a stable capacity of about 600 $mAh.g^{-1}$ for 100 charge-discharge cycles [49]. The stable discharge capacity was reported by Wang et al. to be around 2300 $mAh.g^{-1}$ for 55 cycles [50]. Marino et al. achieved a capacity of about 900 $mAh.g^{-1}$ after 20 cycles [41], while Sun et al. showed a very high initial discharge capacity of about 2786 $mAh.g^{-1}$ with a capacity retention of about 80% after 100 cycles [54]. However, despite recent improvements and outstanding performances, a composite of the graphite-phosphorus (Gr/P) has never been studied as a diffusion-dependent solid-state electrode for ASSBs.

Here, a high-performance diffusion-dependent electrode made of graphite and phosphorus is presented. Graphite, which can be used as the active material for diffusion-

dependent electrodes, suffers from its low volumetric capacity (~744 $mAh.cm^{-3}$ for 372 $mAh.g^{-1}$ and 2 $g.cm^{-3}$) [55]. The cell's performance, particularly at high C-rates, is typically unsatisfactory for overly thick graphite electrodes [36]. The composite anode of graphite and phosphorus can enhance the battery's capacity since its lithiation/delithiation potential is somewhat higher than that of pristine graphite. The higher lithiation potential of the composite Gr/P battery resulted in a lower working voltage, but capacity growth could make up for the energy loss. In this regard, the Gr/P composite anode will benefit in managing the battery's state of charge. It is discovered that interparticle diffusion between different active materials can easily take place, enabling stable operation of this electrode. Through comparing various graphite: phosphorus ratios, the all-solid-state electrode with 10 wt% of phosphorus to the total weight of active materials (graphite/phosphorus 90/10, wt%) showed an initial specific capacity of 638.2 $mAh.g^{-1}$, 38.4% capacity retention at 0.5 C-rate to that at 0.1 C-rate, and good capacity retention after cycling (92.7% after 40 cycles at 0.1 C-rate).

4.2 Methods

4.2.1 Fabrication of All-Solid-State Batteries

The Gr/P (different ratios of graphite: phosphorus is used) and PVDF were combined in NMP in a 98:2 weight ratio to create a slurry for diffusion-dependent electrodes. The resultant slurry was deposited on carbon-coated copper foil current collectors using the controlled doctor blade approach. The electrode was then dried for 24 hours at 100 °C in a vacuum oven to remove all solvent traces. Roll-pressing was applied to the diffusion-dependent electrode to ensure structural stability and create a seamless interface between Gr/P particles. Li_6PS_5Cl (LPSCl) powder of 100 mg was pelletized under 0.5 tons in a polyether ether ketone mold with a diameter of 13 mm to create a solid electrolyte layer. Separately, the Gr/P electrode was pressed under 0.5 tons, and then it was joined with the pre-pelletized LPSCl layer by pressing under 4 tons once more. The Li-In alloy was used as the counter electrode to create half-cells.

4.2.2 Electrochemical Measurement

GCD tests were performed at both room temperature (25 °C) and high temperature (60 °C) with CC discharging and CC charging, between -0.6 and 1.4 V (due to the presence of In in the anode part). The cells were cycled at 0.1 C-rate for 100 cycles for cycling performance testing. For the rate capability tests, the cells completed 5 cycles at the following rates: 0.1C, 0.2C, 0.3C, 0.5C, and 1C, followed by 5 cycles at 0.3 C-rate.

4.2.3 SEM and EDX

Surface morphology was characterized using a Hitachi S-4800 SEM in the secondary electron mode, with an acceleration voltage of 5.0 kV and a working distance of 5 mm. Also, the scanning electron microscope's X-ray detector attachment was used for the EDX study, with a working distance of 15 mm and an acceleration voltage of 20.0 kV.

4.2.4 XRD

Using Cu Kα radiation (λ = 1.54178 Å) and a particular container to prevent exposure to air during tests, X-ray powder diffraction was carried out using an X-ray diffraction diffractometer (XRD, Bruker AXS D8 Advance) to analyze the crystal structure of the samples between 2 theta between 10 ° and 80 °.

4.3 Results and Discussion

The common composite electrode and the all-solid-state graphite diffusion-dependent electrode are represented schematically in **Figures 4.1a** and **4.1b**. As can be seen in the figures, the diffusion-dependent electrode is composed chiefly of active material, in contrast to the composite electrode. For charge/discharge, this electrode utilizes interparticle lithium-ion diffusion between active material particles. As previously indicated, the low volumetric capacity of graphite hinders its application as a diffusion-dependent electrode. Additionally, the cell's performance, especially at high C-rates, is often unsatisfactory for excessively thick graphite electrodes. As a result, we proposed an electrode design consisting of a graphite matrix embedded with phosphorus particles,

schematically depicted in **Figure 4.1c**. In this configuration, the active graphite material contributes to the electrode's overall capacity while delivering enough electrons to the adjacent phosphorus, which has low electronic conductivity. Due to its structural stability, the graphite matrix can also operate as a buffer for phosphorus expansion and contraction during (de)lithiation, and graphite particles can transport lithium ions to the phosphorus particles. Low interface resistance should be used for the interdiffusion between the various active materials, graphite, and phosphorus. It is well known that phosphorus and lithium electrochemically react to form the Li_3P alloy, which functions as a Li-ion conductor and can considerably boost the electrode's capacity (**Figure 4.1d**). The diffusion-dependent electrode can deliver higher gravimetric and volumetric energy densities than the composite electrode (**Figures 4.1e** and **4.1f**) due to its compact electrode design without solid electrolyte particles.

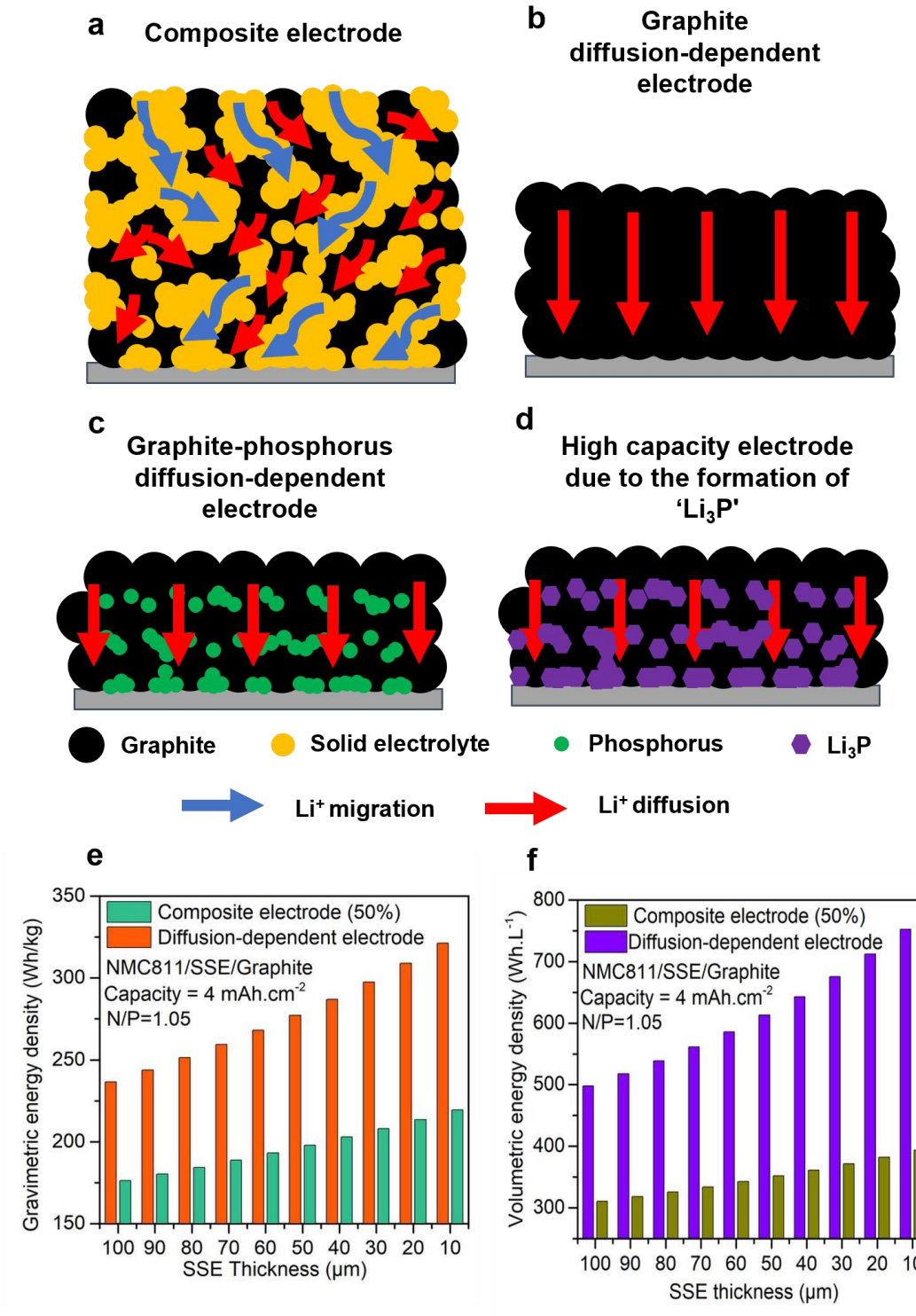

Figure 4.1: (a)-(b) Schematic comparison of the all-solid-state composite electrode and the diffusion-dependent electrode. (c) Schematic representation of the graphite-phosphorus diffusion-dependent electrode. (d) Formation of the Li_3P, Li-ion

conductor, between graphite particles. (e) Gravimetric energy density comparison of the composite electrode and diffusion-dependent electrode. (f) Volumetric energy density comparison of the composite electrode and diffusion-dependent electrode.

Figure 4.2 shows the scanning electron microscopy (SEM), energy dispersive X-ray spectroscopy (EDX) and X-ray diffraction (XRD) images of the pure graphite and graphite-phosphorus diffusion-dependent electrode with a weight ratio of 90/10. The graphite used in this thesis is the mesophase carbon microspheres (MG11) which have uniform sizes, as confirmed by SEM images. The typical spherical morphology with a uniform size is shown in the SEM images of the graphite (**Figures 4.2a** and **4.2b**). SEM images of the Gr/P composite electrode (**Figures 4.2c** and **4.2d**) demonstrate that adding phosphorous to the graphite particles did not change their spherical morphology and uniform size. The cross-sectional SEM image and the corresponding EDX results of the Gr/P diffusion-dependent electrode are shown in **Figure 4.2e**. Since there is no solid electrolyte particle in the diffusion-dependent electrode, serious problems associated with solid electrolytes can be avoided. The C and P signals were well distributed throughout the entire electrode, and it was established that there were no solid electrolyte particles (Li_6PS_5Cl) in the electrode. The X-ray diffraction (XRD) pattern of graphite, phosphorus and Gr/P composite was performed to analyze the structure of materials, and the results are shown in **Figure 4.2f**. The sharp diffraction peak in graphite observed at $2\theta = 26.6°$ was attributed to the typical graphite spacing of the (001) plane. Additionally, there are two weak peaks between 40 and 50 degrees that correspond to the crystal faces (101) and (012) of graphite [56]. The phosphorus spectrum shows two broad peaks at 15.1° and 34.2°, indicating the presence of a primarily amorphous structure that can only be interpreted by the red P allotrope [57], [58]. The Gr/P composite maintains the same crystalline structure of the phosphorus component even after phosphorus has been embedded into graphite.

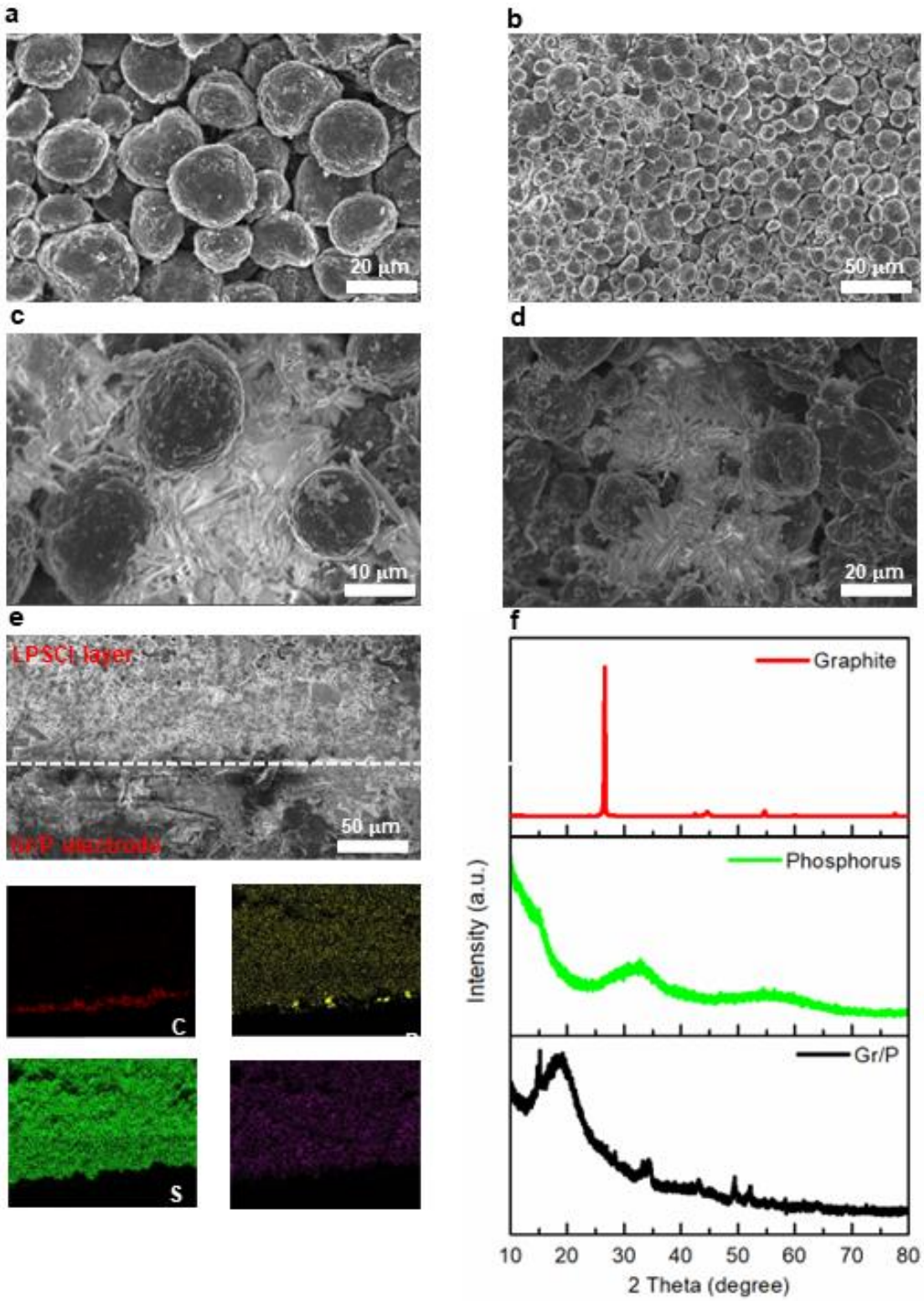

Figure 4.2: (a)-(b) SEM images of graphite. (c)-(d) SEM images of graphite/phosphorus 90/10, wt% electrode. (e) Cross-sectional SEM image and the

corresponding EDX results of the diffusion-dependent electrode with graphite and phosphorus. (f) XRD patterns of graphite, phosphorus, and Gr/P composite.

The first charge/discharge curves of Gr/P diffusion-dependent electrodes for various graphite: phosphorus ratios at 0.1 C-rate are examined in **Figure 4.3a**. The cell has an initial specific discharge capacity of 372 $mAh.g^{-1}$, 505.1 $mAh.g^{-1}$, 683.6 $mAh.g^{-1}$, 638.2 $mAh.g^{-1}$, and 444.5 $mAh.g^{-1}$ for graphite to phosphorus ratios of 70%, 80%, 85%, 90%, and 95%, respectively. Furthermore, the cell displays initial CE values of 15.1%, 18%, 38.6%, 50.7%, and 58.3% for graphite: phosphorus ratios of 70%, 80%, 85%, 90%, and 95%, respectively. The first charge/discharge differential capacity plots of Gr/P diffusion-dependent electrodes for various graphite: phosphorus ratios are investigated in **Figure 4.3b**. These plots demonstrate several peaks during discharge and a single prominent peak during charge. The significant peaks seen during the discharge are believed to be caused by the formation of LiP and Li_3P phases, while multiple smaller peaks can be seen because of different Li_xP phases, including LiP_7, LiP_5, and Li_3P_7 which are formed in sequence. However, the prominent peak observed during the charge is due to the Li_3P phase. **Figure 4.3c** compares the cycling stability and capacity retention of the Gr/P diffusion-dependent electrode for various graphite: phosphorus ratios. At 0.1 C-rate and after 10 cycles, the cell shows capacity retention values of 26.0%, 44.5%, 74.8%, 96.3%, and 97.1% for graphite: phosphorus ratios of 70%, 80%, 85%, 90%, and 95%, respectively. It is found that capacity retention decreases, and the cell exhibits poor cycling stability when the phosphorus content of the electrode increases. **Figure 4.3d** compares the CE values for various graphite: phosphorus ratios concerning the cycle number. The figure illustrates that increasing the phosphorus content in the active material causes the cell to exhibit lower CE values. These analyses conclude that the Gr/P diffusion-dependent electrode with a graphite: phosphorus ratio of 90:10 percent exhibits the best performance in terms of specific capacity and cycling stability. Therefore, the Gr/P diffusion-dependent electrode with this ratio of active materials is compared to that of graphite diffusion-dependent electrode.

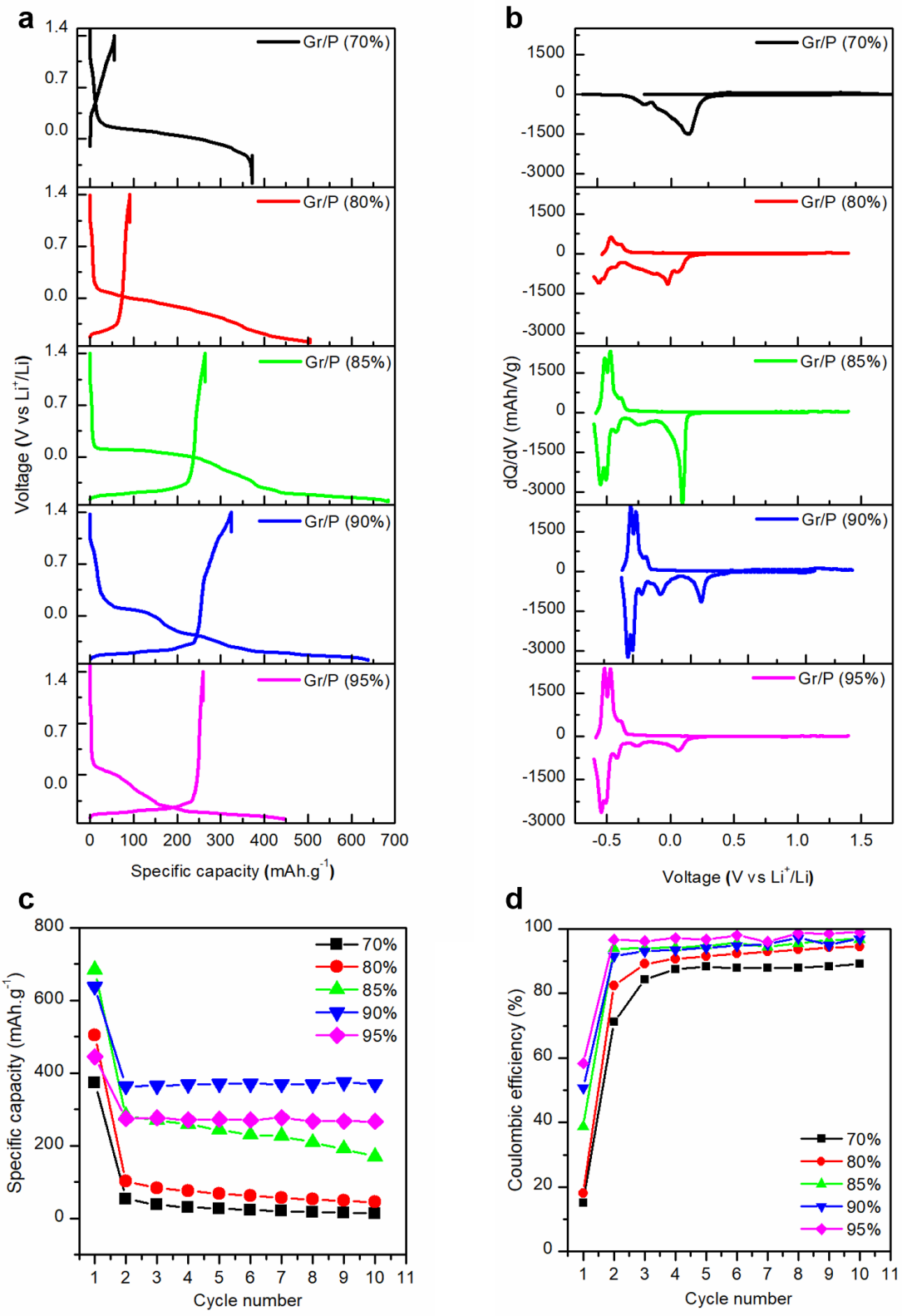
a
Gr/P (70%)
Gr/P (80%)
Gr/P (85%)
Gr/P (90%)
Gr/P (95%)
Voltage (V vs Li+/Li)
Specific capacity (mAh.g-1)
b
dQ/dV (mAh/Vg)
Voltage (V vs Li+/Li)
c
70%
80%
85%
90%
95%
Specific capacity (mAh.g-1)
Cycle number
d
Coulombic efficiency (%)
Cycle number

Figure 4.3: (a) The initial charge/discharge curves of a Gr/P diffusion-dependent electrode for different graphite: phosphorus ratios. (b) The initial charge/discharge differential capacity plots of Gr/P diffusion-dependent electrode for different graphite: phosphorus ratios. (c) The capacity retention of Gr/P diffusion-dependent electrode for different graphite: phosphorus ratios. (d) CE versus cycle number of Gr/P diffusion-dependent electrode for different graphite: phosphorus ratios.

The charge/discharge properties of graphite and Gr/P (graphite: phosphorus ratio 90:10 percent) diffusion-dependent electrodes were measured at 0.1 C-rate, as shown in **Figure 4.4a**. The experiments were carried out at 60 °C to achieve enough diffusion activity. The specific capacity of the graphite diffusion-dependent electrode was 257.8 $mAh.g^{-1}$, whereas the Gr/P diffusion-dependent electrode had a specific capacity of 638.2 $mAh.g^{-1}$, which is greater than the theoretical specific capacity that can be obtained when using graphite solely. Based on these findings, we were able to confirm that interdiffusion between the graphite and phosphorus occurs quickly because the achieved specific capacity is higher than that of the graphite diffusion-dependent electrode, and only the conventional voltage profile of graphite should be visible if the interdiffusion between the particles were inhibited [36]. The Nyquist plots obtained from Electrochemical Impedance Spectroscopy (EIS) measurements for graphite and Gr/P diffusion-dependent electrodes before cycling are shown in **Figure 4.4b**. These data demonstrating capacitive behavior revealed that the electrodes were uniformly formed without solid electrolyte particles. The impedance spectrum of each sample has a straight line in the low-frequency region, which is explained by the diffusion of lithium ions. The Gr/P Nyquist plot resembles graphite, proving that the addition of phosphorus particles does not impair the good electronic conductivity of graphite. Due to the increased lithium-ion diffusivity in the Gr/P diffusion-dependent electrode structure as compared to that graphite one, this electrode has improved performance. The galvanostatic intermittent titration technique (GITT) was applied to confirm this inference. The GITT results for the graphite and Gr/P diffusion-dependent electrodes are shown in **Figure 4.4c**. The Gr/P electrode had lower overpotential profiles than the graphite electrode, which confirms the higher average diffusivity of the Gr/P diffusion-dependent electrode compared to that of the graphite

diffusion-dependent electrode. **Figure 4.4d** illustrates the investigation of cycling retention for the graphite and Gr/P diffusion-dependent electrodes at high temperatures (60 °C) and 0.1 C-rate. The Gr/P diffusion-dependent electrode has higher specific capacity values than the graphite diffusion-dependent. Also, both electrodes have same performance in terms of capacity retention, the graphite diffusion-dependent electrode showed 92.4% capacity retention after 40 cycles and the Gr/P diffusion-dependent electrode showed 92.7% capacity retention after 40 cycles. As indicated in **Figure 4.4e**, the graphite and Gr/P diffusion-dependent electrode rate was evaluated at high temperatures (60 °C). For the graphite diffusion-dependent electrode, at 0.2, 0.3, 0.5, and 1 C-rates capacity of 72.9, 61.4, 48.4, and 33.3% to that at 0.1 C-rate were found, respectively. However, with the Gr/P diffusion-dependent electrode, the capacities of 55.3, 51.2, 40.8, and 28.0% to that at 0.1 C-rate were obtained at 0.2, 0.3, 0.5, and 1 C-rates, respectively. The capacity retention of the graphite and Gr/P diffusion-dependent electrodes at room temperature (25 °C) and 0.1 C-rate is compared in **Figure 4.4f**. The initial specific capacity of the graphite diffusion-dependent electrode is 152.2 $mAh.g^{-1}$, whereas the initial specific capacity of the Gr/P diffusion-dependent electrode is 246.4 $mAh.g^{-1}$, 66.2% of the theoretical capacity of the graphite. Additionally, the cell shows capacity retention of 87.5% and 94.8% after 9 cycles for graphite and Gr/P diffusion-dependent electrodes, respectively. These findings confirm that this study's suggested electrode offers superior cycling capabilities even at room temperature. This outstanding capability of the proposed electrode provides a new area for developing ASSBs.

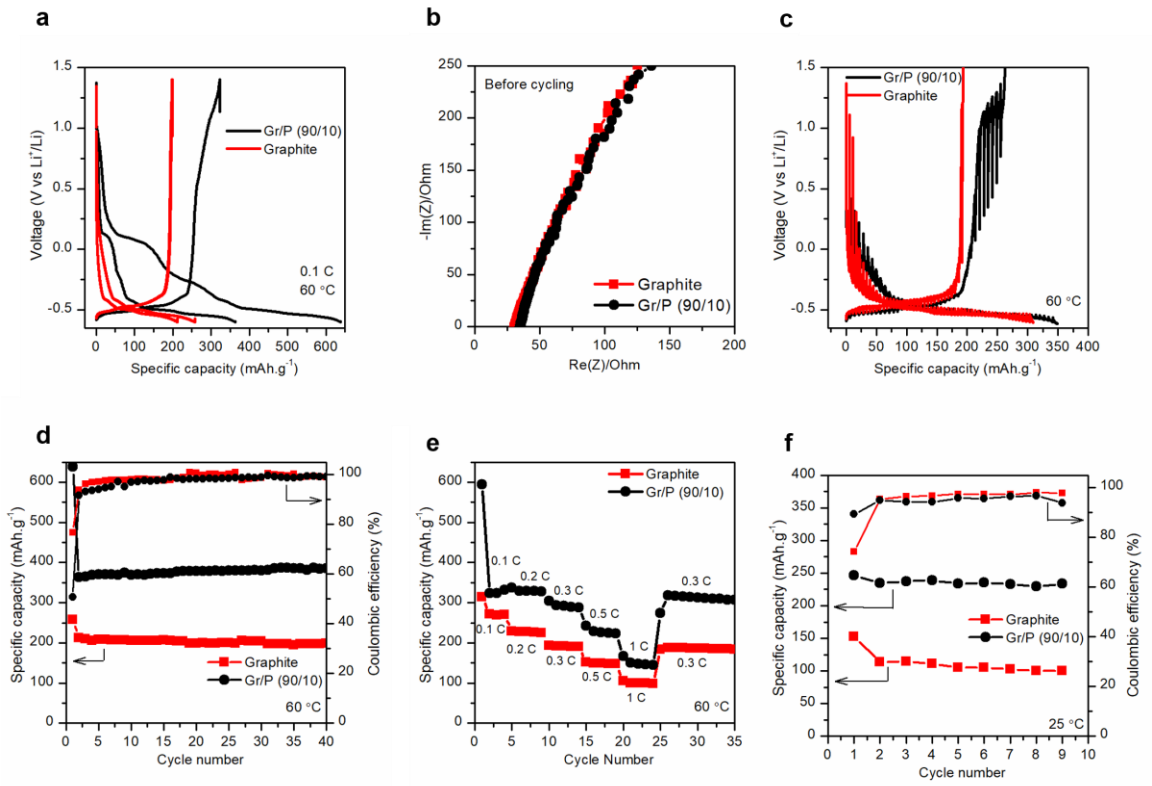

Figure 4.4: (a) The initial charge/discharge curves of the graphite and Gr/P diffusion-dependent electrodes at 0.1 C-rate and high temperature. (b) Nyquist plots of the graphite and Gr/P diffusion-dependent electrodes at room temperature before cycling. (c) GITT curves of the graphite and Gr/P diffusion-dependent electrodes at high temperatures. (d) The capacity retention of the graphite and Gr/P diffusion-dependent electrodes at high temperatures. (e) Rate performance of the graphite and Gr/P diffusion-dependent electrodes at high temperature. (f) The capacity retention of the graphite and Gr/P diffusion-dependent electrodes at room temperature.

4.4 Conclusion

In summary, we present the diffusion-dependent electrode utilizing mixed active materials of graphite and phosphorus for high-performance all-solid-state electrodes for the first time. The formation of an electrode with a highly compact structure and a high energy density was made possible by the interdiffusion of graphite and phosphorus

particles. Introducing phosphorus to diffusion-dependent electrodes can boost ion diffusion due to the formation of Li_3P alloy, a Li-ion conductor produced by the electrochemical reaction of phosphorus and lithium. As a result, the capacity increased compared to the electrode structure that utilizes graphite alone as the active material. Based on the comparison of various ratios of graphite to phosphorus in the active material, it is found that the best performing electrode in terms of specific capacity and cycling stability has 10 wt% of phosphorus to the total weight of active materials (graphite/phosphorus 90/10, wt%). This Gr/P diffusion-dependent electrode achieved a high initial specific capacity of 638.2 $mAh.g^{-1}$ with a good capacity retention of 92.7% after 40 cycles at 0.1 C-rate and high temperature. Additionally, this electrode exhibits an initial specific capacity of 246.4 $mAh.g^{-1}$ at room temperature and 0.1 C-rate, which is equal to 66.2% of the theoretical capacity of the graphite. This demonstrates the ability of the proposed electrode to operate with superior cycling performance even at low temperatures and provides new opportunities for the ASSBs' future. These findings lead us to conclude that electrode design is essential for developing high-performance ASSBs. This intriguing and straightforward electrode structure will serve as an efficient electrode configuration and inspire research into rational electrode design for high-performance ASSBs.

4.5 References

[1] Z. Zhang *et al.*, "New horizons for inorganic solid state ion conductors," *Energy Environ. Sci.*, vol. 11, no. 8, pp. 1945–1976, 2018, doi: 10.1039/c8ee01053f.

[2] Q. Zhao, S. Stalin, C.-Z. Zhao, and L. A. Archer, "Designing solid-state electrolytes for safe, energy-dense batteries," *Nat. Rev. Mater.*, vol. 5, no. 3, pp. 229–252, 2020, doi: 10.1038/s41578-019-0165-5.

[3] Y. Xiao, Y. Wang, S.-H. Bo, J. C. Kim, L. J. Miara, and G. Ceder, "Understanding interface stability in solid-state batteries," *Nat. Rev. Mater.*, vol. 5, no. 2, pp. 105–126, 2020, doi: 10.1038/s41578-019-0157-5.

[4] T. Ye, L. Li, and Y. Zhang, "Recent progress in solid electrolytes for energy storage devices," *Adv. Funct. Mater.*, vol. 30, no. 29, p. 2000077, 2020.

[5] T. Liu, Y. Yuan, X. Tao, Z. Lin, and J. Lu, "Bipolar electrodes for next-generation rechargeable batteries," *Adv. Sci.*, vol. 7, no. 17, p. 2001207, 2020.

[6] Y. Zhu, X. He, and Y. Mo, "Origin of outstanding stability in the lithium solid electrolyte materials: insights from thermodynamic analyses based on first-principles calculations," *ACS Appl. Mater. Interfaces*, vol. 7, no. 42, pp. 23685–23693, 2015.

[7] F. Han, Y. Zhu, X. He, Y. Mo, and C. Wang, "Electrochemical stability of $Li_{10}GeP_2S_{12}$ and $Li_7La_3Zr_2O_{12}$ solid electrolytes," *Adv. Energy Mater.*, vol. 6, no. 8, p. 1501590, 2016.

[8] D. H. S. Tan *et al.*, "Elucidating reversible electrochemical redox of Li_6PS_5Cl solid electrolyte," *ACS Energy Lett.*, vol. 4, no. 10, pp. 2418–2427, 2019.

[9] L. Zhou *et al.*, "Solvent-engineered design of argyrodite Li_6PS_5X (X= Cl, Br, I) solid electrolytes with high ionic conductivity," *ACS Energy Lett.*, vol. 4, no. 1, pp. 265–270, 2018.

[10] T. K. Schwietert *et al.*, “Clarifying the relationship between redox activity and electrochemical stability in solid electrolytes,” *Nat. Mater.*, vol. 19, no. 4, pp. 428–435, 2020.

[11] W. Zhang *et al.*, “Degradation mechanisms at the $Li_{10}GeP_2S_{12}/LiCoO_2$ cathode interface in an all-solid-state lithium-ion battery,” *ACS Appl. Mater. Interfaces*, vol. 10, no. 26, pp. 22226–22236, 2018.

[12] J. Zhang *et al.*, “Unraveling the intra and intercycle interfacial evolution of Li_6PS_5Cl-based all-solid-state lithium batteries,” *Adv. Energy Mater.*, vol. 10, no. 4, p. 1903311, 2020.

[13] D. Wang, C. Zhu, Y. Fu, X. Sun, and Y. Yang, “Interfaces in garnet-based all-solid-state lithium batteries,” *Adv. Energy Mater.*, vol. 10, no. 39, p. 2001318, 2020.

[14] Y. Su *et al.*, “A more stable lithium anode by mechanical constriction for solid state batteries,” *Energy Environ. Sci.*, vol. 13, no. 3, pp. 908–916, 2020.

[15] W. D. Richards, L. J. Miara, Y. Wang, J. C. Kim, and G. Ceder, “Interface Stability in Solid-State Batteries,” *Chem. Mater.*, vol. 28, no. 1, pp. 266–273, 2016, doi: 10.1021/acs.chemmater.5b04082.

[16] G.-L. Zhu *et al.*, “Interfacial redox behaviors of sulfide electrolytes in fast-charging all-solid-state lithium metal batteries,” *Energy Storage Mater.*, vol. 31, pp. 267–273, 2020.

[17] H. Huo *et al.*, “Li_2CO_3 effects: New insights into polymer/garnet electrolytes for dendrite-free solid lithium batteries,” *Nano Energy*, vol. 73, p. 104836, 2020.

[18] C. Wang *et al.*, “Interface-assisted in-situ growth of halide electrolytes eliminating interfacial challenges of all-inorganic solid-state batteries,” *Nano Energy*, vol. 76, p. 105015, 2020.

[19] A. Banerjee, X. Wang, C. Fang, E. A. Wu, and Y. S. Meng, “Interfaces and

interphases in all-solid-state batteries with inorganic solid electrolytes," *Chem. Rev.*, vol. 120, no. 14, pp. 6878–6933, 2020.

[20] S. Ohno, C. Rosenbach, G. F. Dewald, J. Janek, and W. G. Zeier, "Linking Solid Electrolyte Degradation to Charge Carrier Transport in the Thiophosphate-Based Composite Cathode toward Solid-State Lithium-Sulfur Batteries," *Adv. Funct. Mater.*, vol. 31, no. 18, p. 2010620, 2021.

[21] D. H. Kim *et al.*, "Infiltration of Solution-Processable Solid Electrolytes into Conventional Li-Ion-Battery Electrodes for All-Solid-State Li-Ion Batteries," *Nano Lett.*, vol. 17, no. 5, pp. 3013–3020, May 2017, doi: 10.1021/acs.nanolett.7b00330.

[22] F. Hippauf *et al.*, "Overcoming binder limitations of sheet-type solid-state cathodes using a solvent-free dry-film approach," *Energy Storage Mater.*, vol. 21, pp. 390–398, 2019.

[23] T. Shi *et al.*, "High Active Material Loading in All-Solid-State Battery Electrode via Particle Size Optimization," *Adv. Energy Mater.*, vol. 10, no. 1, 2020, doi: 10.1002/aenm.201902881.

[24] J. Y. Kim *et al.*, "Efficient cell design and fabrication of concentration-gradient composite electrodes for high-power and high-energy-density all-solid-state batteries," *ETRI J.*, vol. 42, no. 1, pp. 129–137, 2020.

[25] Y. Xiao *et al.*, "Electrolyte melt infiltration for scalable manufacturing of inorganic all-solid-state lithium-ion batteries," *Nat. Mater.*, vol. 20, no. 7, pp. 984–990, 2021.

[26] H. Deiseroth *et al.*, "Li_6PS_5X: a class of crystalline Li-rich solids with an unusually high Li^+ mobility," *Angew. Chemie Int. Ed.*, vol. 47, no. 4, pp. 755–758, 2008.

[27] N. Kamaya *et al.*, "A lithium superionic conductor," *Nat. Mater.*, vol. 10, no. 9, pp. 682–686, 2011, doi: 10.1038/nmat3066.

[28] Y. Kato *et al.*, “High-power all-solid-state batteries using sulfide superionic conductors,” *Nat. Energy*, vol. 1, no. 4, p. 16030, 2016, doi: 10.1038/nenergy.2016.30.

[29] A. Bielefeld, D. A. Weber, and J. Janek, “Microstructural modeling of composite cathodes for all-solid-state batteries,” *J. Phys. Chem. C*, vol. 123, no. 3, pp. 1626–1634, 2018.

[30] J. Y. Kim *et al.*, “Revisiting TiS_2 as a diffusion-dependent cathode with promising energy density for all-solid-state lithium secondary batteries,” *Energy Storage Mater.*, vol. 41, pp. 289–296, 2021.

[31] D. H. S. Tan *et al.*, “Carbon-free high-loading silicon anodes enabled by sulfide solid electrolytes,” *Science (80-.).*, vol. 373, no. 6562, pp. 1494–1499, 2021.

[32] J. Sakabe, N. Ohta, T. Ohnishi, K. Mitsuishi, and K. Takada, “Porous amorphous silicon film anodes for high-capacity and stable all-solid-state lithium batteries,” *Commun. Chem.*, vol. 1, no. 1, pp. 1–9, 2018.

[33] F. Strauss et al., “Impact of Cathode Material Particle Size on the Capacity of Bulk-Type All-Solid-State Batteries,” ACS Energy Lett., vol. 3, no. 4, pp. 992–996, Apr. 2018, doi: 10.1021/acsenergylett.8b00275.

[34] X. Chen, W. He, L.-X. Ding, S. Wang, and H. Wang, “Enhancing interfacial contact in all solid state batteries with a cathode-supported solid electrolyte membrane framework,” *Energy Environ. Sci.*, vol. 12, no. 3, pp. 938–944, 2019, doi: 10.1039/c8ee02617c.

[35] N. Ohta, S. Kimura, J. Sakabe, K. Mitsuishi, T. Ohnishi, and K. Takada, “Anode properties of Si nanoparticles in all-solid-state Li batteries,” *ACS Appl. Energy Mater.*, vol. 2, no. 10, pp. 7005–7008, 2019.

[36] J. Y. Kim *et al.*, “Diffusion-dependent graphite electrode for all-solid-state batteries with extremely high energy density,” *ACS Energy Lett.*, vol. 5, no. 9, pp.

2995–3004, 2020.

[37] J. Park *et al.*, “Dimension-controlled solid oxide electrolytes for all-solid-state electrodes: Percolation pathways, specific contact area, and effective ionic conductivity,” *Chem. Eng. J.*, vol. 391, p. 123528, 2020.

[38] S. Cangaz *et al.*, “Enabling High-Energy Solid-State Batteries with Stable Anode Interphase by the Use of Columnar Silicon Anodes,” *Adv. Energy Mater.*, vol. 10, no. 34, p. 2001320, 2020.

[39] A. L. Davis *et al.*, “Rate limitations in composite solid-state battery electrodes: revealing heterogeneity with operando microscopy,” *ACS Energy Lett.*, vol. 6, no. 8, pp. 2993–3003, 2021.

[40] J. Y. Kim *et al.*, “Graphite–Silicon Diffusion-Dependent Electrode with Short Effective Diffusion Length for High-Performance All-Solid-State Batteries,” *Adv. Energy Mater.*, vol. 12, no. 3, p. 2103108, 2022.

[41] C. Marino, A. Debenedetti, B. Fraisse, F. Favier, and L. Monconduit, “Activated-phosphorus as new electrode material for Li-ion batteries,” *Electrochem. commun.*, vol. 13, no. 4, pp. 346–349, 2011, doi: https://doi.org/10.1016/j.elecom.2011.01.021.

[42] R. Yazami, “Surface chemistry and lithium storage capability of the graphite–lithium electrode,” *Electrochim. Acta*, vol. 45, no. 1, pp. 87–97, 1999, doi: https://doi.org/10.1016/S0013-4686(99)00195-4.

[43] L.-Q. Sun, M.-J. Li, K. Sun, S.-H. Yu, R.-S. Wang, and H.-M. Xie, “Electrochemical Activity of Black Phosphorus as an Anode Material for Lithium-Ion Batteries,” *J. Phys. Chem. C*, vol. 116, no. 28, pp. 14772–14779, Jul. 2012, doi: 10.1021/jp302265n.

[44] Y. Kim *et al.*, “An amorphous red phosphorus/carbon composite as a promising anode material for sodium ion batteries,” *Adv. Mater.*, vol. 25, no. 22, pp. 3045–

3049, 2013.

[45] M. C. Stan, J. von Zamory, S. Passerini, T. Nilges, and M. Winter, “Puzzling out the origin of the electrochemical activity of black P as a negative electrode material for lithium-ion batteries,” *J. Mater. Chem. A*, vol. 1, no. 17, pp. 5293–5300, 2013.

[46] Z. Yu, J. Song, M. L. Gordin, R. Yi, D. Tang, and D. Wang, “Phosphorus-graphene nanosheet hybrids as lithium-ion anode with exceptional high-temperature cycling stability,” *Adv. Sci.*, vol. 2, no. 1–2, p. 1400020, 2015.

[47] Y. Zhang *et al.*, “Wet-Chemical Processing of Phosphorus Composite Nanosheets for High-Rate and High-Capacity Lithium-Ion Batteries,” *Adv. Energy Mater.*, vol. 6, no. 10, p. 1502409, 2016.

[48] J. Sun *et al.*, “A phosphorene–graphene hybrid material as a high-capacity anode for sodium-ion batteries,” *Nat. Nanotechnol.*, vol. 10, no. 11, pp. 980–985, 2015, doi: 10.1038/nnano.2015.194.

[49] C. Park and H. Sohn, “Black phosphorus and its composite for lithium rechargeable batteries,” *Adv. Mater.*, vol. 19, no. 18, pp. 2465–2468, 2007.

[50] L. Wang *et al.*, “Nano-structured phosphorus composite as high-capacity anode materials for lithium batteries,” *Angew. Chemie*, vol. 124, no. 36, pp. 9168–9171, 2012.

[51] X. Ma, G. Ning, C. Qi, C. Xu, and J. Gao, “Phosphorus and Nitrogen Dual-Doped Few-Layered Porous Graphene: A High-Performance Anode Material for Lithium-Ion Batteries,” *ACS Appl. Mater. Interfaces*, vol. 6, no. 16, pp. 14415–14422, Aug. 2014, doi: 10.1021/am503692g.

[52] F.-Y. Su *et al.*, “Could graphene construct an effective conducting network in a high-power lithium ion battery?,” *Nano Energy*, vol. 1, no. 3, pp. 429–439, 2012, doi: https://doi.org/10.1016/j.nanoen.2012.02.004.

[53] Y.-X. Wang, S.-L. Chou, H.-K. Liu, and S.-X. Dou, “Reduced graphene oxide with superior cycling stability and rate capability for sodium storage,” *Carbon N. Y.*, vol. 57, pp. 202–208, 2013, doi: https://doi.org/10.1016/j.carbon.2013.01.064.

[54] J. Sun *et al.*, “Formation of Stable Phosphorus–Carbon Bond for Enhanced Performance in Black Phosphorus Nanoparticle–Graphite Composite Battery Anodes,” *Nano Lett.*, vol. 14, no. 8, pp. 4573–4580, Aug. 2014, doi: 10.1021/nl501617j.

[55] Y. Li, Y. Lu, P. Adelhelm, M.-M. Titirici, and Y.-S. Hu, “Intercalation chemistry of graphite: alkali metal ions and beyond,” *Chem. Soc. Rev.*, vol. 48, no. 17, pp. 4655–4687, 2019.

[56] F. Y. Ban, S. R. Majid, N. M. Huang, and H. N. Lim, “Graphene oxide and its electrochemical performance,” *Int. J. Electrochem. Sci*, vol. 7, no. 5, pp. 4345–4351, 2012.

[57] Y. Wang, L. Tian, Z. Yao, F. Li, S. Li, and S. Ye, “Enhanced reversibility of red phosphorus/active carbon composite as anode for lithium ion batteries,” *Electrochim. Acta*, vol. 163, pp. 71–76, 2015.

[58] W. Li, Z. Yang, Y. Jiang, Z. Yu, L. Gu, and Y. Yu, “Crystalline red phosphorus incorporated with porous carbon nanofibers as flexible electrode for high performance lithium-ion batteries,” *Carbon N. Y.*, vol. 78, pp. 455–462, 2014.

5 Chapter 5: Hard Carbon Diffusion-Dependent Electrode for Sulfide-Based All-Solid-State Lithium-Ion Batteries

5.1 Introduction

All-solid-state batteries (ASSBs) have become up-and-coming energy storage technologies with the potential to achieve the highest levels of safety and energy density [1]–[4]. To realize all-solid-state lithium-ion batteries (ASSLIBs), solid-state electrolytes (SSEs) should be used to replace liquid electrolytes used in traditional lithium-ion batteries (LIBs). It is highly desirable to develop solid electrolytes with outstanding electrochemical characteristics [5]–[8]. Over the past few years, many SSEs have been developed, including oxide, sulfide, halide, and polymer solid electrolytes. In particular, oxide and sulfide solid electrolytes have undergone extensive study for high-performance ASSBs [9], [10]. The sulfide-based solid electrolytes typically display high ionic conductivity and a mechanically adaptable interface with high deformability [11]–[13]. In ASSBs, the solid sulfide electrolyte is typically used in two parts. First, for effective lithium-ion transport between the two electrodes, while avoiding direct electrical shorting, the solid electrolyte layer between the cathode and the anode is constructed from the solid electrolyte powders [14]–[17]. Second, the solid sulfide electrolyte is included in the composite electrode with active materials to replicate the porous electrode in LIBs that employ liquid electrolytes [18]–[22]. However, composite electrodes have many interfacial reactions because of sulfide solid electrolytes' intrinsic narrow stability window. In addition, the large portion of inactive SSE in the composite electrodes compromises the energy density of ASSBs.

In recent years, diffusion-dependent electrodes have gained increasing attention because of the reduced interfacial contact, good process compatibility, and increased energy density compared to composite electrodes. So far, many electrode materials have been studied for developing diffusion-dependent solid-state cathode and anode. In this

scenario, $Li_2Ru_{0.8}S_{0.2}O_{3.2}$, developed by A. Sakuda et al., is an ion and electron mixed conductor that may be used as the cathode material for ASSBs without the requirement for extra carbon additions or SSEs [23]. In a further study, Y. Lee et al. designed a diffusion-dependent solid-state TiS_2 electrode. High areal and volumetric capacities of 9.43 $mAh.cm^{-2}$ and 578 $mAh.cm^{-3}$, respectively, are produced by this electrode at a loading level of 45.6 $mg.cm^{-2}$ [24]. S. Meng's team also reported a micro silicon diffusion-dependent electrode for ASSBs because of the material's high electronic conductivity (~ 3 × 10^{-5} $S.cm^{-1}$) and strong Li-ion diffusivity [25]. Y. Lee's group proposed a diffusion-dependent graphite electrode using a conventional slurry casting method. According to their research, Li-ion self-diffusion inside graphite electrodes can reach an areal capacity of 2 ~ 6 $mAh.cm^{-2}$ at a high temperature in a high-loading graphite electrode [26]. Following this research, they introduced a graphite-silicon diffusion-dependent electrode for ASSBs with a short effective diffusion length [27]. However, another critical anode material, hard carbon (HC), has never been investigated in diffusion-dependent electrodes for sulfide-based ASSLIBs.

Inspired by the advantages of HC, such as its higher capacity, longer lifespan, improved rate performance, and higher level of safety compared to conventional carbonaceous anode materials [28]–[34], here we first report HC diffusion-dependent electrodes for sulfide-based ASSLIBs. This work gives a novel all-solid-state electrode design that uses a simple electrode composition to boost energy density and improve electrochemical performance noticeably. The solid electrolyte, often present in significant quantities in the composite-type all-solid-state electrode, is absent from the proposed all-solid-state electrode and is replaced by an active material and a polymeric binder. This suggested electrode uses the diffusion-based lithium-ion transport of active materials among themselves for charge-discharge, as opposed to the composite electrode design that partially consists of the solid electrolyte, which provides lithium-ion migration through the percolated pathway of the solid electrolyte particles. The interface between the active materials is intended to be seamless in the proposed all-solid-state electrode. In this case, HC is chosen as the suitable active material to illustrate this novel all-solid-state electrode approach. Due to the high electronic conductivity that HC inherently possesses, it is

possible to construct an efficient model without taking the spatial placement of the conducting agent into account [35]. In addition, HC is notable for its ability to deform mechanically in response to an applied force. As a result, in a compressed state, the HC particles can come close to one another, making it easier for lithium ions to diffuse. Therefore, the electrode can hold as much active material as the solid electrolyte excluded in this configuration. Thus, the all-solid-state electrode's volumetric capacity can be significantly increased.

5.2 Methods

5.2.1 Fabrication of Liquid Cells

Commercial HC was used for preparing the electrodes. To fabricate the negative electrodes for liquid cells, the HC particles were combined with the PVDF binder and Super P C65 conductive additive in a weight ratio of 90:5:5 in NMP solvent to create a slurry. This slurry was cast onto carbon-coated copper foil and let dried overnight at 100 °C in a vacuum oven. Lithium metal was used as the anode to assemble CR2032 coin half-cells. A 1:1:1 mixture of EC, DMC, and EMC was utilized as an electrolyte, which included 1 M $LiPF_6$.

5.2.2 Fabrication of All-Solid-State Batteries

The HC and PVDF were combined in NMP in a 98:2 weight ratio to create a slurry for a diffusion-dependent electrode. The resultant slurry was deposited on carbon-coated copper foil current collectors using the controlled doctor blade approach. The electrode was then dried for 24 hours at 100 °C in a vacuum oven to remove all solvent traces. Roll-pressing was applied to the diffusion-dependent electrode to ensure structural stability and create a seamless interface between HC particles. Li_6PS_5Cl (LPSCl) powder of 100 mg was pelletized under 0.5 tons in a polyether ether ketone mold with a diameter of 13 mm to create a solid electrolyte layer. Separately, the HC electrode was pressed under 0.5 tons, and then it was joined with the pre-pelletized Li_6PS_5Cl layer by pressing

under 4 tons once more. The Li-In alloy was used as the counter electrode to create half-cells.

5.2.3 Electrochemical Measurement

For the liquid cells, GCD tests were performed at room temperature (25 °C) with CC discharging and CC charging between 0 and 2 V. For the cycling performance testing, the cells were cycled at C/10 rate for the first 5 cycles and C/3 rate for the following 100 cycles. For the rate capability tests, the cells completed 5 cycles at the following rates: C/10, C/4, C/3, C/2, 1C, and 2C, followed by 5 cycles at the C/10 rate.

For the ASSBs, GCD tests were performed at both room temperature (25 °C) and high temperature (60 °C) with CC discharging and CC charging between -0.6 and 1.4 V (due to the presence of In in the anode part). For the cycling performance testing, the cells were cycled at a 0.1C rate for 100 cycles. For the rate capability tests, the cells completed 5 cycles at the following rates: 0.1C, 0.2C, 0.3C, 0.5C, and 1C, followed by 5 cycles at 0.3C rate. The cells were tested at both normal and high pressure (2 tons).

5.2.4 SEM and EDX

Surface morphology was characterized using a Hitachi S-4800 SEM in the secondary electron mode, with an acceleration voltage of 5.0 kV and a working distance of 5 mm. Also, the scanning electron microscope's X-ray detector attachment was used for the EDX study, with a working distance of 15 mm and an acceleration voltage of 20.0 kV.

5.2.5 XRD

Using Cu Kα radiation (λ = 1.54178 Å) and a particular container to prevent exposure to air during tests, X-ray powder diffraction was carried out using an X-ray diffraction diffractometer (XRD, Bruker AXS D8 Advance) to analyze the crystal structure of the samples between 2 theta between 10 ° and 80 °.

5.3 Results and Discussion

Schematic representations of the standard composite electrode and the all-solid-state diffusion-dependent electrode are shown in **Figure 5.1**. As previously explained, to migrate lithium ions into the active material in the composite electrode, the solid electrolyte is included with it. In contrast, the designed electrode in this study receives the lithium ions from the interface with the solid electrolyte layer and only permits the ions to transit within the electrode by self-diffusion.

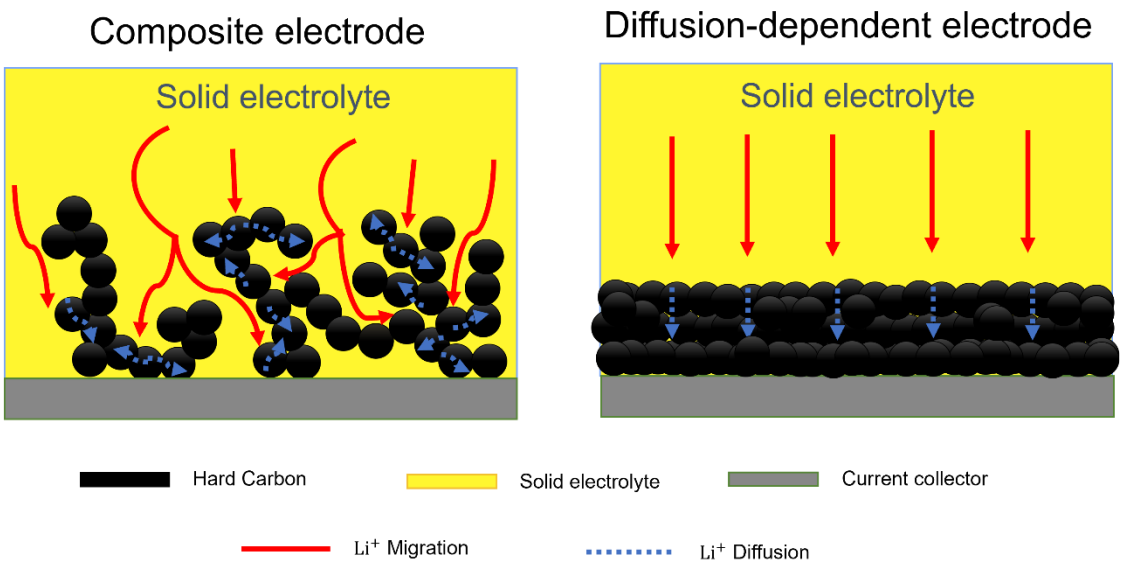

Figure 5.1: Schematic comparison of the all-solid-state composite electrode and the diffusion-dependent electrode.

Figures 5.2a to 5.2c display the scanning electron microscopy (SEM) images of the HC electrode. The figures show that this sample has a non-uniform morphology and a sharp edge. HC does not typically have a shape with well-developed edges, indicating that it was pulverized after being processed. **Figure 5.2d** displays the HC powders' X-ray diffraction (XRD) pattern. The peaks at 24.4°, 43.6°, and 79.4° are associated with (002), (100), and (110) diffraction peaks. This was an example of an amorphous carbon structure with a lower degree of graphitization. The sample's peak at 24.4° is associated with its graphene-like structure, while the smaller peak at 43.6° is associated with

creating a disordered carbon substance, according to data from previous studies [36]. To determine the proportion of single layers in HC materials, Liu et al. defined an empirical parameter R that refers to the ratio of the height of the (002) peak against the background [37]. In general, the percentage of single layers decreases as the R increases. The presence of such a high R in this instance, which equals 2.2, indicates that the single-layer content is insignificant.

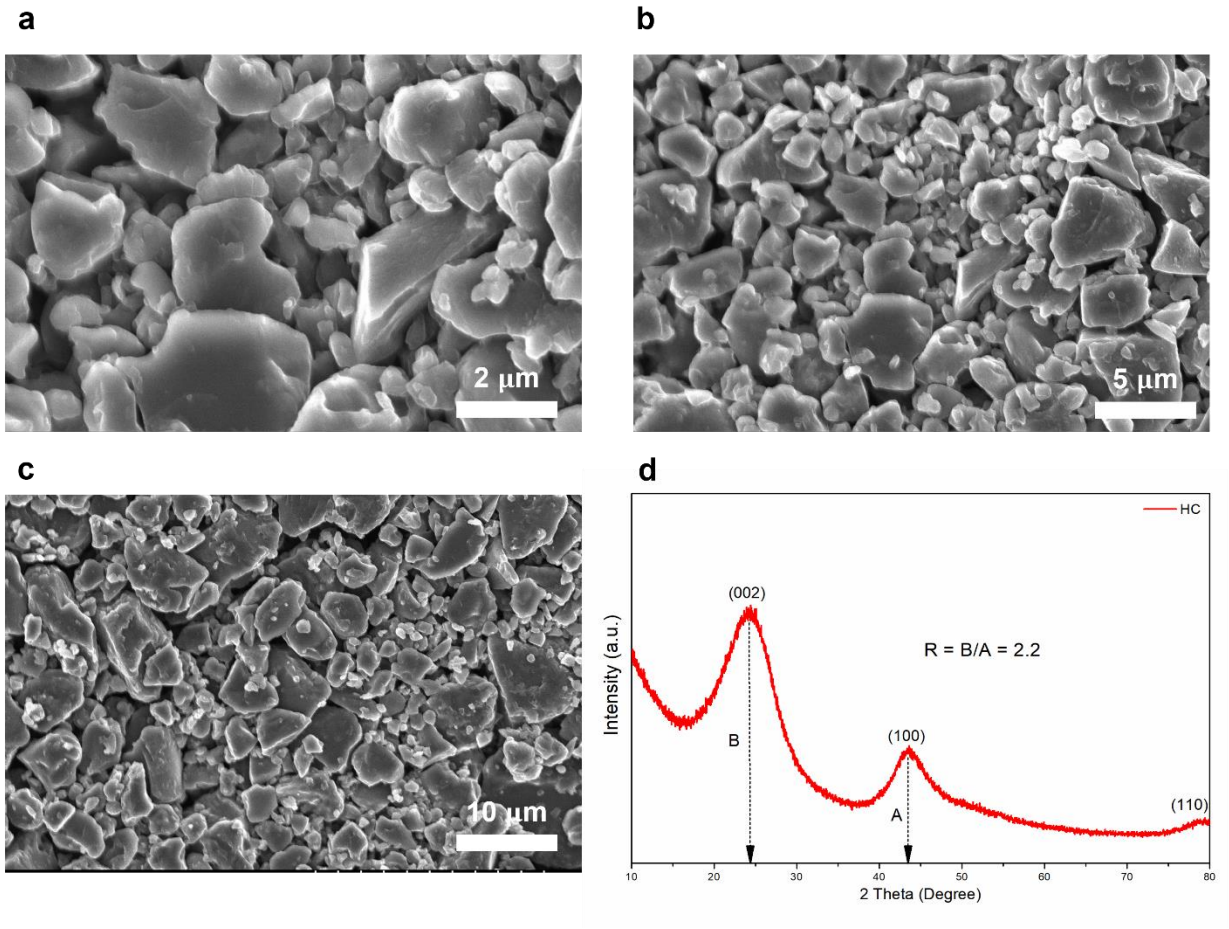

Figure 5.2: (a)-(c) SEM images of HC electrode, (d) XRD patterns of HC.

Results from SEM and energy dispersive X-ray spectroscopy (EDX) on a compressed HC electrode with a solid electrolyte layer are shown in **Figure 5.3a**. The solid electrolyte layer and the HC electrode were individually pressed and merged as one body to avoid tiny solid electrolyte particles from entering the pores of the HC electrode during the compressing process. It was proven from the morphological observation in **Figure 5.3a**

that the mechanically compliant HC particles may come into close contact with one another, changing their initial shape. It is implied that there are no LPSCl particles in the HC electrode by the stark contrast between the HC layer and the solid electrolyte layer. Additionally, the EDX results of **Figure 5.3a** demonstrate that the C signal (from HC) and the S, P, and Cl signals (from LPSCl) are undeniably separated. Impedance measurements provide more evidence. If the electronic resistance is significantly less than the ionic resistance, impedance measurements state that the ionic resistance in a mixed conductor is described as a vector with a half-phase angle to that of the ionic conductor [38]–[40]. The Nyquist plot of the impedance spectra of the diffusion-dependent HC electrode in ASSLIB is shown in **Figure 5.3b**. Due to the electrode's role as an electronic conductor, the diffusion-dependent electrode displays the typical capacitive behavior of the LPSCl layer. These results provide further evidence that an electrode can be created without a solid electrolyte.

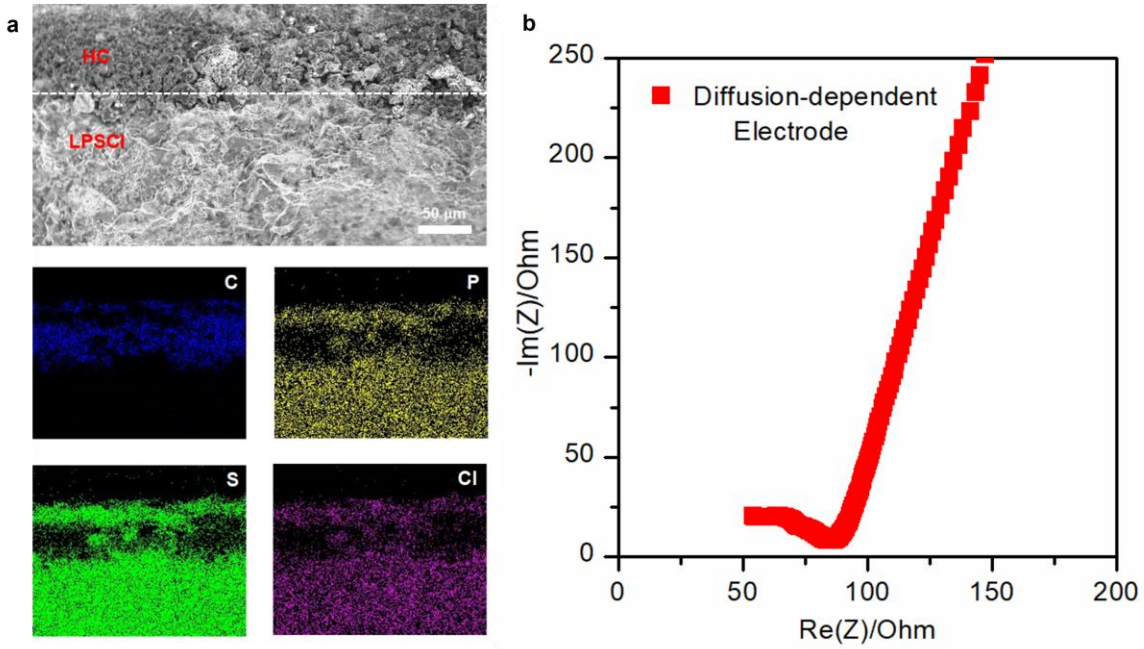

Figure 5.3: (a) Cross-sectional SEM and corresponding EDX images of the all-solid-state diffusion-dependent electrode, (b) Nyquist plot of the all-solid-state diffusion-dependent electrode at room temperature before cycling.

To check the electrochemical performance of HC, we first test it in a coin cell and evaluate its discharge capacity, cycling stability, and rate performance in liquid LIBs. As shown in **Figure 5-S1**, the cell exhibits an initial discharge capacity of 352.7 $mAh.g^{-1}$ and an initial CE of 98.6% at a 0.1C rate. Also, this cell displays capacity retention of 89.2% after 100 cycles at a C/3 rate. This information will be used to evaluate and compare the performance of the solid-state cells.

Diffusion-dependent HC electrodes were coupled with lithium-indium alloy (Li-In) as counter electrodes for the solid-state batteries' electrochemical evaluation, and they were evaluated at normal and high temperatures and pressure. In contrast to LIBs that use a liquid electrolyte, one key advantage of ASSBs is their capacity to function in a wide temperature range, including high temperatures [26]. As shown in **Figures 5.4a-d**, the fabricated cells' charge-discharge characteristics were obtained at room temperature (RT) and high temperature (HT), which is 60 °C. The results show that the cell exhibits higher initial specific capacity at HT but lower cycling stability than the RT values. This is because lithium ions' diffusion and conduction are enhanced at 60 °C [35]. **Figures 5.4a** and **5.4c**, show CC charge-discharge voltage profiles of the initial cycles at 0.1C rate, at RT and HT. **Figure 5.4b** exhibits the cycling performance of the cell at RT, and **Figure 5.4d** compares the performance and stability at RT and HT. As was already indicated, although the cell exhibits increased specific capacity at higher temperatures, the capacity decays very quickly and the cell displays poor cycling stability. The cells were tested at both high temperature and pressure to address this issue and enhance cycling stability. **Figure 5.4e** shows CC charge-discharge voltage profiles of the initial cycles at 0.1C rate, at HT and high pressure (HP). A comparison of the cycling performance at low and high testing pressures is shown in **Figure 5.4f** as well. The results show that the cell has greater specific capacities and improved cycling stability at higher pressure. Since the cell performs best in conditions of HT and HP in terms of capacity and stability, the rate capability was also examined in this scenario. **Figure 5.4g** displays the voltage profiles of the diffusion-dependent HC electrode at various current densities from 0.1 to 1C at HT and HP. Also, **Figure 5.4h** exhibits the specific capacity of the diffusion-dependent HC electrode for various C-rates at both HT and HP. The cell exhibits initial discharge

capacity of 514.4 $mAh.g^{-1}$ and initial CE of 38.4% at 0.1C rate. Also, the capacity retention after 100 cycles and at 0.1C rate is equal to 76.7%. According to the information provided for LIBs, these results are reasonable and comparable with liquid cells. The suggested diffusion-dependent electrode shows higher specific capacities, but lower cycling stability compared to the liquid cells. The cycling stability issue can be addressed by different methods such as carbon coating, the addition of a secondary phase, or oxidizing treatment in future works to achieve an exceptionally stable performance of the cells.

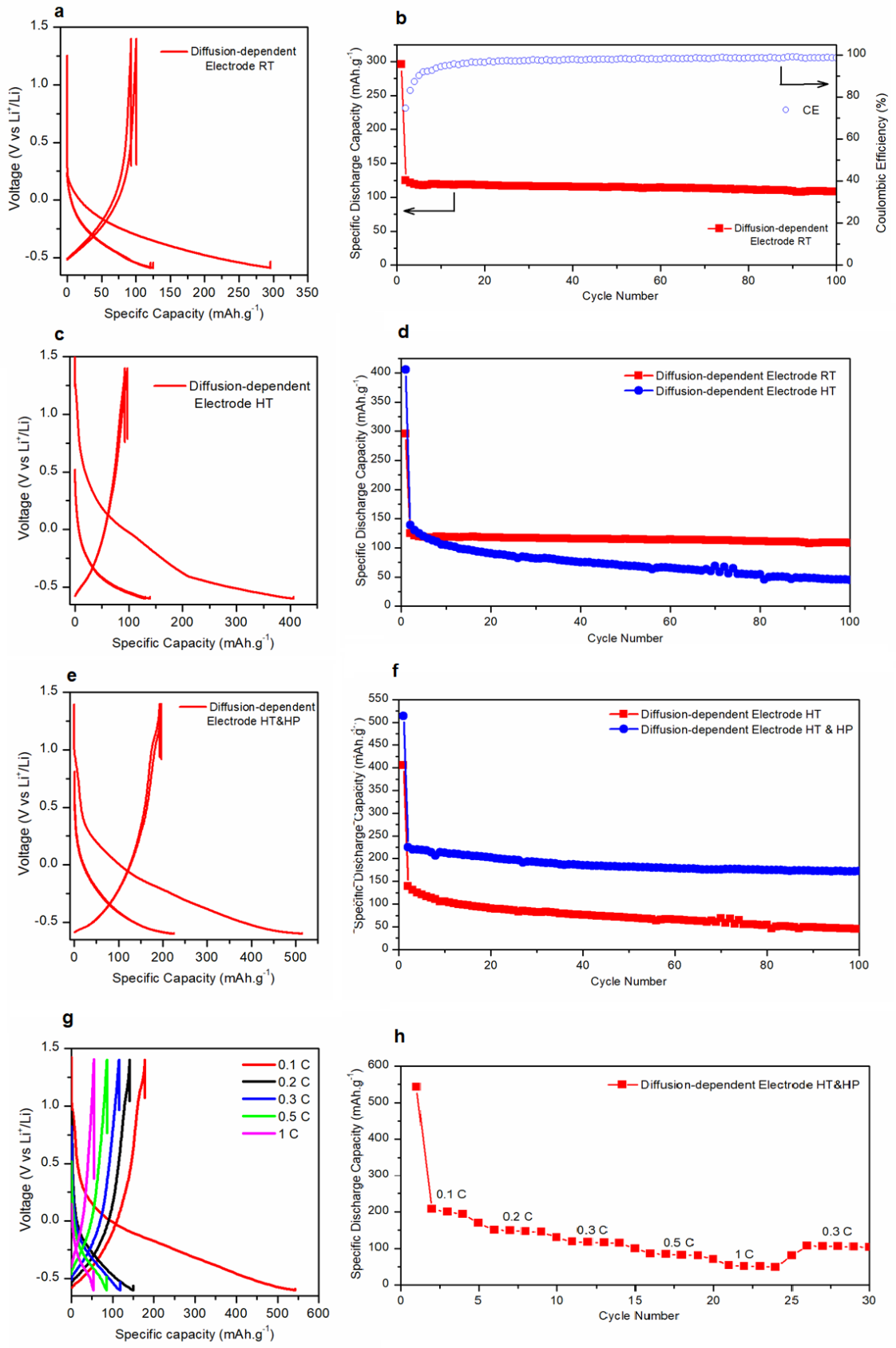
a
Diffusion-dependent Electrode RT
Voltage (V vs Li+/Li)
Specifc Capacity (mAh.g-1)
b
Specific Discharge Capacity (mAh.g-1)
Coulombic Efficiency (%)
CE
Diffusion-dependent Electrode RT
Cycle Number
c
Diffusion-dependent Electrode HT
Voltage (V vs Li+/Li)
Specific Capacity (mAh.g-1)
d
Diffusion-dependent Electrode RT
Diffusion-dependent Electrode HT
Specific Discharge Capacity (mAh.g-1)
Cycle Number
e
Diffusion-dependent Electrode HT&HP
Voltage (V vs Li+/Li)
Specific Capacity (mAh.g-1)
f
Diffusion-dependent Electrode HT
Diffusion-dependent Electrode HT & HP
Specific Discharge Capacity (mAh.g-1)
Cycle Number
g
0.1 C
0.2 C
0.3 C
0.5 C
1 C
Voltage (V vs Li+/Li)
Specific capacity (mAh.g-1)
h
Diffusion-dependent Electrode HT&HP
Specific Discharge Capacity (mAh.g-1)
0.1 C
0.2 C
0.3 C
0.5 C
1 C
0.3 C
Cycle Number

Figure 5.4: (a) Charge−discharge voltage profiles of the all-solid-state diffusion-dependent electrode at RT. (b) The capacity retention of the HC diffusion-dependent electrode at RT. (c) Charge−discharge voltage profiles of the all-solid-state diffusion-dependent electrode at HT. (d) Capacity retention comparison of the HC diffusion-dependent electrode at RT and HT. (e) Charge−discharge voltage profiles of the all-solid-state diffusion-dependent electrode at HT and HP. (f) Capacity retention comparison of the HC diffusion-dependent electrode at low pressure and HP. (g) Diffusion-dependent HC electrode voltage profiles at various current densities from 0.1 to 1 C at HT and HP. (h) Rate performance of the all-solid-state diffusion-dependent electrode at HT and HP.

5.4 Conclusion

In summary, a hard carbon diffusion-dependent electrode was investigated in sulfide-based ASSLIBs for the first time. A novel type of all-solid-state electrodes that are appropriate for ASSBs is introduced. A unique electrode made of closely packed HC materials and entirely excludes the solid electrolyte is offered as an alternative to the typical composite electrode design that mimics the electrode in LIBs employing a liquid electrolyte. The diffusion between the HC particles with a seamless surface was extensively utilized for lithium-ion transport throughout the HC electrode. Systematic experiments confirm that interparticle diffusion is enabled in the suggested electrode, and improved performance could be obtained. Although the cycling and rate performances of the diffusion-dependent electrode were not particularly noticeable at RT due to a restriction on the lithium diffusion velocity, the feature could be enhanced through operation at HT, which is a significant advantage of ASSBs. However, even at high temperatures, cycling stability is still a problem. Thus, to address this issue, the cells underwent testing at HP. Finally, the proposed diffusion-dependent electrode demonstrated higher rate performance and stable capacity retention at high temperatures and pressure. The cell has an initial discharge capacity of 514.4 $mAh.g^{-1}$ and an initial CE of 38.4% at a 0.1C rate. Additionally, at 0.1C rate and after 100 cycles, the capacity retention equals to 76.7%. These results are close and comparable with the results

achieved for liquid LIBs. However, the cycling stability could be improved by methods such as carbon coating, the addition of a secondary phase, or oxidizing treatment to achieve a stable performance of ASSBs. These findings thus provide a viable approach for producing a high-performance, all-solid-state electrode using a simple technique and open a new venue for developing ASSBs.

5.5 References

[1] Y. Wang *et al.*, “Design principles for solid-state lithium superionic conductors,” *Nat. Mater.*, vol. 14, no. 10, pp. 1026–1031, 2015, doi: 10.1038/nmat4369.

[2] J. Wan, J. Xie, D. G. Mackanic, W. Burke, Z. Bao, and Y. Cui, “Status, promises, and challenges of nanocomposite solid-state electrolytes for safe and high performance lithium batteries,” *Mater. Today Nano*, vol. 4, pp. 1–16, 2018, doi: https://doi.org/10.1016/j.mtnano.2018.12.003.

[3] Y.-S. Hu and Y. Lu, “2019 Nobel Prize for the Li-Ion Batteries and New Opportunities and Challenges in Na-Ion Batteries,” *ACS Energy Lett.*, vol. 4, no. 11, pp. 2689–2690, Nov. 2019, doi: 10.1021/acsenergylett.9b02190.

[4] H.-D. Lim *et al.*, “A review of challenges and issues concerning interfaces for all-solid-state batteries,” *Energy Storage Mater.*, vol. 25, pp. 224–250, 2020, doi: https://doi.org/10.1016/j.ensm.2019.10.011.

[5] J. Li, C. Ma, M. Chi, C. Liang, and N. J. Dudney, “Solid electrolyte: The key for high-voltage lithium batteries,” *Adv. Energy Mater.*, vol. 5, no. 4, 2015, doi: 10.1002/aenm.201401408.

[6] J. C. Bachman *et al.*, “Inorganic Solid-State Electrolytes for Lithium Batteries: Mechanisms and Properties Governing Ion Conduction,” *Chem. Rev.*, vol. 116, no. 1, pp. 140–162, 2016, doi: 10.1021/acs.chemrev.5b00563.

[7] Z. Zhang *et al.*, “New horizons for inorganic solid state ion conductors,” *Energy Environ. Sci.*, vol. 11, no. 8, pp. 1945–1976, 2018, doi: 10.1039/c8ee01053f.

[8] L. Liu *et al.*, “In Situ Formation of a Stable Interface in Solid-State Batteries,” *ACS Energy Lett.*, vol. 4, no. 7, pp. 1650–1657, Jul. 2019, doi: 10.1021/acsenergylett.9b00857.

[9] A. Miura *et al.*, “Liquid-phase syntheses of sulfide electrolytes for all-solid-state

lithium battery," *Nat. Rev. Chem.*, vol. 3, no. 3, pp. 189–198, 2019, doi: 10.1038/s41570-019-0078-2.

[10] A. Manthiram, X. Yu, and S. Wang, "Lithium battery chemistries enabled by solid-state electrolytes," *Nat. Rev. Mater.*, vol. 2, no. 4, p. 16103, 2017, doi: 10.1038/natrevmats.2016.103.

[11] F. Mizuno, A. Hayashi, K. Tadanaga, and M. Tatsumisago, "New, highly ion-conductive crystals precipitated from Li_2S–P_2S_5 glasses," *Adv. Mater.*, vol. 17, no. 7, pp. 918–921, 2005.

[12] Y. Kato *et al.*, "High-power all-solid-state batteries using sulfide superionic conductors," *Nat. Energy*, vol. 1, no. 4, p. 16030, 2016, doi: 10.1038/nenergy.2016.30.

[13] K. H. Park *et al.*, "Design Strategies, Practical Considerations, and New Solution Processes of Sulfide Solid Electrolytes for All-Solid-State Batteries," *Adv. Energy Mater.*, vol. 8, no. 18, 2018, doi: 10.1002/aenm.201800035.

[14] D. H. Kim *et al.*, "Infiltration of Solution-Processable Solid Electrolytes into Conventional Li-Ion-Battery Electrodes for All-Solid-State Li-Ion Batteries," *Nano Lett.*, vol. 17, no. 5, pp. 3013–3020, May 2017, doi: 10.1021/acs.nanolett.7b00330.

[15] L. Yang *et al.*, "Flexible Composite Solid Electrolyte Facilitating Highly Stable 'Soft Contacting' Li–Electrolyte Interface for Solid State Lithium-Ion Batteries," *Adv. Energy Mater.*, vol. 7, no. 22, 2017, doi: 10.1002/aenm.201701437.

[16] Z. Jiang *et al.*, "Tape-Casting $Li_{0.34}La_{0.56}TiO_3$ Ceramic Electrolyte Films Permit High Energy Density of Lithium-Metal Batteries," *Adv. Mater.*, vol. 32, no. 6, 2020, doi: 10.1002/adma.201906221.

[17] E. J. Cheng, T. Kimura, M. Shoji, H. Ueda, H. Munakata, and K. Kanamura, "Ceramic-Based Flexible Sheet Electrolyte for Li Batteries," *ACS Appl. Mater.*

Interfaces, vol. 12, no. 9, pp. 10382–10388, Mar. 2020, doi: 10.1021/acsami.9b21251.

[18] F. Strauss *et al.*, "Impact of Cathode Material Particle Size on the Capacity of Bulk-Type All-Solid-State Batteries," *ACS Energy Lett.*, vol. 3, no. 4, pp. 992–996, Apr. 2018, doi: 10.1021/acsenergylett.8b00275.

[19] A. Bielefeld, D. A. Weber, and J. Janek, "Microstructural modeling of composite cathodes for all-solid-state batteries," *J. Phys. Chem. C*, vol. 123, no. 3, pp. 1626–1634, 2018.

[20] T. Shi *et al.*, "High Active Material Loading in All-Solid-State Battery Electrode via Particle Size Optimization," *Adv. Energy Mater.*, vol. 10, no. 1, 2020, doi: 10.1002/aenm.201902881.

[21] X. Chen, W. He, L.-X. Ding, S. Wang, and H. Wang, "Enhancing interfacial contact in all solid state batteries with a cathode-supported solid electrolyte membrane framework," *Energy Environ. Sci.*, vol. 12, no. 3, pp. 938–944, 2019, doi: 10.1039/c8ee02617c.

[22] Y. Li *et al.*, "Ultralow-Concentration Electrolyte for Na-Ion Batteries," *ACS Energy Lett.*, vol. 5, no. 4, pp. 1156–1158, Apr. 2020, doi: 10.1021/acsenergylett.0c00337.

[23] K. Nagao *et al.*, "A reversible oxygen redox reaction in bulk-type all-solid-state batteries," *Sci. Adv.*, vol. 6, no. 25, p. eaax7236, 2020.

[24] J. Y. Kim *et al.*, "Revisiting TiS_2 as a diffusion-dependent cathode with promising energy density for all-solid-state lithium secondary batteries," *Energy Storage Mater.*, vol. 41, pp. 289–296, 2021.

[25] D. H. S. Tan *et al.*, "Carbon-free high-loading silicon anodes enabled by sulfide solid electrolytes," *Science (80-.).*, vol. 373, no. 6562, pp. 1494–1499, 2021.

[26] J. Y. Kim *et al.*, "Diffusion-dependent graphite electrode for all-solid-state

batteries with extremely high energy density," *ACS Energy Lett.*, vol. 5, no. 9, pp. 2995–3004, 2020.

[27] J. Y. Kim *et al.*, "Graphite–Silicon Diffusion-Dependent Electrode with Short Effective Diffusion Length for High-Performance All-Solid-State Batteries," *Adv. Energy Mater.*, vol. 12, no. 3, p. 2103108, 2022.

[28] J. Hu, H. Li, and X. Huang, "Electrochemical behavior and microstructure variation of hard carbon nano-spherules as anode material for Li-ion batteries," *Solid State Ionics*, vol. 178, no. 3–4, pp. 265–271, 2007, doi: 10.1016/j.ssi.2006.12.014.

[29] J.-H. Lee, H.-Y. Lee, S.-M. Oh, S.-J. Lee, K.-Y. Lee, and S.-M. Lee, "Effect of carbon coating on electrochemical performance of hard carbons as anode materials for lithium-ion batteries," *J. Power Sources*, vol. 166, no. 1, pp. 250–254, 2007, doi: 10.1016/j.jpowsour.2006.12.078.

[30] H. Sun, X. He, J. Ren, J. Li, C. Jiang, and C. Wan, "Hard carbon/lithium composite anode materials for Li-ion batteries," *Electrochim. Acta*, vol. 52, no. 13, pp. 4312–4316, 2007, doi: 10.1016/j.electacta.2006.12.012.

[31] B. Guo, J. Shu, K. Tang, Y. Bai, Z. Wang, and L. Chen, "Nano-Sn/hard carbon composite anode material with high-initial coulombic efficiency," *J. Power Sources*, vol. 177, no. 1, pp. 205–210, 2008, doi: 10.1016/j.jpowsour.2007.11.003.

[32] H. Haruna, S. Itoh, T. Horiba, E. Seki, and K. Kohno, "Large-format lithium-ion batteries for electric power storage," *J. Power Sources*, vol. 196, no. 16, pp. 7002–7005, 2011, doi: 10.1016/j.jpowsour.2010.10.045.

[33] H. Fujimoto, K. Tokumitsu, A. Mabuchi, N. Chinnasamy, and T. Kasuh, "The anode performance of the hard carbon for the lithium ion battery derived from the oxygen-containing aromatic precursors," *J. Power Sources*, vol. 195, no. 21, pp. 7452–7456, 2010, doi: 10.1016/j.jpowsour.2010.05.041.

[34] J.-L. Liu, J. Wang, and Y.-Y. Xia, “A new rechargeable lithium-ion battery with a $xLi_2MnO_3\cdot(1-x)\ LiMn_{0.4}Ni_{0.4}Co_{0.2}O_2$ cathode and a hard carbon anode,” *Electrochim. Acta*, vol. 56, no. 21, pp. 7392–7396, 2011, doi: 10.1016/j.electacta.2011.05.080.

[35] M. Park, X. Zhang, M. Chung, G. B. Less, and A. M. Sastry, “A review of conduction phenomena in Li-ion batteries,” *J. Power Sources*, vol. 195, no. 24, pp. 7904–7929, 2010, doi: https://doi.org/10.1016/j.jpowsour.2010.06.060.

[36] F. Bonino *et al.*, “A disordered carbon as a novel anode material in lithium-ion cells,” *Adv. Mater.*, vol. 17, no. 6, pp. 743–746, 2005.

[37] Y. Liu, J. S. Xue, T. Zheng, and J. R. Dahn, “Mechanism of lithium insertion in hard carbons prepared by pyrolysis of epoxy resins,” *Carbon N. Y.*, vol. 34, no. 2, pp. 193–200, 1996, doi: 10.1016/0008-6223(96)00177-7.

[38] R. De Levie, “On porous electrodes in electrolyte solutions—IV,” *Electrochim. Acta*, vol. 9, no. 9, pp. 1231–1245, 1964.

[39] N. Ogihara, Y. Itou, T. Sasaki, and Y. Takeuchi, “Impedance spectroscopy characterization of porous electrodes under different electrode thickness using a symmetric cell for high-performance lithium-ion batteries,” *J. Phys. Chem. C*, vol. 119, no. 9, pp. 4612–4619, 2015.

[40] N. Kaiser, S. Spannenberger, M. Schmitt, M. Cronau, Y. Kato, and B. Roling, “Ion transport limitations in all-solid-state lithium battery electrodes containing a sulfide-based electrolyte,” *J. Power Sources*, vol. 396, pp. 175–181, 2018.

5.6 Supporting Information

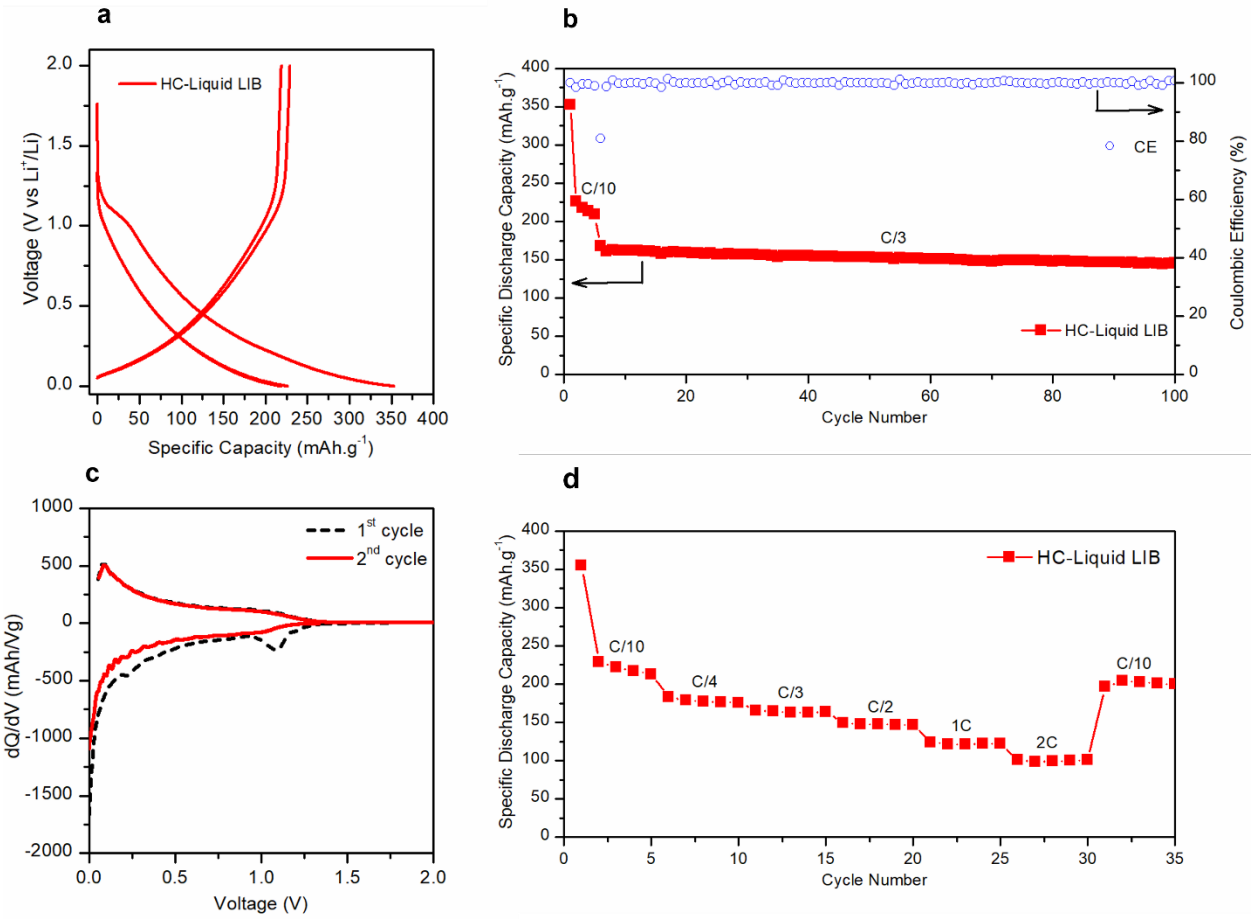

Figure 5.S1: (a) GCD profiles of HC at 0.1C in liquid LIB. (b) Cycling performance of HC electrode in liquid LIB. (c) Differential capacity vs. voltage for first and second cycles for HC. (d) Rate performance of HC electrode in liquid LIB.

In liquid LIBs, an HC material was previously reported to have a capacity of 322 mAh.g^{-1} and an initial CE of 83% [1]. The initial cycles half-cell performance of the developed HC sample in this work is shown in **Figure 5.S1a**. When combined with a lithium metal anode, HC is subjected to lithium insertion and removal at the typical low voltage value. Therefore, in the potential range of 0 - 2.0 V vs. Li$^+$/Li, a reversible capacity of 352.7 mAh.g^{-1} can be achieved with an efficiency of 98.6%, outperforming the earlier findings [2]–[4]. Li$^+$ intercalation starts at 1.2 V, and the curve slopes downward without exhibiting

a distinct plateau. This characteristic property may be explained by the chaotic crystal structure of HC [5]–[9]. Additionally, due to the creation of the SEI protective layer on the electrode surface and the trapping of some lithium in the electrode structure, the negative electrodes of rechargeable LIBs exhibit a typical electrochemical characteristic known as high irreversible capacity [10]–[14].

Furthermore, high irreversible capacities, slope profiles, and high-rate capability are typically seen in HC materials because of their disordered structure, which is made up of cross-linked carbon sheets (graphene layers). According to reports, sloping voltage profiles facilitate quick Li^+ insertion and disinsertion [7], [8] as well as convenient cell state-of-charge monitoring [9]. **Figure 5.S1b** shows the cycle life results of the cell at two different C-rates (C/10, C/3). This cell displayed a stable behavior over a long cycle time. After 100 cycles the specific capacity retains 89.2% of the initial value at the C/3 rate. It is also seen that the CE is very stable from the initial cycles and maintains a level close to 100% in the following cycles. The incremental capacity vs. potential (dQ/dV) is shown in **Figure 5.S1c** to closely examine the charge and discharge behavior. The differential capacity curve during the first cycle has two prominent peaks close to 1.2 and 0.25 V, as seen in the graph. The peak around 1.2 V has been linked to the breakdown of the electrolyte, which results in the formation of a passivating layer [15], [16], while the peak near 0.25 V results from the reactivity of lithium with surface functional groups or absorbed species as a result of exposure to the air [17]. Also, **Figure 5.S1d** illustrates the rate performance of the HC electrode at various rates in lithium half-cells, ranging from C/10 to 2C.

5.7 References

[1] X. Liao, J. Yu, and L. Gao, “Electrochemical study on lithium iron phosphate/hard carbon lithium-ion batteries,” *J. Solid State Electrochem.*, vol. 16, no. 2, pp. 423–428, 2012.

[2] H. Sun, X. He, J. Ren, J. Li, C. Jiang, and C. Wan, “Hard carbon/lithium composite anode materials for Li-ion batteries,” *Electrochim. Acta*, vol. 52, no. 13, pp. 4312–4316, 2007, doi: 10.1016/j.electacta.2006.12.012.

[3] B. Guo, J. Shu, K. Tang, Y. Bai, Z. Wang, and L. Chen, “Nano-Sn/hard carbon composite anode material with high-initial coulombic efficiency,” *J. Power Sources*, vol. 177, no. 1, pp. 205–210, 2008, doi: 10.1016/j.jpowsour.2007.11.003.

[4] J.-L. Liu, J. Wang, and Y.-Y. Xia, “A new rechargeable lithium-ion battery with a $xLi_2MnO_3\cdot(1-x)\ LiMn_{0.4}Ni_{0.4}Co_{0.2}O_2$ cathode and a hard carbon anode,” *Electrochim. Acta*, vol. 56, no. 21, pp. 7392–7396, 2011, doi: 10.1016/j.electacta.2011.05.080.

[5] M. Winter, J. O. Besenhard, M. E. Spahr, and P. Novak, “Insertion electrode materials for rechargeable lithium batteries,” *Adv. Mater.*, vol. 10, no. 10, pp. 725–763, 1998.

[6] E. Buiel and J. R. Dahn, “Li-insertion in hard carbon anode materials for Li-ion batteries,” *Electrochim. Acta*, vol. 45, no. 1–2, pp. 121–130, 1999.

[7] S. Atlung, B. Zachau-Christiansen, K. West, and T. Jacobsen, “The composite insertion electrode: theoretical part. Equilibrium in the insertion compound and linear potential dependence,” *J. Electrochem. Soc.*, vol. 131, no. 5, p. 1200, 1984.

[8] H. Shi, “Coke vs. graphite as anodes for lithium-ion batteries,” *J. Power Sources*, vol. 75, no. 1, pp. 64–72, 1998.

[9] P. Novák, D. Goers, and M. E. Spahr, “Carbon materials in lithium-ion batteries,”

Carbons Electrochem. Energy Storage Syst., pp. 263–328, 2010.

[10] F. Bonino *et al.*, “A disordered carbon as a novel anode material in lithium-ion cells,” *Adv. Mater.*, vol. 17, no. 6, pp. 743–746, 2005.

[11] K. Gotoh *et al.*, “Properties of a novel hard-carbon optimized to large size Li ion secondary battery studied by 7Li NMR,” *J. Power Sources*, vol. 162, no. 2, pp. 1322–1328, 2006.

[12] Q. Wang, H. Li, L. Chen, and X. Huang, “Monodispersed hard carbon spherules with uniform nanopores,” *Carbon N. Y.*, vol. 39, no. 14, pp. 2211–2214, 2001.

[13] J. R. Dahn, T. Zheng, Y. Liu, and J. S. Xue, “Mechanisms for lithium insertion in carbonaceous materials,” *Science (80-.).*, vol. 270, no. 5236, pp. 590–593, 1995.

[14] D. A. Stevens and J. R. Dahn, “High capacity anode materials for rechargeable sodium-ion batteries,” *J. Electrochem. Soc.*, vol. 147, no. 4, p. 1271, 2000.

[15] R. Fong, U. Von Sacken, and J. R. Dahn, “Studies of lithium intercalation into carbons using nonaqueous electrochemical cells,” *J. Electrochem. Soc.*, vol. 137, no. 7, p. 2009, 1990.

[16] Y. Matsumura, S. Wang, and J. Mondori, “Mechanism leading to irreversible capacity loss in Li ion rechargeable batteries,” *J. Electrochem. Soc.*, vol. 142, no. 9, p. 2914, 1995.

[17] W. Xing and J. R. Dahn, “Study of irreversible capacities for Li insertion in hard and graphitic carbons,” *J. Electrochem. Soc.*, vol. 144, no. 4, p. 1195, 1997.

6 Chapter 6: Conclusions and Future Work

6.1 Conclusions

In this thesis, two studies focused on the diffusion-dependent solid-state electrode structure were carried out to investigate various aspects of this design approach, including using of various materials to obtain high-performance all-solid-state lithium-ion batteries (ASSLIBs) by using the diffusion-dependent electrode.

The first study used graphite-phosphorus (Gr/P) diffusion-dependent electrodes for sulfide-based ASSLIBs. A straightforward electrode design primarily comprising composite active materials of graphite and phosphorus is proposed to simultaneously satisfy the high power and high energy density requirements of ASSBs. First, several active material ratios (graphite: phosphorus) were examined to determine the ideal ratio that offers the highest performance in terms of capacity and stability. For graphite to phosphorus ratios of 70%, 80%, 85%, 90%, and 95%, the cell had an initial specific discharge capacity of 372 $mAh.g^{-1}$, 505.1 $mAh.g^{-1}$, 683.6 $mAh.g^{-1}$, 638.2 $mAh.g^{-1}$, and 444.5 $mAh.g^{-1}$ at 0.1 C-rate, respectively. The cell displayed capacity retention values of 26.0%, 44.5%, 74.8%, 96.3%, and 97.1% at 0.1 C-rate and after 10 cycles for graphite: phosphorus ratios of 70%, 80%, 85%, 90%, and 95%, respectively. These results indicate that the Gr/P diffusion-dependent electrode with a graphite: phosphorus ratio of 90:10 percent exhibits the highest performance in terms of specific capacity and cycling stability. Thus, the Gr/P diffusion-dependent electrode with this ratio of active materials is utilized to compare its performance to that of a graphite diffusion-dependent electrode. At high temperature (60 °C) and 0.1 C-rate, the graphite diffusion-dependent electrode exhibited a specific capacity of 257.8 $mAh.g^{-1}$. In contrast, the Gr/P diffusion-dependent electrode had a specific capacity of 638.2 $mAh.g^{-1}$, which is higher than the theoretical specific capacity that can be attained using only graphite. Additionally, after 40 cycles, graphite and Gr/P diffusion-dependent electrodes showed 92.4% and 92.7% capacity retention, respectively. The tests were also carried out at room temperature to demonstrate the unique capability of the proposed electrode. At room temperature and 0.1

C-rate, the initial specific capacity of the graphite diffusion-dependent electrode was 152.2 $mAh.g^{-1}$. However, the initial specific capacity of the Gr/P diffusion-dependent electrode was 246.4 $mAh.g^{-1}$, 66.2% of the theoretical capacity of the graphite. Additionally, the cell demonstrated capacity retention of 87.5% and 94.8% for graphite and Gr/P diffusion-dependent electrodes, respectively, after 9 cycles. These results show that the suggested electrode can operate with high cycling performances even at low temperatures, thus providing new avenues for developing ASSBs.

The second study utilized hard carbon (HC) diffusion-dependent electrodes for sulfide-based ASSLIBs. Since HC has never been investigated in ASSLIBs, we first employed this electrode material in liquid LIB to compare and validate the results obtained for solid-state cells. In liquid LIB, high initial specific discharge capacity (352.7 $mAh.g^{-1}$) and initial CE (98.6%) values were displayed by this electrode material at room temperature and 0.1C rate. Additionally, this material exhibited a capacity retention of 89.2% after 100 cycles at a C/3 rate. Then, the HC diffusion-dependent solid-state electrode was used in ASSBs to produce high-performance ASSLIBs. Contrasting the composite electrode, the novel electrode design that is being proposed is made entirely of densely compacted HC materials without any solid electrolyte. For the transport of lithium ions in the HC electrode, diffusion between HC particles with a seamless interface has been used extensively. Interparticle diffusion is allowed in the developed electrode, and performance improvement is possible, according to the experiments presented. Different testing conditions, such as room temperature (RT), high temperature (HT), and both high temperature and high pressure (HP), were used to examine the cycling performance and stability of the diffusion-dependent electrode. For RT, HT, and both HT and HP conditions, the cell showed initial specific discharge capacity values of 295.6 $mAh.g^{-1}$, 437.9 $mAh.g^{-1}$, and 514.4 $mAh.g^{-1}$, respectively. Furthermore, the initial CE values for the RT, HT, and HT and HP situations were 31.6%, 28.2%, and 38.4%, respectively. Moreover, the cell displayed capacity retention values of 86.6%, 57.4%, and 76.7% at RT, HT, and both HT and HP, respectively, after 100 cycles at 0.1 C-rate. As a result, the proposed diffusion-dependent electrode demonstrated superior cycling and rate performances at HT and HP compared to the other two conditions. These outcomes are

reasonable and comparable with the information provided for liquid LIBs. Thus, these results offer a practical strategy for developing an all-solid-state electrode with great performance utilizing a straightforward method.

It should be highlighted that testing for the thesis was carried out under controlled laboratory circumstances using mold/coin half-cells rather than the full cells in actual batteries. Therefore, the results might not be immediately applicable to battery packs for real-world applications. It could be possible to obtain more realistic data by repeating the testing with full cells (such as pouch cells) and the appropriate cathode materials (such as lithium cobalt oxide).

In conclusion, this thesis proposes a diffusion-dependent electrode, an innovative concept of the solid-state electrode. In the first study, Gr/P diffusion-dependent electrode was introduced for the first time. By virtue of in-situ forming Li_3P ionic conductors, Gr/P diffusion-dependent electrode exhibits better cycling performance and rate performance compared to the graphite diffusion-dependent electrode. Even at room temperature, the resultant Gr/P diffusion-dependent electrode presented superior cycling performance. In the second study, another important anode material—hard carbon—is systematically investigated as the diffusion-dependent electrode for the first time, which also shows decent electrochemical performance at both room temperature and elevated temperature. These research outcomes would guide the future design of diffusion-dependent electrodes for high-performance all-solid-state batteries.

6.2 Recommendations for Future Work

Despite the increased focus on the diffusion-dependent electrodes to achieve high energy density in ASSBs having made them a popular topic to study, with many researchers already contributing to this area of research, there are still many research directions to pursue to optimize the diffusion-dependent electrode structure, from developing high performance at room temperature to adjusting the electrode structure to improve Li-ion diffusivity. We believe there are still several materials available that can be designed and utilized for diffusion-dependent electrodes. Due to the constrained ion transport kinetics,

many studies have described the electrochemical performance of the diffusion-dependent electrodes at high temperatures (60 °C – 100 °C). Thus, it is encouraged to keep looking for and developing new electrode materials with high Li-ion diffusivity and excellent electronic conductivity, which could allow the room-temperature operation of diffusion-dependent electrodes.

Future research in this area could be directed in several directions, one of which would be the creation of diffusion-dependent electrodes that exhibit high performance at room temperature. To achieve this, it is necessary to look for advanced anode materials with high Li-ion diffusivity and electronic conductivity at room temperature. In this regard, alloy anodes are a potential substitute for the diffusion-dependent electrode's future. Numerous alloy anodes benefit from being inherently electronic conductive, and several highly lithiated metals have comparatively high lithium diffusivities [1], [2]. For instance, the Mg alloy's most lithiated phase, Li_3Mg [3], has a lithium diffusion coefficient of 10^{-7} $cm^2.s^{-1}$ [4]. Also, $Li_{13}In_3$ [5], the most lithiated phase of the In alloy, has a lithium diffusion coefficient of 10^{-8} $cm^2.s^{-1}$ [6]. Moreover, Li_3Sb [7] is the Sb alloy's most lithiated phase, with a lithium diffusion coefficient of 10^{-8} - 10^{-9} $cm^2.s^{-1}$ [2]. Due to the increased Li-ion diffusivity, these alloy anodes can be employed as the diffusion-dependent electrode to achieve high-performance ASSBs at room temperature.

Further work can be done on improving the areal capacity, which might be achieved by tuning the electrode structure. Creating a seamless interface between the active material particles is necessary to achieve perfect Li-ion interdiffusion. This is made possible by controlling the size of the active material particles. Particle size optimization can be utilized to achieve a minimum void space in an electrode morphology which might allow for sufficient Li-ion diffusion between the active material particles [8]. The Li-ion diffusivity between active material particles can also be improved by using nanoscale particles. The advantage of nanosizing materials for bulk transport is typically attributed to nanoparticles' increased surface to volume ratio and shorter transport distance [9].

6.3 References

[1] T. R. Jow and C. C. Liang, “Lithium-Aluminum Electrodes at Ambient Temperatures,” *J. Electrochem. Soc.*, vol. 129, no. 7, pp. 1429–1434, 1982, doi: 10.1149/1.2124178.

[2] E. Allcorn, S. O. Kim, and A. Manthiram, “Lithium diffusivity in antimony-based intermetallic and FeSb–TiC composite anodes as measured by GITT,” *Phys. Chem. Chem. Phys.*, vol. 17, no. 43, pp. 28837–28843, 2015.

[3] W.-J. Zhang, “A review of the electrochemical performance of alloy anodes for lithium-ion batteries,” *J. Power Sources*, vol. 196, no. 1, pp. 13–24, 2011, doi: https://doi.org/10.1016/j.jpowsour.2010.07.020.

[4] Z. Shi, M. Liu, D. Naik, and J. L. Gole, “Electrochemical properties of Li–Mg alloy electrodes for lithium batteries,” *J. Power Sources*, vol. 92, no. 1, pp. 70–80, 2001, doi: https://doi.org/10.1016/S0378-7753(00)00521-8.

[5] S. Y. Han *et al.*, “Porous Metals from Chemical Dealloying for Solid-State Battery Anodes,” *Chem. Mater.*, vol. 32, no. 6, pp. 2461–2469, Mar. 2020, doi: 10.1021/acs.chemmater.9b04992.

[6] M. Hiratani, K. Miyauchi, Y. Ito, K. Kanehori, F. Kirino, and T. Kudo, “Solid state lithium battery.” Google Patents, Feb. 24, 1987.

[7] B. T. Heligman and A. Manthiram, “Elemental Foil Anodes for Lithium-Ion Batteries,” *ACS Energy Lett.*, vol. 6, no. 8, pp. 2666–2672, Aug. 2021, doi: 10.1021/acsenergylett.1c01145.

[8] T. Shi *et al.*, “High Active Material Loading in All-Solid-State Battery Electrode via Particle Size Optimization,” *Adv. Energy Mater.*, vol. 10, no. 1, 2020, doi: 10.1002/aenm.201902881.

[9] C. Delacourt, P. Poizot, S. Levasseur, and C. Masquelier, “Size effects on carbon-

free $LiFePO_4$ powders: The key to superior energy density," *Electrochem. Solid-State Lett.*, vol. 9, no. 7, p. A352, 2006.

Curriculum Vitae

Name:	Peiman Mardani
Post-secondary Education and Degrees:	University of Tehran (UT) Tehran, Tehran, Iran 2015 – 2019 B.A.
	The University of Western Ontario London, Ontario, Canada 2021 – 2022 Master
Honours and Awards:	Western Engineering Full Scholarship 2021 - 2022
	Full Scholarship for bachelor's Studies at University of Tehran 2015 - 2019
Related Work Experience	Teaching Assistant The University of Western Ontario 2021 - 2022
	Research Assistant The University of Western Ontario 2021 - 2022